University of Brasília

Institute of Physics

Thesis

Properties of Charged Quasiparticles in Highly Confined Materials

Propriedades de Quasipartículas Carregadas em Materiais Altamente Confinados

Tiago de Sousa Araújo Cassiano

Tiago de Sousa Araújo Cassiano

Properties of Charged Quasiparticles in Highly Confined Materials

Propriedades de Quasipartículas Carregadas em Materiais Altamente Confinados

Thesis Dissertation presented to the Institute of Physics of the University of Brasília as a partial requirement to obtain the degree of doctor of physics.

Advisor: Prof. Pedro Henrique de Oliveira Neto

Brasilia, August of 2024.

"You ask me if an ordinary person, by studying hard, would get to be able to imagine these things, like I imagine. Of course! I was an ordinary person who had studied hard. There are no miracle people."

Richard P. Feynman

Acknowledgments

I would like to thank my mother, Lucenira de Sousa Araújo, and my aunt, Maria das Graças Aureliano, for supporting me since the beginning. Only because of your support, I could pursue such a difficult career path with no hesitation. I am forever grateful for all the sacrifices.

I thank Larissa dos Santos Born for the unwavering support and understanding. Your daily care and wonderful smile have helped me face challenges with enthusiasm.

I am also eternally grateful for my teachers, who through a genuine and intense effort guided me through this journey. I thank Prof. Geraldo Magela e Silva for all the excellent lectures. They became the core of my scientific foundation. I also greatly appreciate the enjoyable collaborations and the funny talks, from which I always learn something interesting. I thank my advisor, Prof. Pedro Henrique de Oliveira Neto, for his enormous effort in guiding me through the steep steps of academic formation while expecting nothing less than excellence, always willing to offer (excellent) counsel. I thank Prof. Ricardo Gargano for his optimism and kindness during our collaborations and Prof. Luiz Antônio Ribeiro Junior for his dedication and insightful contributions. All the teachers that I could not mention: thank you for your guidance.

I thank all members of LSSC, active and "off-duty", for the companionship shared through theses years. Unfortunately, the limited space does not allow me to mention everyone. I thank in special Dr. Leonardo Evaristo de Sousa for his help through these years, showing inspiring tolerance and determination even when nothing works. Finally, I thank Fernando Teixeira Bueno for his friendship and all his help.

CONTENTS

Abstract

The use of confined materials is profoundly shaping our civilization. Today, confinement remains an important design choice in many modern materials, such as graphene, fullerene, and graphene nanoribbons. For most optoelectronic devices, charge transport is a pivotal step. In organic materials, it is convenient to interpret the mechanism as the drifting of quasiparticles, resulting from the coupling of a localized charge with phonon clouds. Understanding their properties can elucidate the response of complex confined systems and provide the theoretical foundation for proposing new materials. In this work, eight studies on the properties of charge quasiparticles in confined materials are presented. Each study addresses specific facets of quasiparticle physics, such as mechanical and electronic stability, transport efficiency, structural design, and temperature effects. Four main systems with different confinement regimes are considered: conjugated polymers (1D), graphene nanoribbons (2D), bilayer graphene nanoribbons (quasi-2D), and molecular crystals (2D). The physical description of the molecules is achieved using model Hamiltonians that account for lattice relaxation effects. The dynamics of charged quasiparticles were determined by simulating their interaction with a time-dependent external electric field. The findings contribute to the theoretical understanding of highly confined systems and may inspire future applied research in materials science.

keywords: SSH model, Graphene, GNR, polaron, mobility, heterojunctions

Resumo

O uso de materiais confinados está moldando profundamente nossa civilização. Atualmente, o confinamento continua sendo uma escolha importante no design de muitos materiais modernos, como grafeno, fulereno e nanofitas de grafeno. Para a maioria dos dispositivos optoeletrônicos, o transporte de carga é uma etapa crucial. Em materiais orgânicos, é conveniente interpretar o mecanismo como o deslocamento de quasipartículas, resultante do acoplamento de uma carga localizada com nuvens de fônons. Compreender suas propriedades pode elucidar a resposta de sistemas confinados complexos e fornecer a base teórica para a proposição de novos materiais. Neste trabalho, são apresentados oito estudos sobre as propriedades de quasipartículas de carga em materiais confinados. Cada estudo aborda aspectos específicos da física das quasipartículas, como estabilidade mecânica e eletrônica, eficiência de transporte, design estrutural e efeitos da térmicos. Quatro sistemas principais, com diferentes regimes de confinamento, são considerados: polímeros conjugados (1D), nanofitas de grafeno (2D), nanofitas de grafeno bicamada (quasi-2D) e cristais moleculares (2D). A descrição física das moléculas é alcançada usando Hamiltonianos modelos que levam em conta os efeitos de relaxamento da rede. A dinâmica das quasipartículas carregadas foi determinada simulando sua interação com um campo elétrico externo dependente do tempo. Os resultados obtidos contribuem para a compreensão teórica de sistemas altamente confinados e podem inspirar futuras pesquisas aplicadas na ciência dos materiais.

Resumo Expandido

Polímeros condutores conjugados, desde o poliacetileno sintetizado acidentalmente nos anos 70, são cruciais na tecnologia moderna, como OPVs, OLEDs e transistores. Além de sua importância tecnológica, a síntese desses polímeros inspirou a descoberta de materiais como fulerenos, nanotubos de carbono e grafeno. Este último, conhecido por suas propriedades eletrônicas excepcionais, continua sendo uma fonte de inovação em diversas áreas, apesar de sua falta de *band gap* para aplicações semicondutoras. Técnicas como dopagem e cortes em nanofitas de grafeno (GNRs) são exploradas para superar essa limitação, oferecendo potencial para aplicações optoeletrônicas avançadas.

Historicamente, dois tipos de bordas são centrais no desenvolvimento das aplicações baseadas GNRs: as nanofitas armchair (AGNR) e zigzag (ZGNR). AGNRs têm bordas em forma de “cadeira de braço", enquanto ZGNRs possuem bordas com ligações alternadas cis-trans. Outras simetrias, como nanofitas quirais (chGNRs) e cove-type (CGNRs) vem ganhando importânica, ampliando as possibilidades de aplicação. As CGNRs, sintetizadas inicialmente em 2014, destacam-se por sua estrutura quase sem defeitos, um gap de 1,88 eV, e alta mobilidade de carga, tornando-as promissoras para a próxima geração de dispositivos optoeletrônicos baseados em GNRs. As bordas das GNRs influenciam diretamente suas propriedades, deter-

minando sua aplicabilidade em diferentes campos. Por exemplo, ZGNRs são adequadas para spintrônica, enquanto AGNRs e CGNRs, com gap adequado, são ideais para dispositivos semicondutores como OPVs e OFETs. O estudo teórico da eficiência de transporte em GNRs pode guiar futuros experimentos e avanços conceituais. Recentemente, uma nova estratégia de design foi introduzida para nanofitas de grafeno (GNRs), aumentando ainda mais o potencial dessas estruturas. A ideia principal é combinar duas nanofitas diferentes para formar uma nova geometria chamada heterojunção. Esse sistema híbrido exibe propriedades únicas devido à mistura dos materiais base, permitindo controle sobre propriedades topológicas, engenharia de gap, e outros comportamentos inovadores. Essa flexibilidade torna as heterojunções altamente adaptáveis para atender às exigências industriais, elevando o potencial das GNRs em futuras aplicações optoeletrônicas semicondutoras. Essa abordagem pode evitar a necessidade de desenvolver novos materiais do zero, economizando tempo. No entanto, devido à variedade de bordas e conformações possíveis, grande parte do potencial das heterojunções permanece inexplorado, exigindo investigações teóricas para explorar suas implicações. Combinar materiais 2D em sistemas de bicamadas, como no caso do grafeno, também pode gerar propriedades emergentes, como supercondutividade. Empilhar GNRs é uma rota promissora para explorar essas propriedades em aplicações semicondutoras. Outro material de interesse são os cristais moleculares orgânicos (OMC), que possuem propriedades dependentes das unidades moleculares e da organização cristalina. O transporte de carga nesses materiais é crucial para dispositivos optoeletrônicos, como células fotovoltaicas e eletrônicos flexíveis. O fenômeno do transporte de carga em compostos orgânicos difere dos cristais inorgânicos, com distorções da rede causadas pela ionização da carga. Essas distorções, favoráveis energeticamente, resultam em estados ligados conhecidos como quasipartículas, simplificando o tratamento das interações complexas nos materiais orgânicos estendidos, como polímeros conjugados, GNRs e cristais moleculares.

Quasipartículas são caracterizadas por carga, spin, perfil de distorção da rede e estados intragap. Cargas efetivas e mobilidade variam conforme o material, impactando significativamente o potencial de sistemas para aplicações semicondutoras. Polarons, quasipartículas carregadas com spin meio e carga $\pm e$, têm menor massa efetiva e maior mobilidade, sendo cruciais no transporte de carga. Bipolarons, formados pelo estado ligado de dois polarons, possuem maior massa efetiva e são relevantes em mecanismos de emissão, podendo formar biexcitons. A mobilidade e massa efetiva dessas quasipartículas variam entre materiais, sendo definidoras na eficiência de dispositivos optoeletrônicos.

AGNRs apresentam uma massa efetiva de portadores de carga que depende da largura das nanofitas, com estimativas de massa efetiva variando entre 0-60 m_e e mobilidade de até $350\,\mathrm{cm}^2/\mathrm{Vs}$. Em cristais moleculares, a mobilidade é inferior devido à menor coesão intermolecular, mas esses materiais são mais robustos a defeitos de síntese, facilitando o design de dispositivos. No entanto, combinar alta mobilidade com um bandgap não nulo é um desafio. A redução da largura das GNRs aumenta o gap, mas reduz a mobilidade e aumenta a massa efetiva, um problema também observado no design de cristais moleculares. Encontrar materiais com gap finito e portadores de carga eficientes é uma necessidade constante para avanços tecnológicos e teóricos.

A tese consiste em uma compilação de oito trabalhos que visam investigar as propriedades dos portadores de carga em materiais altamente confinados. Cada trabalho foca em um aspecto específico do portador, como efeitos de temperatura, interação com o campo elétrico e mudanças geométricas. O texto é dividido com base no tipo de sistema em questão: polímeros conjugados, nanofitas de grafeno, nanofitas bicamada e cristais moleculares.

O primeiro trabalho, intitulado *Quasiparticle Dynamics by Effective π-Field Distortion*[1], consiste em uma reinterpretação do formalismo SSH, onde o campo de forças eletrônico é identificado como originado de uma força uniforme, semelhante à gravidade. Um aprofundamento dessa análise sugere que a presença de quasipartículas pode ser vista como uma deformação local nesse campo de forças, apresentando um comportamento análogo ao de massa na teoria da relatividade geral.

O segundo trabalho, intitulado *Charge transport in cove-type graphene nanoribbons: The role of quasiparticles*[2], estuda as propriedades de transporte dos portadores polaron e bipolaron em nanofitas do tipo cove. Sob a influência de um campo elétrico externo, as mobilidades e massas efetivas são calculadas. Os resultados mostram que esse tipo de nanofita possui grande potencial para aplicações em transistores, devido ao transporte eficiente das quasipartículas.

No terceiro trabalho, intitulado *Regulating Polaron Transport Regime via Heterojunction Engineering in Cove-Type Graphene Nanoribbons*[3], propomos uma combinação de heterojunção que integra diferentes nanofitas do tipo cove. Estudos de estabilidade e transporte são realizados utilizando materiais na solução do tipo polaron. Os resultados mostram que, dependendo da composição, o transporte pode atingir um regime de semi-hopping atômico, onde o polaron salta entre blocos específicos da molécula. Análises de mobilidade indicam que essa engenharia geométrica possibilita a modulação da eficiência de transporte.

Baseada na mudança geométrica do terceiro trabalho, propomos uma reformulação do tratamento de nanofitas no modelo SSH 2D. Intitulado *Quasiparticles in Graphene Nanoribbon Heterojunctions: Insights from a Simplified One-Dimensional Model*[4], o trabalho apresenta uma estratégia para mapear o modelo 2D de transporte em um polímero 1D fictício que exibe as mesmas características de transporte.

O quinto trabalho, *Thermal-Induced Charge Carrier Population Control on Graphene Nanoribbons*[5], explora as implicações da estabilidade de polarons estacionários sob a influência de perturbações térmicas. O efeito é modelado como flutuações nas ligações covalentes. Os resultados mostram que altas temperaturas degradam o perfil de portadores localizados. Além disso, é demonstrado que, para certos regimes de temperatura, a energia de ligação de bipolarons é positiva, indicando que a formação de polarons pode ser energeticamente mais favorável.

O sexto trabalho, *Phase Transition of Polarons in Bilayer Graphene Nanoribbons*[6], é o primeiro estudo sobre nanofitas de grafeno bicamada nesta tese. Investigamos os efeitos da proximidade entre camadas na formação de portadores de carga em nanofitas bicamada ultrafinas. Os resultados indicam a presença de pelo menos duas soluções possíveis: a não-simétrica e a simétrica. A primeira solução corresponde ao caso em que a maior parte da carga está localizada em uma única nanofita. Por outro lado, o polaron simétrico possui metade de sua carga em cada camada.

Como uma extensão natural, investigamos as propriedades de bipolarons em sistemas bicamada, resultando no sétimo trabalho, *Strain-Tuneable Bipolaron Stability on Ultranarrow Bilayer Graphene Nanoribbons*[7]. Os resultados mostram que o controle preciso da proximidade entre as nanofitas (que pode ser modelado por pressão externa ou inclusão de outros materiais no meio) permite modular a estabilidade dos bipolarons. Esta conclusão tem implicações importantes na área tecnológica, visto que os bipolarons participam de processos recombinatórios na difusão de biéxcitons.

Por fim, o último trabalho intitula-se *Large Polarons in Two-Dimensional Fullerene Networks: The Crucial Role of Anisotropy in Charge Transport*[8]. O estudo consiste em uma descrição teórica do transporte de carga em um cristal molecular composto por redes de fulerenos. Tanto a velocidade quanto a estabilidade do portador são avaliadas, mostrando um desempenho comparável ao de cristais de ponta. Os resultados também oferecem uma visão detalhada do mecanismo de transporte por meio de dinâmicas não adiabáticas.

CHAPTER 1

INTRODUCTION

1.1 Conjugated Polymers

From the trash bag to high-end optoelectronic devices, conjugated polymers are deeply present in our civilization. The diverse and massive use of conducting polymers traces back to the groundbreaking synthesis of polyacetylene, reported in the '70s by Prof. Hideki Shirakawa's group[9, 10]. The synthesis route — discovered by accident during the experiment of Hideki's former student — motivated the search for other polymers. Since then, the use of conjugated polymers has only increased. Nowadays, polymer science is an established field, behind the development of modern organic photovoltaic cells (OPV)[11], organic light-emitting diodes (OLED)[12, 13], transistors[14], and other crucial technological devices[15].

Its importance goes even beyond direct technological integration. The synthesis of conjugated polymers also inspired the search for other conjugated organic allotropies. The investigation led to many other key materials such as fullerenes[16] and carbon nanotubes[17]. In this context, graphene[18] is one of the most notorious variations. This two-dimensional system can be thought of, in many aspects, as a series of infinite polyacetylene chains vertically bonded. Figure 1.1 illustrates this form of presentation, in which we transition from a one-dimensional system to a two-dimensional array. On the left side, multiple (identical) polymer chains are presented. Connecting them through covalent bonds returns the graphene geometry.

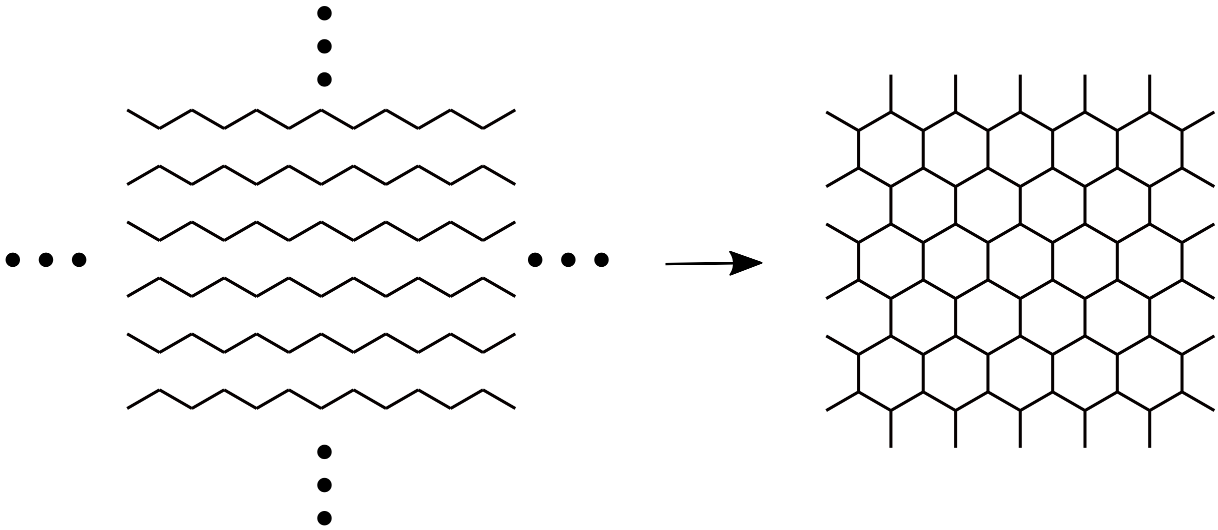

Figure 1.1: Representation of graphene as a combination of infinite polymers connected vertically.

1.2 Graphene

After almost 20 years from its first reported isolation[18], graphene remains a strong source of innovation and theoretical breakthroughs in materials science, being applied in diverse fields such as gas sensing[19, 20], electronics[21, 22, 23] and biomedical devices[24, 25, 26]. Most of the potentiality relies on its outstanding electronic properties. Graphene's mobility is estimated in almost $200\,000\,\mathrm{cm^2/Vs}$[27, 28] far outperforming almost every other organic compound. However, this attribute is a direct consequence of its linear electronic band, near the Fermi level at the Dirac points[29]. Because the gap is zero, the use of pristine graphene for semiconductor applications is undermined. In the face of this restriction, intense effort is dedicated to design techniques to grant semiconductor behavior to graphene. One possibility is to enforce doping[30, 31, 32], adding non-carbon atomic species to the lattice. This transformation breaks the lattice symmetry and consequently opens the gap. A more elegant alternative is to cut the sheet along some axis. The idea is to reduce the stripes' widths dramatically. They become so thin that quantum confinement starts to take place. A finite gap can rise depending on the shape cut and the width. These materials, known as graphene nanoribbons (GNRs)[33], are a potential source for high-end optoelectronics.

1.3 Graphene Nanoribbons

Besides the bandgap, GNRs also display other attributes that stand out when compared with state-of-art materials[34]. Similarly to graphene, this quasi-one-dimensional material has high surface area[35] with intense mechanical stress resilience[36], excellent thermal conductivity[37] and promising transport properties[38, 39]. Moreover, simple structural changes such as width and border variations have a tremendous effect on the overall molecule's response, allowing fine-tuning design towards specific applications through predictable and elegant procedures[40, 41, 42].

1.3.1 Edge Shapes

Historically, two edge shapes play a central role in the current development of GNR-based applications: the armchair (AGNR) and the zigzag (ZGNR) nanoribbons[33, 43]. Figure

1.2 displays these conformations, where (a) shows the former and (b) the latter. As the name suggests, the AGNRs' edges, highlighted in red, resemble an armchair, while the ZGNRs' borders, in blue, are composed of alternating cis-trans bonds. Other symmetries are allowed by composing AGNRs and ZGNRs, forming specimens such as the chiral graphene nanoribbons (chGNRs)[34, 44, 45] or the cove-type graphene nanoribbons (CGNRs)[38, 42, 2]. We illustrate in Figure 1.2(c) the 4CGNR, a member of the latter type. The nomenclature refers to the number of sites along the vertical axis. In this thesis, one of the main focuses is the study of nanoribbons with cove symmetry.

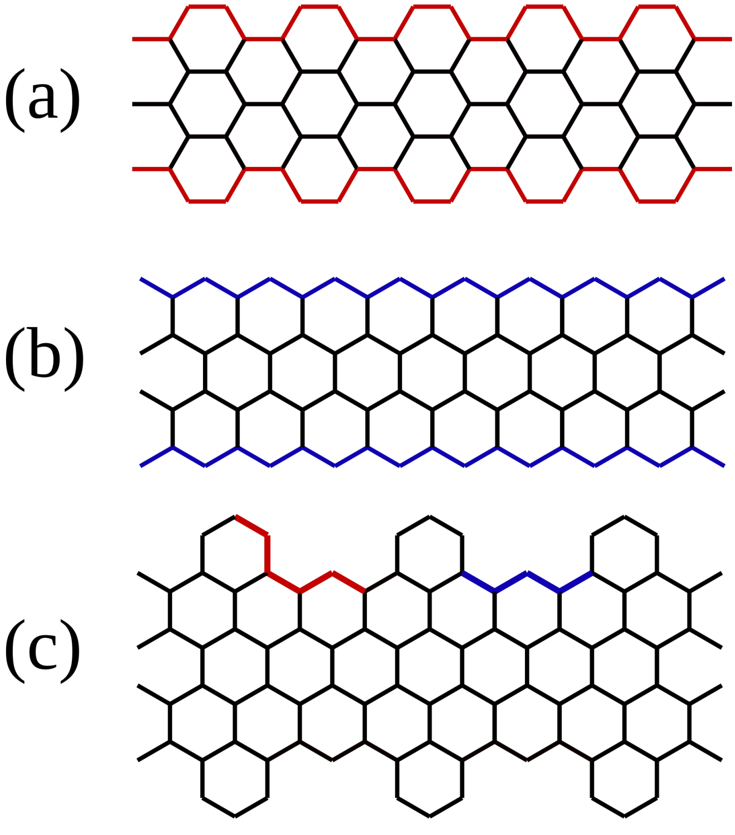

Figure 1.2: Diagrams of nanoribbons specimens of AGNR (a), ZGNR (b), and CGNRs (c) edge shapes. The colors highlight the border shapes of each molecule type: red for the AGNR and blue for the ZGNR. The cove-type has the contribution of both symmetries.

Synthesized in 2014 through a liquid-based bottom-up route[38], the 4-CGNRs are reported to have notable attributes, even when compared to other GNRs, as they exhibit a well-extended structure with almost no structural defects. Moreover, UV-VIS spectra reveal a gap of 1.88 eV, suitable for the nanoribbon to behave as a semiconductor. Finally, terahertz spectroscopy (THz) indicates that 4-CGNRs' charge transport may be highly efficient with mobility estimated between 150 and 15000 $\mathrm{cm}^2/\mathrm{Vs}$. All these properties give a promising future for these nanoribbons, having the potential to lead the next generation of GNRs' optoelectronics.

1.4 Applications

There is a wide range of applicability for GNRs. The edges have a definitive impact on the overall nanoribbons' properties, meaning that specimens with different edge symmetries may be fit for entirely distinct uses. In practice, this expands the applicability to numerous and diverse fields. For instance, ZGNRs are extensively used in spintronics[46, 47]. Members of certain width families in the AGNRs are present in high-end optoelectronics, inside OPVs[48, 49], OFETs[50, 51], and other devices[34, 52].

The main target of CGNRs and semiconducting AGNRs is within the same applications, considering that the material displays adequate bandgap for them. Synthesized in 2014 through a liquid-based bottom-up route[38], the cove GNR class is reported with notable attributes, even when compared to other GNRs, exhibiting a well-extended structure with almost no structural defects. Moreover, UV-VIS spectra reveal a gap of 1.88 eV, suitable for the nanoribbon to behave as a semiconductor. Finally, terahertz spectroscopy (THz) indicates that 4-CGNRs' charge transport may be highly efficient with mobility estimated between 150 and

$15\,000\,\mathrm{cm}^2/\mathrm{Vs}$. All these properties give a promising future for these nanoribbons, having the potential to lead the next generation of GNRs' optoelectronics.

In general, a theoretical investigation of the transport efficiency of those highly confined systems is of great interest, potentially assisting future experimental endeavors and further deepening the theoretical foundation through conceptual breakthroughs.

1.4.1 Heterojunctions

Recently, another design strategy became available to GNRs, pushing even further the potential of these structures. The main idea is to combine two different nanoribbons to form a new geometry called heterojunction[53, 54]. This hybrid system displays its own unique properties due to the mixing of the two base materials. Past studies indicate the prospect of this technique, reporting the control of topological properties[45], gap engineering[55], and the rising of unique behaviors.

A notable experimental breakthrough was achieved in 2018 through the synthesis of a heterojunction combining 9AGNR with 7AGNR borders[53]. The authors proposed that the electronic topological properties could be controlled by carefully merging these components. Since then, various studies have focused on exploring similar design strategies. Recently, the impact of combining chevron borders with 9AGNR blocks was assessed, demonstrating not only the capability to tune the bandgap but also to control current under uniaxial strain[56, 57]. Another possibility is to merge hexagonal nanoribbons made from different atomic species. Recently, computational simulations revealed that combining zigzag GNRs with boron nitride lattices allows the formation of magnetic flux chains, with tunable momentum splitting and spin depending on the influence of external fields[58].

All these attributes make the heterojunctions' physical properties even more flexible to be tuned[59], allowing them to fulfill highly detailed specifications of industrial demands while holding all the general properties of GNRs, elevating even further the potential of GNRs in future semiconducting optoelectronics[60]. This new pathway may eliminate the need to search for entirely new materials, which can be a much more time-consuming endeavor. However, due to the number of edge types available and other conformations variations, much of the vast potential of heterojunction strategies remains unexplored. For this reason, theoretical investigations are in demand to gauge the implications and impact of this new protocol. The successful theoretical description can potentially inspire experimental studies toward these conformations.

1.4.2 Bilayer Stacking

Combining 2D materials into bilayer systems has an enormous potential to generate novel properties. Recent reports on bilayer graphene and other configurations endorse this view. For instance, under a layer misalignment of 1.1^o[61], bilayer graphene may display superconductivity. Control over the layer interaction is also applied to tailor polariton properties[62], to obtain heavy-fermions on van der Waals heterostructures[63], among other modifications on the electronic response[64, 65, 66]. Similar strategies might be applicable to graphene derivatives. In particular, stacking GNRs is a promising route for exploiting the appeal of layer stacking for semiconductor applications, a field in which pristine graphene has limited influence. Figure1.3 illustrates the bilayer of GNRs along with other materials studied in this thesis.

1.5 Molecular Crystals

Another material class of interest is the organic molecular crystals (OMCs). These materials consist of a combination of molecular units held together through a complex balancing of interactions including van der Waals, multipole, π-stacking[67] and even covalent bonding[68]. The OMC properties depend heavily on the attributes of the molecular units and the intermolecular crystalline arrangement[69]. It is known that factors such as lattice spacing, molecular orientation, and anisotropy are crucial for the overall charge transport performance in OMCs[70]. The use of OMCs in optoelectronics is broad, behind promising devices in photovoltaics[67], transistors[71, 72, 73], and flexible electronics[74, 75, 76], where charge transport is, in a way or another, essential to the practical operation. Figure1.3 illustrates the molecular crystals as an molecular matrix.

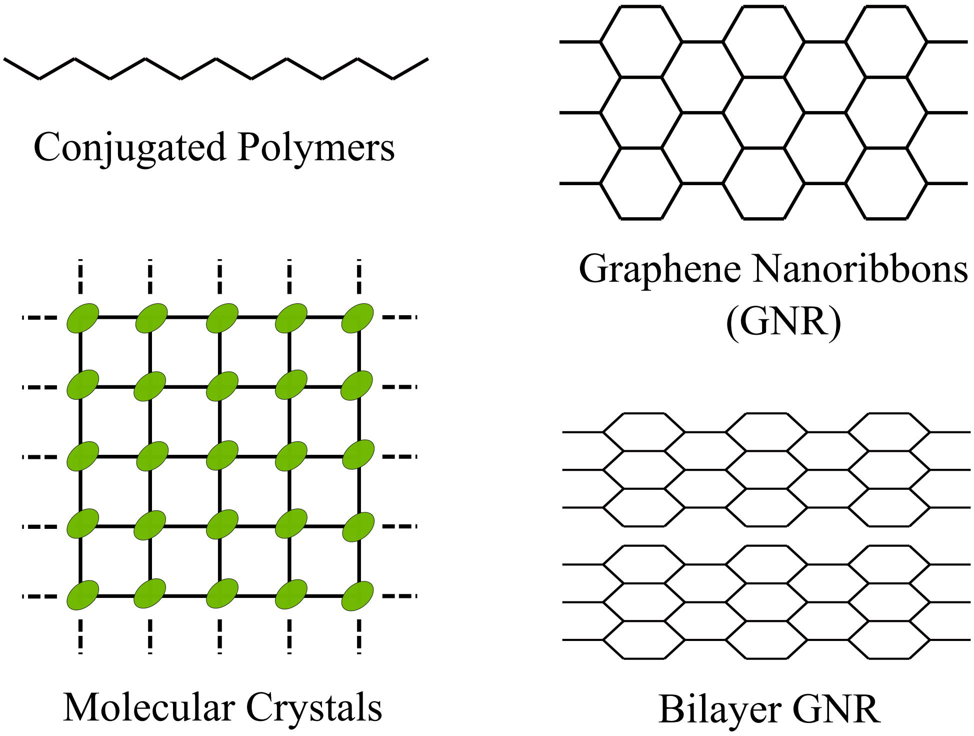

Figure 1.3: Representation of the different materials studied in this thesis.

1.6 Quasiparticles in Highly Confined Materials

Many-body problems in quantum mechanics unfold in a tremendously complicated manner. A detailed description of such systems would require the contemplation of all electrons and nuclei present. However, this approach is impossible when it comes to solids. Interestingly, the charge transport phenomenon in organic compounds is widely different than in inorganic crystals. One of the most distinct characteristics is the lattice response over charge ionization. Organic materials tend to present lattice distortions when it has an unbalanced net charge. That happens because these materials are intrinsically malleable, and such disturbances are energetically favorable[77]. The distortion is a collective response that emerges from the complicated interaction between the charge and the molecule's constituents[78]. All this complexity can be condensed in bounded states of the lattice distortion with charge localization[77] known as quasiparticles. For many purposes, it is highly desirable to proceed with such formalism instead of directly accounting for the complex dynamics of the actual particles (electrons, protons, and neutrons). The advantages of the quasiparticle treatment are even more evident when applied to extended organic molecules such as conjugated polymers, GNRs, and molecular crystals.

1.6.1 Polarons and Bipolarons

Charge, spin, lattice distortion profile and intragap states characterize a quasiparticle. In the case of the charged carriers, they also present specific effective mass and mobility. Regardless of the materials' properties, quasiparticles of the same type have the same charge and spin. On the other hand, the effective mass and mobility highly depend on the host material.

This set of transport properties has an enormous effect on the overall potential of those systems when it comes to semiconducting applications. Other relevant properties include the charge localization and lattice profile deformation associated with the defect.

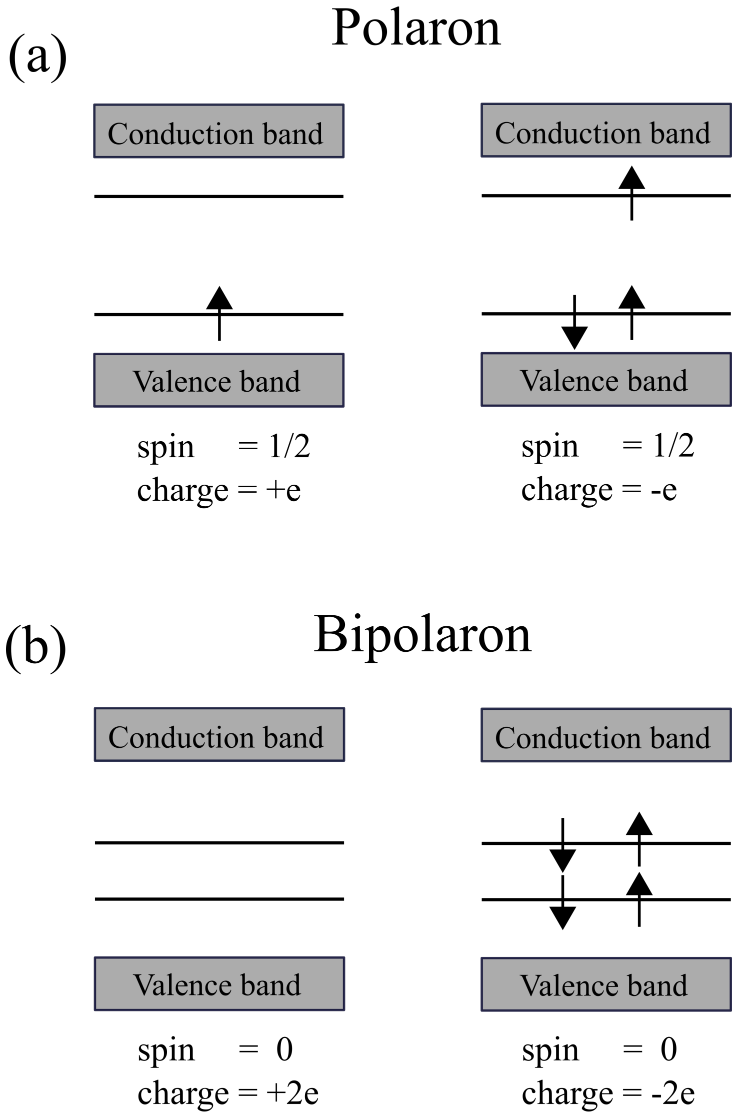

Figure 1.4: Electronic band structure associated with polaron (a) and bipolaron (b). Aside from their different occupations, the quasiparticles differ by their intragap magnitude, which depends on the energetic input associated with its charges.

In this context, the polarons and the bipolarons perform lead roles in many phenomena in materials science. The first one emerges from a single ionization. Thus, it is a half-spin structure with a charge of ±e. The polaron is the main charged quasiparticle, often associated with higher transport regimes due to its lower effective mass. On the other hand, the bipolaron is a spin-less quasiparticle that arises from the bounding of two polaron states with opposite spins. This carrier is especially relevant to the emission mechanism since its recombination may involve the formation of biexciton quasiparticles[79]. Regarding transport, the bipolaron usually has a greater effective mass than a single polaron due to the additional lattice distortion. That additional relaxation is often present in electronic band structure through narrower intragap levels. Depending on the excitation type, the bipolaron charge is ±2e. We illustrate the electronic band structures of these two quasiparticles in Figure 1.4. Different materials can display striking distinct sets of polarons and bipolarons. Probing their properties has proven to be an important step in investigating future materials[44, 80, 81, 82, 83, 84].

The charge transport mechanism has a central role in the viability and efficiency of many optoelectronic applications. As a result, an intense effort was dedicated to investigating the transport of quasiparticles[79, 84, 85, 83, 86, 81, 87]. The studies often aim to characterize the quasiparticles by probing their effective masses and mobility. AGNRs, for instance, are reported to present charge carriers with a width-dependent effective mass. More interestingly, this relationship orders the nanoribbons specimens in the same width families seen in the energy bandgap. Generally, estimates of the effective mass of charge carriers in narrow AGNR are within the range of 0-60 m_e[87], and experimental mobility measures up to $350\,\mathrm{cm}^2/\mathrm{Vs}$[88]. These values indicate efficient carriers when compared with other organic compounds.

When it comes to molecular crystals, charge transport performance is considerably diminished when looking only at the numbers. Most efficient variants have a carrier speed

$\approx$ 2.6 nm/ps[89] and mobilities around $10\,\mathrm{cm}^2/\mathrm{Vs}$[90]. This is due to the lower cohesion between intermolecular units compared to a single atomic crystal. For instance, it is well known that intramolecular mobility is superior to the intermolecular counterpart. However, the use of crystals has its advantages. The most prominent is the ease in the device design, as molecular crystal properties are robust to synthesis defects. The performance of atomic crystals, in turn, is way more sensible to structural flaws.

The technological demand requires a continuous pursuit of more efficient charge carriers. Ideally, charge carriers should be highly mobile. However, another requirement is the presence of a non-zero bandgap. Unfortunately, combining these two demands is a challenging task. As we know, reducing the width of GNRs enforces quantum confinement, which increases the gap. However, the same engineering strategy depletes mobility and increases the effective mass[91, 92, 93]. Similar trade-off scenarios appear when designing molecular crystals. Thus, finding a material with a finite gap and efficient charge carriers is an all-time need for both technological and theoretical purposes.

In face of this scenario, the objective of this thesis is to investigate charge quasiparticles in highly confined materials. The effort will comprise a series of independent works that focus on different aspects of the mechanism. The studies will navigate through four main material classes: conjugated polymers, GNRs, bilayer GNRs and molecular crystals.

1.7 Organization of the Thesis

The proceeding chapters are divided based on the different material classes addressed in the text. Chapter 2 presents the theoretical foundation. We begin by presenting the one-dimensional chain under the tight-binding modeling. Then, the formalism is progressively expanded to include dynamical evolution, 2D lattices, bilayer stacking, and molecular crystals. The next chapters discuss the results obtained. They are grouped based on the type of system being simulated: conjugated polymers (Chapter 3), graphene nanoribbons (Chapter 4), bilayer graphene nanoribbons (Chapter 5), and molecular crystals (Chapter 6). Each chapter provides a brief discussion of the studies, followed by a reference to the corresponding paper. All referenced open access papers are available in the appendix section, organized similarly. We present a cover page for the remaining papers in the appendix indicating where to obtain them at the publisher channels.

CHAPTER 2

THEORETICAL MODELING

Solving the Schödinger equation of the molecular Hamiltonian for extended and highly confined materials is, for most cases, impractical. Moreover, post-HF methods relying on the electronic-nuclear decoupling offered by the Born-Oppenheimer approximation may offer limited insight[94] when it comes to the study the dynamics of coupled states, as the approximation assumes that the electronic wave function changes slowly with respect to the nuclei coordinates when compared to the nuclear wave function. An alternative - and promising - route is to propose model Hamiltonians that replace the *ab initio* treatment to a simplified set of parameterized interactions. Selecting the appropriate interactions and parameters can effectively represent complex physical phenomena through interpretable models. For convenience, lets begin with one of the simplest (yet powerful) models: the tight-binding.

2.1 Tight-binding in a Chain

Consider a single chain of N sites equally spaced by a. Under the approximation of independent electrons, the resulting electronic Hamiltonian (H_{tb}) can be expanded over the basis of localized states $\{|n\rangle\}$ with a defined completeness relation ($\mathbf{1} = \sum_n^N |n\rangle \langle n|$):

$$\begin{aligned} H &= \mathbf{1} H \mathbf{1} \\ &= \sum_{n,n'} \langle n| H |n'\rangle |n\rangle \langle n'| . \end{aligned} \tag{2.1}$$

Since we are under a low-energy regime, it is convenient to disregard any electronic transfer beyond the first neighbors. Moreover, due to the translational symmetry, the hopping probability has to be the same regardless of the site position and the hopping orientation (if it is left or right). Therefore, the matrix elements above are reduced to:

$$\langle n| H |n'\rangle = \begin{cases} -t_0 & \text{if} \quad n = n' \mp 1, \\ \\ 0 & \text{otherwise,} \end{cases} \tag{2.2}$$

where t_0 is the hopping integral associated with the lattice parameter a. Note that diagonal terms were neglected. This choice is reasonable because the sites are identical. In this case, the intra-site energy only modifies the origin of the dispersion relation but poses no relevant changes in the physical description of electronic conduction.

Applying Eq. 2.2 into H_{tb} leads to:

$$
\begin{aligned}
H_{tb} &= \sum_n (-t_0 \left| n+1 \right\rangle \left\langle n \right| + h.c.), \\
&= \sum_n (-t_0 C^\dagger_{n+1} C_n + h.c.),
\end{aligned} \tag{2.3}
$$

where the last line is the Hamiltonian written in second quantization. Therefore, $C^\dagger_{n+1}$ is the fermionic creation operator whose application creates a localized electron state at the site $n+1$ and C_n annihilates a state at the n-th site.

Then, the problem can be solved by finding the corresponding eigenvalue ($\{\epsilon_k\}$) and eigenvector ($\{\left|\psi_k\right\rangle\}$) sets. Due to the translation symmetry, the form of the eigenvectors can be assumed beforehand. Consider the following Bloch functions[95, 96]

$$
\left|\psi_k\right\rangle = \frac{1}{\sqrt{N}} \sum_n e^{ikna} \left| n \right\rangle , \tag{2.4}
$$

such that,

$$
H \left|\psi_k\right\rangle = E^{tb}_k \left|\psi_k\right\rangle . \tag{2.5}
$$

It can be shown that in this case

$$
E^{tb}_k = -2t_0 \cos(ka), \tag{2.6}
$$

which is a continuous function, meaning that each energy value within the range between -$2t_0$ and $2t_0$ has a corresponding electronic state available for the electron occupation. For monovalent atoms, only half of the states will be occupied. In other words, the material is a metal.

Although suitable for some metal-based materials, this projection is not accurate for most organic materials, in particular conjugated polymers[97]. The reason is because they are way more malleable than common metals. Hence, accounting for lattice relaxation becomes imperative. As will be shown in the next section, incorporating this factor results in a new ground-state configuration in which the lattice is rearranged, further lowering the total energy.

2.2 The 1D Su-Schrieffer-Heeger (SSH) Model

The Su-Schrieffer-Heeger [98, 97] (SSH) model provides a reliable route to model the π electrons inside such systems. The modeling consists of building the Hamiltonian H as the sum of two components, the lattice Hamiltonian, H_{latt}, and the electronic one H_{elec}. Here, the former term is modeled over the harmonic approximation, assuming that the inter-site interaction is a sum of harmonic oscillators. This term represents the σ bonds. Then, in other words:

$$H_{lattice} = \frac{1}{2M}\sum_n P_n^2 + \sum_n \frac{K}{2}(u_{n+1} - u_n)^2. \tag{2.7}$$

The first term accounts for the kinetic part, while the latter is the potential one, and

$$\eta_n \equiv u_{n+1} - u_n \tag{2.8}$$

is the deformation of the n-th bond. P_n is the conjugated moment of the n-th site. M and K are the site mass and the spring constant, respectively.

The electronic interaction term is a tight-binding like Hamiltonian which, under the second quantization formalism, reads:

$$H_{elec} = -\sum_{n,s}(t_{n+1,n}C^{\dagger}_{n+1,s}C_{n,s} + h.c.). \tag{2.9}$$

Here $t_{n+1,n}$ is the hopping integral between sites n and $n+1$ and s denotes the spin.

The hopping mechanism depends on the relative distance between neighboring π orbitals, but there is no analytical form for it. However, at low excitation energy regime, the distortion amplitude of σ bonds are up to 2 % of their length[99], allowing to expand $t_{i,j}$ around the undisturbed hopping energy t_0, which gives:

$$t_{n+1,n} = t_0 - \alpha\eta_n. \tag{2.10}$$

This approximate form couples the electronic mechanism with the lattice through this expansion term, where α is the electron-phonon coupling constant. The parameter represents the coupling degree between the two phenomena.

Cis-trans isomerism can be introduced in the model by modifying the hopping term through the Brazovskii-Kirova correction:

$$t_{n+1,n} = (1 + (-1)^n\delta_0)t_0 - \alpha\eta_n, \tag{2.11}$$

where δ_0 is the symmetry breaking term, which controls the isomeric change.

The description of the electronic mechanism is obtained by solving the corresponding time-independent Schrodinger equation. In other words, one must diagonalize H_{elec}. However, to numerically build it up, the spatial configuration of the system, $\{\eta_n\}$, which is a part of the very solution we are searching for, must be known. This coupling demands a self-consistent field (SCF) approach[83, 100, 101, 81, 84]. Moreover, the coupling obliges to solve both lattice and electronic terms simultaneously. Here, we separate the discussion into two types of solutions: the stationary and dynamical states. The next two sections present a brief presentation of the two methods.

2.2.1 Stationary States

The stationary state comprises the configuration when the lattice degrees of freedom are in equilibrium without time-dependent external influence. Therefore, in the stationary state, we set $P_n = 0$ for all n in Eq. 2.7. The stationary algorithm consist on solving simultaneously the electronic and lattice parts until the solution is consistent after a successive iteration step. The electronic states will be determined through the Schödinger equation of H_{elec}

$$H_{elec} \left|\psi_k\right\rangle = E_k \left|\psi_k\right\rangle , \tag{2.12}$$

while the lattice will be calculated through the Euler-Lagrange equations:

$$\frac{d}{dt}\left(\frac{\partial \langle L \rangle}{\partial \dot{u}_n}\right) = \frac{\partial \langle L \rangle}{\partial u_n}. \tag{2.13}$$

Here, $\langle L \rangle$ is calculated using a Slater determinant wave function using the occupied π-electrons. Explicit calculation of Eq. 2.13 leads to[102]

$$\eta_n = -\frac{\alpha}{K} \sum_{k \in occ,s} (\psi_k(n)\psi_k^*(n+1) + c.c.) \equiv -\frac{\alpha}{K}(B_{n,n+1} + c.c.), \tag{2.14}$$

where we had defined

$$B_{n,n+1} = \sum_{k \in occ,s} \psi_k(n)\psi_k^*(n+1), \tag{2.15}$$

in which $\psi_k(n) \equiv \langle n|\psi_k\rangle$. Equation 2.14 provides a way to calculate the lattice degrees of freedom evaluation using the electronic solution.

The stationary algorithm can be summarized in the following steps: (1) take a guess for the set $\{\eta_n\}$ (usually is just η_n=0); (2) build numerically H_{elec}; (3) diagonalize the operator, obtaining the eigenvalues $\{E_{k,s}\}$ and eigenstates $\{\psi_{k,s}\}$; (4) the lattice is then recalculated using Eq. 2.14, generating a new set $\{\eta_n^{new}\}$; (5) check if $\{\eta_n^{new}\}$ is equivalent to $\{\eta_n\}$ under a convergence criteria. if the new lattice is accepted, stationary state is found, otherwise return to step (2) building the Hamiltonian with $\{\eta_n^{new}\}$.

Example: Neutral Solution

It is instructive to compare the results from the SSH model with the equally spaced tight-binding solution (see Section 2.1). In the case of a neutral chain of N sites, the dispersion relation from the traditional tight-binding ($E^{tb}(k)$) and the one obtained through the SSH formalism ($E(k)$) is illustrated in Figure 2.2(a), where the black and red lines refer to, respectively, $E^{tb}(k)$ and $E(k)$. As can be seen, the SSH dispersion is not a continuous function, with notable

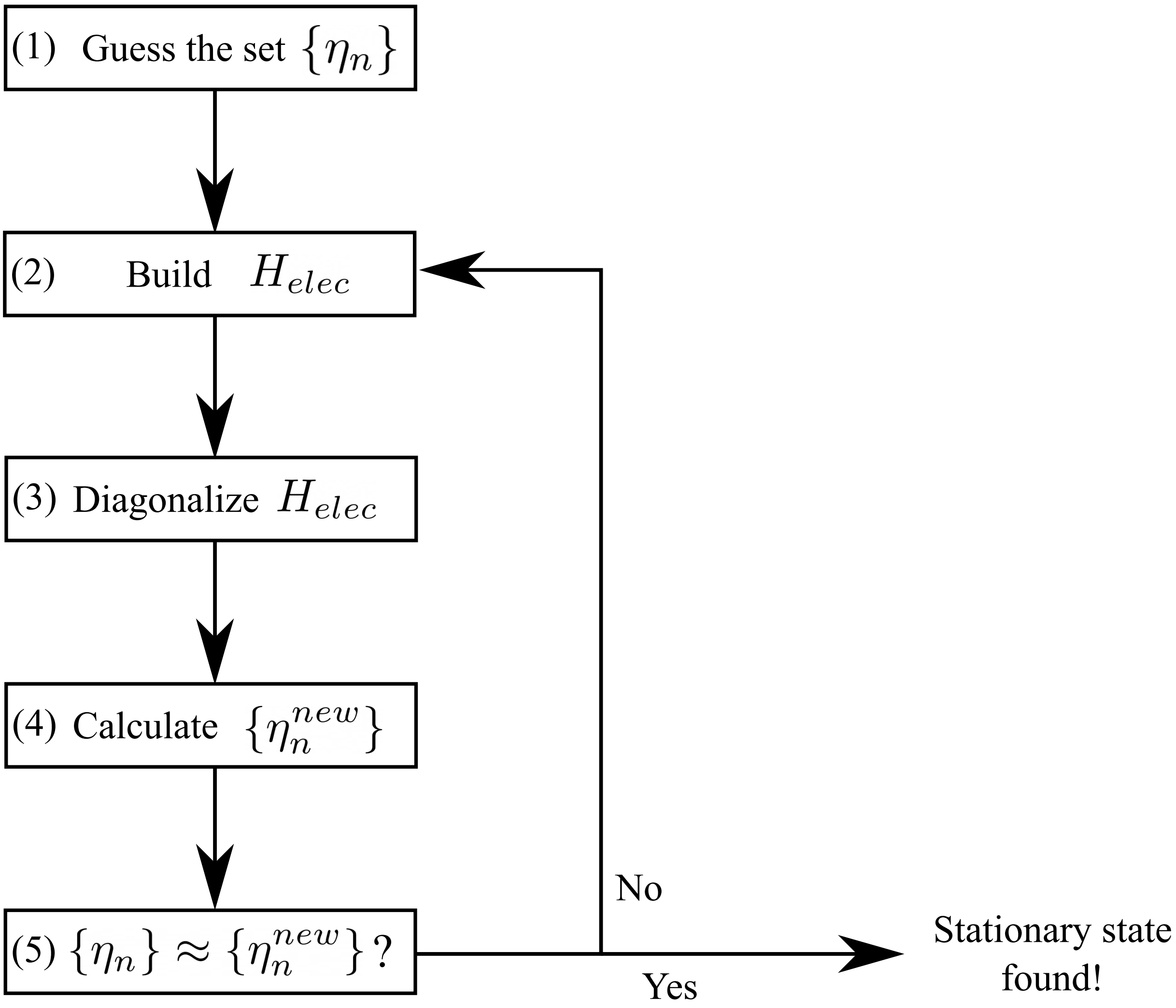

Figure 2.1: Algorithm to find the stationary solutions of the SSH-model Hamiltonian.

breaking points at $k = \pm\pi/2a$. The result is the emergence of a bandgap of magnitude Δ. No electronic state is allowed inside this energy zone. Therefore, lattice relaxation leads to a deeper minimum in which the material exhibits insulator behavior.

The corresponding relaxed spatial configuration is shown in Figure 2.2(b), illustrating the dimer formation. The transition displayed in Figure 2.2 is commonly known as Peierls transition or Peierls instability[95]. It is important to note that a purely electronic tight-binding Hamiltonian can recover the transition. However, this requires a readjustment of the hopping

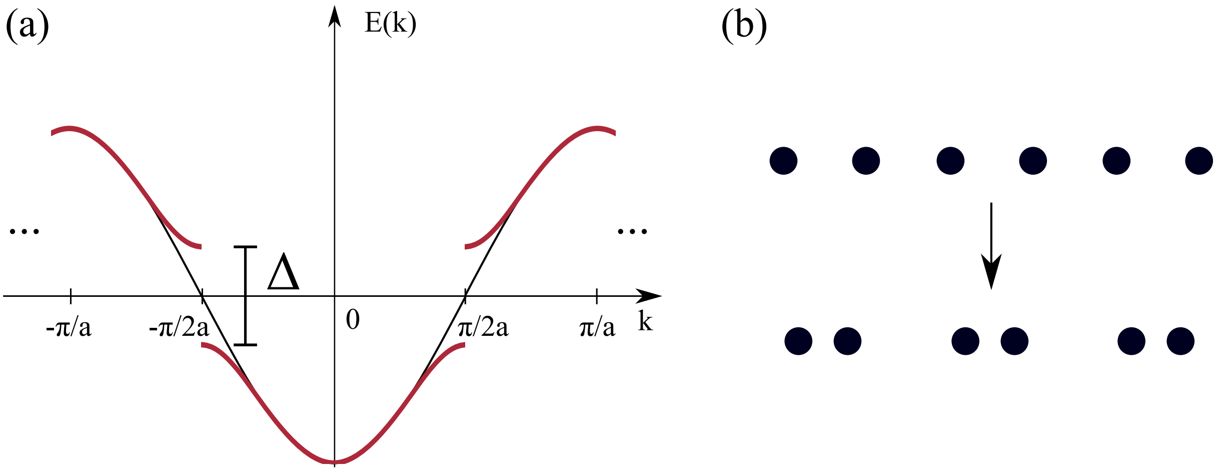

Figure 2.2: (a) Electronic eigenvalues as functions of k for the equally spaced tight-binding (black) and the stationary SSH model (red). (b) comparison between the spatial configuration of two methods.

integral to have parity dependence, hence inducing a symmetry break[95]. On the other hand, the SSH model does not require prior knowledge of the solution, as the transition naturally emerges through the SCF algorithm.

Within the SSH model, the dimerization originates from the effect of the π-electrons on the lattice, through the force balance equation derived form the Euler-Lagrange equations. The expression leads to a condition for bonds depending on their parity: even bonds contract and odd bonds expand (vice-versa). In other words, the lattice solution is

$$\eta_n = (-1)^n (KY_0), \tag{2.16}$$

where Y_0 is the dimerization degree, a constant value that depends on the Hamiltonian parameters.

2.2.2 Dynamical States

The investigation of charge transport requires the time evolution of the stationary charged states, which means evolving both lattice and electronic solutions. Because the phenomena are coupled, we must treat them simultaneously. As discussed earlier, the lattice solution arises from the Euler-Lagrange equations. On the other hand, the electronic states will evolve according to the time-dependent Schrodinger equation.

To this end, the Hamiltonian has to be modified to account for the external electric field $\mathbf{E}(t)$. We begin by assuming a slowly varying potential vector $\mathbf{A}(t)$ and choosing the convenient gauge $\mathbf{E}(t) = -(1/c)\dot{\mathbf{A}}(t)$. That way, the field can be added through the Peierls substitution[103]. Then, the time-dependent effect of the field in the description is to transform the Hamiltonian by the operator

$$\mathbf{U} = e^{\frac{-ie(\mathbf{X}\cdot\mathbf{A})}{c\hbar}}, \tag{2.17}$$

where e is the elementary charge, c is the speed of light, $\hbar$ is the reduced Planck constant, and $\mathbf{X}$ is the position operator. The transformation of H using $\mathbf{U}$ returns the time-dependent Hamiltonian H'

$$H' = -\sum_{n,s}(e^{i\gamma A_x}(t_0 - \alpha\eta_n)C^{\dagger}_{n+1,s}C_{n,s} + h.c.) + \frac{K}{2}\sum_{n}\eta_n^2 + \frac{1}{2M}\sum_{n}P_n^2, \tag{2.18}$$

in which $\gamma = ea/\hbar c$ and A_x is the projection of $\mathbf{A}$ along the σ-bond that connects sites $n+1$ and n. From now on, we will drop the comma on the left side of Eq. 2.18 to ease the notation.

As can be seen, the only change is a phase factor in the hopping term. Then, in other words [81, 99]:

$$t_{n+1,n} \xrightarrow{\text{Field Inclusion}} e^{i\gamma A_x} t_{n+1,n}. \tag{2.19}$$

This new Hamiltonian provides a path to evolve in time the electronic eigenstates and eigenvalues, using the time-dependent Schödinger Equation

$$i\hbar \frac{\partial}{\partial t} \left|\psi_{k,s}(t)\right\rangle = H \left|\psi_{k,s}(t)\right\rangle , \tag{2.20}$$

or, for a small time variation dt,

$$\left|\psi_{k,s}(t+dt)\right\rangle = e^{-iH(t)dt/\hbar} \left|\psi_{k,s}(t)\right\rangle . \tag{2.21}$$

Expanding the right side in terms of the basis that diagonalizes $H(t)$, $\{\phi_l(t)\}$, leads to

$$\left|\psi_k(t+dt)\right\rangle = \sum_l \left\langle \phi_l(t) | \psi_k(t) \right\rangle e^{-i\epsilon_l dt/\hbar} \left|\phi_l(t)\right\rangle , \tag{2.22}$$

where ϵ_l is the l-th eigenvalue of $H(t)$. This equation allows us to evolve $\psi_{k,s}(t)$ in time through incremental steps of dt. We emphasize that during time evolution, the lattice will change. Therefore, the Hamiltonian has to be recalculated and diagonalized at each step. Because of that, the set $\{\phi_l(t)\}$ also evolves in time, requiring the simultaneous solving of lattice and electronic phenomena to progress the system through time.

Because the Hamiltonian is time-dependent, so does the Lagrangian. Time evolution of the lattice arises by reapplying equation 2.13 to the time-dependent $\langle L \rangle$. Ultimately, this provides the following a set of equations of motion for the lattice[104]

$$\begin{aligned} F_n(t) = M\ddot{\eta}_n = K(\eta_{n+1} - 2\eta_n + \eta_{n-1}) \\ + \alpha(\bar{B}_{n+1,n+2} - 2\bar{B}_{n,n+1} + \bar{B}_{n-1,n} + c.c.), \end{aligned} \tag{2.23}$$

where,

$$\bar{B}_{n,n+1} \equiv e^{-i\gamma A_x} B_{n,n+1}. \tag{2.24}$$

Using the equation 2.37 allows to evolve the lattice in time by integrating in time the force to obtain the velocity and position after a dt time step. Dynamics under this formalism have time increments (dt) notably small around $10^{-18}s$. Therefore, Euler's first-order method of integration is suitable to evolve the lattice via Eq. 2.37[105]. In other words, the lattice dynamical variables at the time $t + dt$ are given by

$$\begin{aligned} \dot{\eta}_n(t + dt) = \dot{\eta}_n(t) + \frac{F_n(t)}{M}dt, \\ \eta_n(t + dt) = \eta_n(t) + \dot{\eta}_n(t + dt)dt. \end{aligned} \tag{2.25}$$

The algorithm to obtain dynamical states can be summarized in the following steps: (1) find the stationary solution; (2) calculate $H_{elec}(t)$ (Eq. 2.18); (3) calculate F_n (Eq. 2.23); (4) diagonalize H_{elec} and evolve the electronic states via Eq. 2.22; (5) evolve the lattice using Eq. 2.25; (6) return to step (2) using as input the updated electronic states and lattice coordinates. The loop is maintained to evolve further in time. However, it should be noted that in practical terms one can not simulate arbitrarily long dynamics since successive loops accumulate numerical errors.

As stated earlier, $\mathbf{A}(t)$ must change slowly in time. In that sense, throughout this work we will simulate the conjugated polymers and GNRs under the influence of the following magnetic vector potential[87, 99, 2]:

$$\mathbf{A}(t) = \begin{cases} \mathbf{E_0}(t - (\sin\frac{\pi}{\tau t})(\tau/\pi)) & \text{if } t < \tau \ , \\ \mathbf{E_0}(t - \tau/2) & \text{if } t \geq \tau \text{ and } t < t_{\text{off}}, \\ \frac{\mathbf{E_0}}{2}\left[\left(t - \sin\left(\frac{\pi(t-t_{\text{off}})}{\tau} + \pi\right)\right)(\tau/\pi) + t_{\text{off}} - \tau\right] & \text{if } t \geq t_{\text{off}} \text{ and } t < t_{\text{off}} + \tau, \\ \mathbf{E_0} t_{\text{off}} & \text{if } t > t_{\text{off}} + \tau \ , \end{cases} \tag{2.26}$$

in which τ is a time parameter that controls the function smoothness, and t_{off} is the time set to the electric field to be shutdown. For most cases, τ represents at most 5 % of the simulation duration time, meaning that the values of t_{off} depend on the phenomena studied. Charge transport simulations tend to have t_{off} set to be the duration of the entire simulation. This represents something around 400-600 fs.

2.3 Semi-classical Transport Model of Quasiparticle Drifting

The formation of charged quasiparticles enforcers a local lattice deformation that traps the charge. This stable couple structure maintains its spatial profile unchanged during the motion in the absence of collisions. As long as stability is assured, the dynamics of the bound state can be represented as the trajectory of a point located at the defect center position. Therefore, the particle motion can be approximated to a classical projectile experiencing a dissipating force [87, 102]. According to Newton's second law, the dynamics of a particle, with charge q, under the influence of a uniform electric field of strength E_0 is

$$M_{eff}\ddot{X} = qE_0 - Bv_x, \tag{2.27}$$

in which M_{eff} is the carrier's effective mass, B is the dissipating coefficient, $\ddot{X}$ is the quasiparticle's acceleration, and v_x is its velocity along the electric field's direction. Solving the differential equation gives the dependency of position (X) with time, which reads [106, 87]

$$X(t) = X_0 + v_t t + \frac{v_0 - v_t}{k}(1 - e^{-kt}). \tag{2.28}$$

Here, X_0 and V_0 are the quasiparticle's position and velocity at the instant that the electric field becomes constant, respectively. Finally, v_t is the terminal velocity, and k is the mass-weighted dissipation coefficient. Fitting this function to the motion of the charge carrier allows us to obtain v_t and k. With these parameters, one can estimate important transport-related properties as shown in what follows. From the definition of terminal velocity, Equation 2.27 turns in

$$0 = qE_0 - Bv_t \Rightarrow v_t = qE_0/B. \tag{2.29}$$

Simple manipulation of this relation with the fitted parameters returns B. Since $k = B/M_{eff}$, knowing these two quantities indirectly determines M_{eff}. The fitted coefficients are also able to give an estimate of mobility. For this, we must first realize that the terminal velocity is an estimate of the drift velocity when neglecting the collisions between quasiparticles and any other source of scattering. Then, following the definition of mobility (μ), we get

$$\mu = v_t/E_0. \tag{2.30}$$

Having v_t also allows calculating other transport-related properties. Let λ be the linear charge density in the nanoribbon. The current (I) of this steady flow is

$$I = v_t\lambda. \tag{2.31}$$

The charge density along the chain is equal to the unit cell's density for a steady regime. Thus, if L_0 and Q are, respectively, the length of the unit cell and the charge inside it, we reach

$$\lambda = Q/L_0. \tag{2.32}$$

Using this relation in Eq. 2.31 leads into

$$I = v_tQ/L_0. \tag{2.33}$$

In addition to current, we are also able to obtain the voltage (V). During the constant electric field regime, the ends of the nanoribbon can be considered capacitor terminals. Let L_{tot}

be the length of the entire material. The potential between the two extremities is

$$V = L_{tot} E_0. \tag{2.34}$$

In most cases, the length of the unit cells does not exactly add up to L_{tot}. However, as an approximation, V can be estimated considering the closest sum of unit cells that narrows to the system's real length.

2.4 2D SSH Hamiltonian

The extension for a two-dimensional lattice consists of adapting both electronic and lattice interactions to consider new neighbors. The Hamiltonian becomes[105, 99, 101, 42, 107]

$$H = -\sum_{<i,j>,s} (t_0 - \alpha \eta_{i,j})(C_{i,s}^{\dagger} C_{j,s} + h.c.) + \sum_i \frac{P_i^2}{2M} + \sum_{<i,j>} \frac{K}{2} \eta_{i,j}^2, \tag{2.35}$$

where i and j index lattice sites and the summation on $< i, j >$ is done over the first neighbors. Note that in contrast to the one-dimensional formulation, the 2D Hamiltonian requires two indices to map the bonds along the lattice. In particular, $\eta_{i,j}$ corresponds to the bond length deformation along the line connecting sites i and j. Here, we had used the small oscillations approximation, meaning that only the deformation at the $i - j$ line is accounted for evaluating $\eta_{i,j}$. In other words, this disturbance is the difference between the lattice position of sites i and j (projected in the i-j line). Figure 2.3 illustrates the summing procedure. A graphene slice is presented, highlighting the i-th site and immediate vicinity.

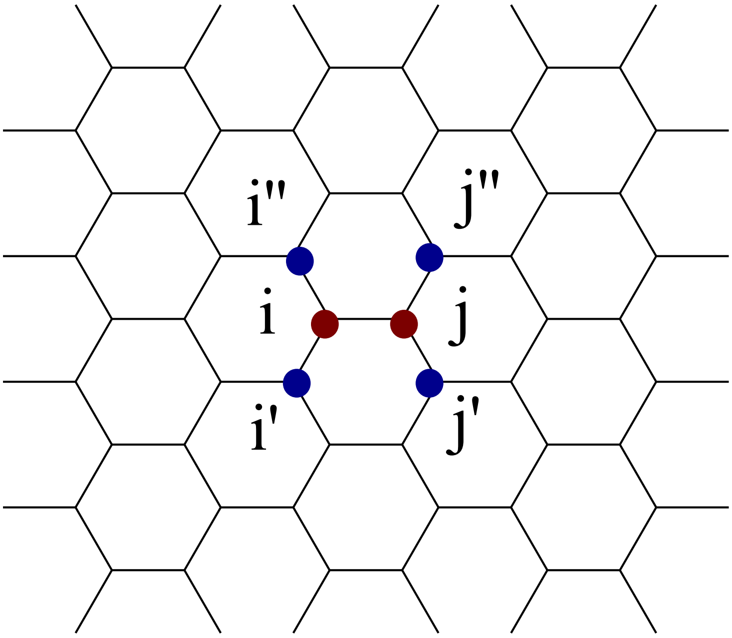

Figure 2.3: Site indexing in hexagonal lattice.

In general, the SSH formalism remains intact with the extension for two dimensions. This means that both stationary and dynamical algorithms of the 1D case are applicable here. The difference arises only in the form of the new expressions used during the algorithms' steps.

The relation obtained from the application of the Euler-Lagrange equations is[108]:

$$\eta_{i,j} = -\frac{\alpha}{K}(B_{i,j} + c.c.). \tag{2.36}$$

As for time evolution, the quantum states will be evolved following Eq. 2.22. The only difference is in the form of Hamiltonian operator responsible for the time translation, which now assumes the 2D form of Eq. 2.35.

Finally, the lattice dynamics for the sites linked with three neighbors will be updated via the following equations of motion[104]:

$$
\begin{aligned}
F_{i,j}(t) = M\ddot{\eta}_{i,j} = \frac{K}{2}(\eta_{i,i'} + \eta_{i,i''} + \eta_{j,j''} + \eta_{j,j'} - 4\eta_{i,j}) \\
+ \frac{\alpha}{2}(\bar{B}_{i,i'} + \bar{B}_{i,i''} + \bar{B}_{j,j'} + \bar{B}_{j,j''} - 4\bar{B}_{i,j} + c.c.),
\end{aligned}
\tag{2.37}
$$

where the expression follows the site indexing presented in Figure 2.3 and

$$
\bar{B}_{i,i'} = e^{i\gamma A_{i,i'}} B_{i,i'},
\tag{2.38}
$$

in which $A_{i,i'}$ is the projection of the potential vector along the direction connecting sites i and i'. Note that, in contrast with the 1D case, the relative orientation between sites changes according to the site pairing, i.e. the projection along the line connecting sites i and j is linearly independent of the i-i' line. Therefore, electric fields with components orthogonal to the i-j line can still alter the dynamics of the bond connecting i and j.

2.5 Bilayer Stacking

GNRs bilayers can be modeled under the SSH formalism. Consider a bilayer formed by two layers: A and B. The corresponding Hamiltonian becomes the sum of the monolayer operators (given by Eq. 2.35) and an interaction term connecting them. In other words,

$$
H_{\text{bilayer}} = H_{SSH,A} + H_{SSH,B} + H_{inter},
\tag{2.39}
$$

where (for $l = A, B$)

$$H_{SSH,l} = -\sum_{<i,j>,s} t_{l,i,j}(C_{i,s}^{l\dagger} C_{j,s}^{l} + h.c.) + \sum_i \frac{P_i^2}{2M} + \sum_{<i,j>} \frac{K}{2}\eta_{i,j}^2, \tag{2.40}$$

in which all the sums are over sites within the same layer (l).

The interlayer interaction is purely electronic since the layers are not bonded by covalent links. The term is represented by a tight-binding interaction. Assuming a AA stacking, where the layers are paired site-per-site, this contribution becomes:

$$H_{inter} = -\sum_{i,i_\perp,s} t_\perp(C_{i,s}^{A\dagger} C_{i_\perp,s}^{B} + h.c.), \tag{2.41}$$

where each i site, belonging to layer A, is linked to its immediate interlayer first neighbor $i_\perp$. Figure 2.4 illustrates the convention for the 4AGNR bilayer. In 2.4(a), a top view of the system is shown. Besides sites at the border, every i-th site has three first intralayer neighbors, represented by j, j', and j''. Figure 2.4(b) shows the bilayer in a rotated perspective, where the two layers (A and B) are visible. Here, each i-th site is paired with its interlayer first neighbor $i_\perp$, which is at the same position as i at the plane shown in 2.4(a). It is worth mentioning that “layer A" and “layer B" are mere labels for convenience since the Hamiltonian is invariant by layer exchange.

The solving algorithm is the same as the monolayer case. The only difference is the form of the electronic Hamiltonian. As a result, the influence on the SCF solution from the interlayer configuration will be expressed in the π-electron force field term, given by the set

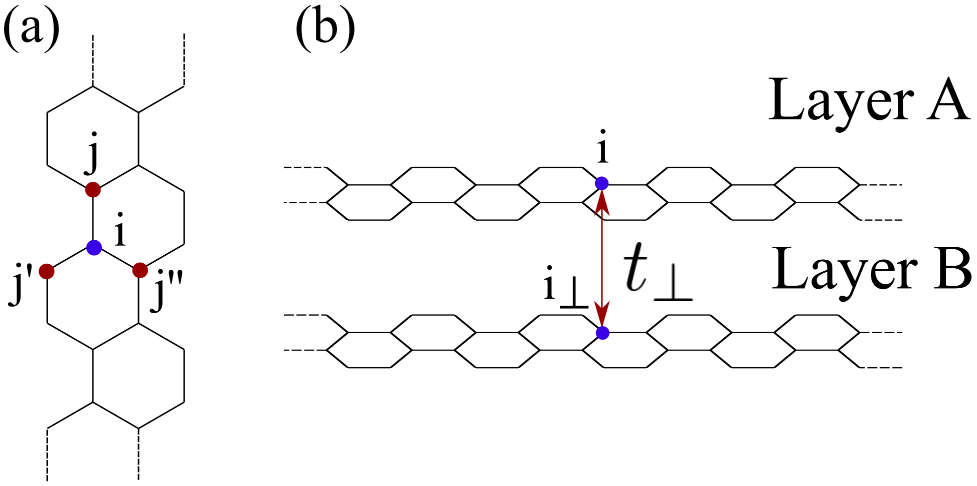

Figure 2.4: Representation of graphene as a combination of infinite polymers connected vertically[6].

$\{B_{i,j}\}$ since the new Hamiltonian will yield different eigenvectors.

2.6 Molecular Crystals

Molecular crystals can be modeled following the same premises behind the SSH formalism. The main modification is that the modeling for crystals explicitly considers the internal degrees of freedom of each site. The resulting Hamiltonian (H_{HP}), known as the Holstein-Peierls operator, is the sum of two contributions: the intramolecular (H_{intra}) and intermolecular (H_{inter}). In the two components, there are lattice ($H^{latt}_{intra/inter}$) and electronic ($H^{elec}_{intra/inter}$) contributions such that[109, 89, 8]

$$H_{HP} = H_{inter} + H_{intra}, \tag{2.42}$$

in which,

$$
\begin{aligned}
H_{intra} &= H^{elec}_{intra} + H^{latt}_{intra}, \\
H_{inter} &= H^{elec}_{inter} + H^{latt}_{inter}.
\end{aligned}
\tag{2.43}
$$

The explicit form of $H^{latt}_{intra/inter}$ and $H^{elect}_{intra/inter}$ depend on the particular crystal morphology, dimension, and the presence (or not) of external agents. Here, let's consider the two-dimensional square lattice, as depicted in Figure 2.5(a). The system is represented as a molecular grid. Each site is a molecular unit indexed by the corresponding row and column position within the molecular matrix. The element (i, j) is centralized in the figure. All sites are surrounded by four first neighbors. In the case of (i, j), they are the $(i + 1, j)$, $(i - 1, j)$, $(i, j + 1)$, and $(i, j - 1)$. These sites are connected by a tight-binding hopping given by[89, 110]

$$
\begin{aligned}
H^{elec}_{inter} = &\sum_{i,j} (J^{x}_{i+1,j} C^{\dagger}_{i+1,j} C_{i,j} + h.c.) + \\
&+ \sum_{i,j} (J^{y}_{i,j+1} C^{\dagger}_{i,j+1} C_{i,j} + h.c.),
\end{aligned}
\tag{2.44}
$$

in which $J^{x}_{i+1,j}$ is the hopping amplitude for an electron transfer from the site (i, j) to its neighbor $(i + 1, j)$ and $J^{y}_{i,j+1}$ corresponds to the hopping $(i, j) \to (i, j + 1)$. In the tight-binding description, the basis consists of a set of localized states. Here, $C^{\dagger}_{i+1,j}$ corresponds to the creation operator of the lowest unoccupied molecular orbital (LUMO) at the site $(i+1, j)$. Analogously, $C_{i,j}$ is the annihilation operator, whose application removes the LUMO from the site (i, j).

The lattice degrees of freedom are treated under the harmonic approximation. In other words, H^{latt}_{inter} is a combination of harmonic oscillators of mass M_{inter} and spring constant

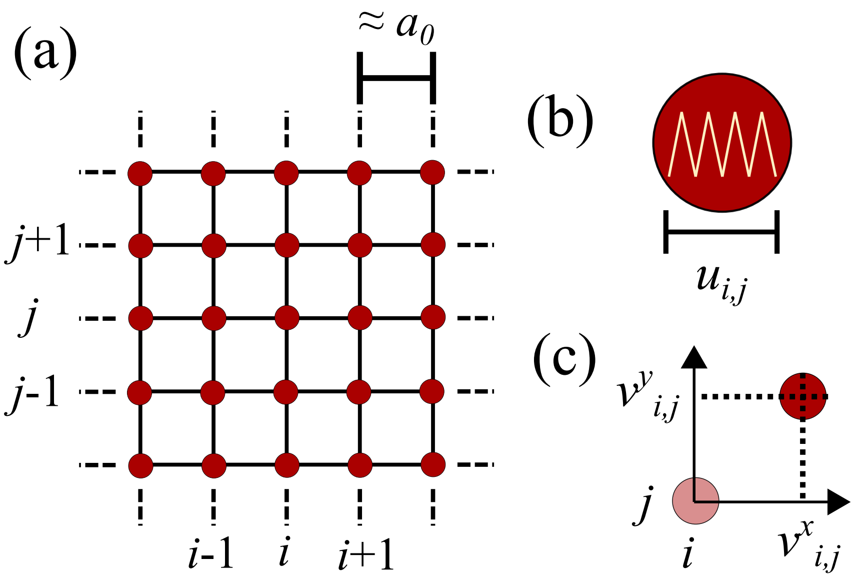

Figure 2.5: Illustration of the molecular crystain within the Holstein-Peierls model. (a) presents the square lattice. (b) highlights the site (i,j), evidencing its internal lattice degree. (c) presents the intermolecular lattice variables.

K_{inter}:

$$H^{latt}_{inter} = \frac{K_{inter}}{2}\sum_{i,j}(\Delta x_{i,j})^2 + \frac{K_{inter}}{2}\sum_{i,j}(\Delta y_{i,j})^2 + \\ + \frac{1}{2M_{inter}}\sum_{i,j}(P^x_{i,j})^2 + \frac{1}{2M_{inter}}\sum_{i,j}(P^y_{i,j})^2. \tag{2.45}$$

As illustrated in 2.5(b), $v^{x/y}_{i,j}$ is the lattice displacement, with respect to the pristine configuration of the site (i,j) at the x/y-direction. In addition, $\Delta x_{i,j} \equiv v^x_{i+1,j} - v^x_{i,j}$ is the corresponding bond displacement of the link connecting the sites (i,j) and $(i+1,j)$, while $\Delta y_{i,j} \equiv v^y_{i,j+1} - v^y_{i,j}$ is the corresponding distortion for the vertical bond (i,j)-$(i,j+1)$. Moreover, $P^{x/y}_{i,j}$ is the x/y momentum of the site (i,j).

The intramolecular component is treated in the similar way. The intramolecular lattice component is[89, 111]

$$H_{intra}^{latt} = \frac{1}{2M_{intra}} \sum_{i,j} (P_{i,j}^{u})^2 + \frac{K_{intra}}{2} \sum_{i,j} u_{i,j}^2, \tag{2.46}$$

where M_{intra} is the internal oscillator mass, K_{intra} its corresponding spring constant, $u_{i,j}$ is the oscillator deformation, and $P_{i,j}^{u}$ is the corresponding intramolecular momentum, as depicted in Figure 2.5(c).

Finally, the electronic intramolecular term is an intrasite term to the Hamiltonian calibrated by the intramolecular electron-phonon coupling α_{intra}. The interaction reads:

$$H_{intra}^{elec} = \sum_{i,j} \alpha_{intra} u_{i,j} (C_{i,j}^{\dagger} C_{i,j}). \tag{2.47}$$

such that $H^{elec} = H_{intra}^{elec} + H_{inter}^{elec}$.

Similar to the organic atomic crystals, organic molecular crystals are malleable. For this reason, it is convenient to consider the spatial dependence of the hopping terms in a protocol equivalent to the one shown in Section 2.2. Moreover, the presence of an external electric field can be included by adding a time-dependent phase into the hopping, as shown in Section 2.2.2. Here, consider the case where the electric field is aligned with the x-direction. Then, we may define the potential vector $A_x(t) = -cE_{x0}t$, where E_{x0} is the corresponding electric field strength. Specifically, these modifications lead to the following hopping integrals[103]:

$$\begin{aligned} J_{i+1,j}^{x} &= (J_0^{x} - \alpha_{inter}(v_{i+1,j}^{x} - v_{i,j}^{x}))e^{i\gamma A_x(t)}, \\ J_{i,j+1}^{y} &= (J_0^{y} - \alpha_{inter}(v_{i,j+1}^{y} - v_{i,j}^{y})). \end{aligned} \tag{2.48}$$

As discussed in Section 2.2.1, the electronic and lattice parts of a hybrid Hamiltonian have to be solved simultaneously to obtain the stationary states. This is an unavoidable constraint since the two mechanisms are explicitly coupled. Here, the backpropagation algorithm is applied to this task[112, 109].

Time evolution is done by simultaneously applying the time-dependent Schödinger equation to the electronic states and calculating the lattice dynamics through the Euler-Lagrange equations. The procedure is analogous to the one presented in Section 2.2.2. For a time increment dt, the electronic state $|\psi(t)\rangle$ evolves as:

$$|\psi(t+dt)\rangle = e^{-iH^{elec}(t)dt/\hbar}\,|\psi(t)\rangle\,. \tag{2.49}$$

After adding the completeness relation of the instantaneous eigenstates $1 = \sum_l |\phi_l(t)\rangle\,\langle\phi_l(t)|$, such that $H^{elec}\,|\phi_l(t)\rangle = \epsilon_l(t)\,|\phi_l(t)\rangle$, the expression can be written as

$$|\psi(t+dt)\rangle = \sum_l e^{-i\epsilon_l(t)dt/\hbar}\,\langle\phi_l(t)|\psi(t)\rangle\,|\phi_l(t)\rangle\,. \tag{2.50}$$

Explicit application of the Euler-Lagrange equations yields the force at the intra and intermolecular lattice degrees of freedom, determining their evolution. For the intermolecular part, the corresponding equations of motion in the x-direction are[109]:

$$\begin{split} M_{inter}\ddot{v}^x_{i,j}(t) = -K_{inter}(2v^x_{i,j}(t) - v^x_{i+1,j}(t) - v^x_{i-1,j}(t)) + \\ - \alpha_{inter}([\rho_{i,j,i-1,j}(t) - \rho_{i+1,j,i,j}(t)]e^{-i\gamma A_x(t)} + c.c.). \end{split} \tag{2.51}$$

The y-direction has a similar form, expect for absence of the time-dependent term from the electric field:

$$\begin{aligned} M_{inter}\ddot{v}^{y}_{i,j}(t) = -K_{inter}(2v^{y}_{i,j}(t) - v^{y}_{i,j+1}(t) - v^{y}_{i,j-1}(t)) + \\ - \alpha_{inter}(\rho_{i,j,i,j-1}(t) - \rho_{i,j+1,i,j}(t) + c.c.). \end{aligned} \tag{2.52}$$

The intramolecular equations of motion are:

$$M_{intra}\ddot{u}_{i,j}(t) = -K_{intra}u_{i,j}(t) - \alpha_{intra}\rho_{i,j;i,j}. \tag{2.53}$$

Note that the forces are the balance between the lattice and the electronic contributions. The term $\rho_{i,j,m,n}(t)$ represents the element (i,j,m,n) of the charge density molecular matrix. In other words,

$$\rho_{i,j,m,n}(t) = \psi(i,j,t)\psi(m,n,t)^{*}, \tag{2.54}$$

where

$$\psi(i,j,t) = \langle i,j|\psi(t)\rangle \tag{2.55}$$

is the projection of the molecular eigenstate at the site (i,j).

Note that, in contrast to the SSH model, the bond forces shown in Eqs. 2.51,2.52, and 2.53 depend only of a single wavefunction, as evidenced in Eq. 2.54. The reason for this is because the sites of π-systems, such as graphene and polyacetylene, contribute with one electron each. In other words, a neutral π-system of size N has N available π-electrons. Consequently, the lattice dynamics will depend of the electronic cloud encompassing all the electrons, as demonstrated in Eq. 2.37. In the present Hostein-Peierls model, only intermolecular excitations contribute to the charge net. Therefore, when there is a single polaron excitation in the molecular matrix, only this specific molecular orbital influences the lattice dynamics.

The algorithm to progress the molecular crystal in time is equivalent to the SSH model: (1) calculate the stationary solution; (2) numerically build $H^{elec}(t)$; (3) calculate the intra and inter motion equations (Eq. 2.53, 2.51 and 2.52); (4) diagonalize H^{elec} and evolve the electronic states via Eq. 2.50; (5) evolve the lattice via the Verlet algorithm; (6) return to step (2) using as input the updated electronic states and lattice coordinates

CHAPTER 3

RESULTS: CONJUGATED POLYMERS

3.1 A New Interpretation for Quasiparticle Physics

In the stationary state, we recall that the lattice is calculated through a force balance equation:

$$K\eta_n = -\alpha(B_{n,n+1} + c.c.). \tag{3.1}$$

The left side is a classical spring force. On the other hand, the right side is the force (of electronic origin) derived from the π-electrons' wave function (Π_n):

$$\Pi_n = \alpha(B_{n,n+1} + c.c.). \tag{3.2}$$

In the neutral SCF solution for a general conjugated polymer, Π_n assumes an alternating form (see Section 2.2.1), giving rise to bond conjugation:

$$\Pi_n^N = (-1)^n K Y_0. \tag{3.3}$$

In other words, the π-electron force field is constant for a given site parity. This solution suggests interpreting the model as a set of classical harmonic oscillators under a constant force field. Note that the configuration is strikingly similar to an ordinary oscillator subjected to uniform gravity.

This realization indicates the existence of an analytical function for Π_n equivalent to the numerical evaluation of Eq. 2.14. Toward this generalization, the force fields of quasiparticle solutions are considered. Analysis shows that the only difference in the force field, compared to the neutral case, is the presence of a local disturbance in Π_n^N. Then, we propose the following general formula for a π-force field:

$$\Pi_n = \Pi_n^N + \Pi_n^P, \tag{3.4}$$

where Π_n^P is a pulse that is set to travel through the sites representing the quasiparticle motion.

Results show that the appropriate choice for Π_n^P is equivalent to the conventional approach for the SSH model. With this confirmation, the work proposes a new interpretation for quasiparticles as local disturbances in the effective field of the π-electrons. More details are in our published article, also present in appendix A.1.

CHAPTER 4

RESULTS: GRAPHENE NANORIBBONS

4.1 Charge Transport in Cove-type Graphene Nanoribbons

Understanding the charge transport mechanism in CGNRs is a pivotal step for their effective use in high-end optoelectronic devices. Toward this goal, it is desirable to characterize the charge carriers and estimate their responses under diverse electric field regimes. Characterizing mobility and effective mass is crucial for understanding charge transport, as it provides essential insights into the material's transport properties and potential applications. In this paper, we simulated the charge transport of polarons and bipolarons hosted on cove-type GNRs. The study begins with the characterization of the carriers in the stationary state. Analysis shows that polarons are wider than bipolarons, hinting at a potential disparity in the transport performance.

This hypothesis is tested by evolving the states in time under the influence of an external electric field. Results show that polarons are faster than bipolarons, an expected result considering previous studies on conjugated polymers. Additionally, the quasiparticles' mobilities were calculated for different electric field strength regimes using the semi-classical model of quasiparticle transport exposed in section 2.3. Results show that the carriers may exhibit excellent mobility values, corroborating experimental observation. Moreover, the simulation indicates that the good performance is mainly due to the polarons. Our published article presents a comprehensive discussion of the findings[2]. Information of the paper can be found in appendix B.1.

4.2 Heterojunction Engineering to Design GNRs for Efficient Charge Transport

The recent advances in the GNR synthesis suggest that strong control of the nanoribbon's shape is attainable, allowing atomic-level design. The heterojunction technique is of special promise, allowing the combination of two nanoribbon types —each with potentially distinct properties— into a new GNR. In this context, we proposed in this work a heterojunction rule that combines different shapes of cove-type GNRs. The charge transport performance is evaluated by the simulation of dynamical polaron states under the SSH model. Mobility calculations show that heterojunction can be a tool for fine-tuning the transport efficiency. Additionally, we reported that forcing asymmetrical unit blocks may induce a change in the transport mechanism regime, in which the polaron hops through minor domains within the nanoribbon. The results presented are discussed in detail in our published article[3]. Information of the paper can be found in appendix B.2.

4.3 Parametrizing Graphene Nanoribbons into 1D Chains

The charge transport on GNR heterojunctions is one-dimensional. Therefore, although the material is 2D, it should be possible to describe the transport mechanism in terms of a one-dimensional representation. In this work, we investigated this reasoning for the heterojunction rule proposed in [3]. The idea is to recover the quasiparticle physics delivered through the SSH 2D model using a parametrized 1D SSH model. Toward a 1D description, the heterojunction's building blocks are mapped to sites. The site's mass equals the entire block's mass. An adjusted lattice parameter, determined by the length of the GNR building blocks, separates the sites in the chain. The 1D electron phonon constant (α^{1D}) and the spring constant of the 1D model (K^{1D}) are left as free parameters.

We report that an appropriate choice for α^{1D}-K^{1D} recovers the dynamics from the 2D model. This robustness remains for all heterojunction pairs considered. The proposed mapping presents a more simplified mechanism for quasiparticle dynamics. This allows direct comparison between different conformations. In other words, the influence of geometrical changes on the polaron transport becomes more transparent. The simplified picture allowed the recognition of heterojunction families in which the fitted parameters follow a predictable monotonic trend. The results presented are discussed in detail in our published article[4]. Information of the paper can be found in appendix B.3.

4.4 Thermal Effects on Polarons and Bipolarons Stability

The functioning of optoelectronic devices often relies on the thermal properties of the materials. Therefore, physical modeling that explicitly takes into consideration the presence of thermal influence is of paramount importance. In this work, we propose an extension for the SSH model in which thermal effects are treated as random lattice distortions of the stationary solutions. Different deformations are sampled, forming an ensemble. Statistical evaluation of physical quantities within the set represents the thermal effects. We illustrate the use of the method by applying it to armchair graphene nanoribbons.

The findings reveal that lattice thermal disturbances greatly alter the polaron and bipolaron charge densities and their lattice localization profiles. In addition, it is found that the conjugation is affected differently, depending on the nanoribbon width. The wider the GNR, the more prone to dimerization loss the specimen becomes. Therefore, we report that narrow nanoribbons are more mechanically stable. Moreover, the formation energies over the polaron and bipolaron ensembles are estimated. Results show that temperature enhances the dispersion of these curves, eventually inducing an overlap. The resulting bipolaron stability becomes affected, allowing positive values. In other words, temperature seems to energetically favor the formation of two independent polarons instead of a bipolaron. The findings are discussed in detail in our published article[5]. Appendix B.4 presents the paper.

CHAPTER 5

RESULTS: BILAYER GRAPHENE NANORIBBONS

5.1 Phase Transition of Polarons in Bilayer Graphene Nanoribbons

In this paper, we investigated the effects on the polaron profile after stacking identical GNRs in an AA formation. The interlayer interaction is a tight-binding term controlled by $t_{\perp}$ (see Section 2.41). We report that two types of interlayer polarons are possible: symmetric and non-symmetric. The symmetric type has an equal amount of charge shared between the layers, while the non-symmetric has an uneven distribution. $t_{\perp}$, which can be interpreted as a degree of proximity, mediates the transition between the solutions. Analysis of the electronic band structure and charge localization profiles determines the domains where each solution is dominant. Besides serving as a theoretical foundation, the work also hints at the potential use of bilayer GNRs on novel optoelectronic applications. The results presented here are discussed in detail in our published article[6]. The paper information can be found in appendix C.1.

5.2 Strain-Tuneable Bipolaron Stability on Bilayer Graphene Nanoribbon

The results discussed for the polaron[6] indicate that the stability of quasiparticles may greatly depend on the interlayer spacing regime. In this work, the bipolaron stability is compared to polarons on ultra-narrow GNR bilayers. Results show that symmetric bipolarons are more stable than two symmetric polarons. This result is especially relevant for optical applications since bipolarons are active agents in emission mechanisms. Controlling their stability via strain could tune the GNR optical properties, allowing the development of wearable devices and other strain-based gadgets. The results presented here are discussed in detail in our published article[7]. Information of the paper can be found in appendix C.2.

CHAPTER 6

RESULTS: MOLECULAR CRYSTALS

6.1 Large polarons in two-dimensional fullerene networks: The crucial role of anisotropy in charge transport

A recent report presented the synthesis of a novel fullerene crystal[68]. In this configuration, the crystalline cohesion is sustained through covalent bonds instead of the weak van der Waals interactions. As it is, the material holds great promise for nanotechnology. The appeal is particularly relevant for semiconducting applications since the reported material has a bandgap of $\approx$ 1.6 eV[113, 114]. However, the performance pertaining to charge transport remained unclear to this point. In this work, we applied the Holstein-Peierls model to simulate the crystal and infer its capabilities for future integration in the industry. Results show that polaronic transport is feasible in the crystal, with transport velocities around 0.5-1.5 nm/ps. Moreover, it is found that electronic anisotropy is crucial for functioning transport. The results presented here are discussed in detail in our published article[8]. Information of the paper can be found in appendix D.1.

Bibliography

[1] Tiago de Sousa Araújo Cassiano, Pedro Henrique de Oliveira Neto, and Geraldo Magela e Silva. Quasiparticle dynamics by effective π-field distortion. Scientific Reports, 12(1):7967, 2022.

[2] Tiago de Sousa Araújo Cassiano, Leonardo Evaristo de Sousa, Luiz Antônio Ribeiro Junior, Geraldo Magela e Silva, and Pedro Henrique de Oliveira Neto. Charge transport in cove-type graphene nanoribbons: The role of quasiparticles. Synthetic Metals, 287:117056, 2022.

[3] Tiago de Sousa Araújo Cassiano, Luiz Antônio Ribeiro Júnior, Geraldo Magela e Silva, and Pedro Henrique de Oliveira Neto. Regulating polaron transport regime via heterojunction engineering in cove-type graphene nanoribbons. Advanced Theory and Simulations, 6(6):2200877, 2023.

[4] Tiago de Sousa Araujo Cassiano, Pedro Henrique de Oliveira Neto, and Geraldo Magela e Silva. Quasiparticles in graphene nanoribbon heterojunctions: Insights from a simplified one-dimensional model. The Journal of Physical Chemistry C, 127(29):14293–14302, 2023.

[5] Tiago de Sousa Araújo Cassiano, Geraldo Magela e Silva, and Pedro Henrique de Oliveira Neto. Thermally-induced charge carrier population control on graphene nanoribbons. Materials Advances, 2024.

[6] Tiago de Sousa Araújo Cassiano, Geraldo Magela e Silva, and Pedro Henrique

de Oliveira Neto. Phase transition of polarons in bilayer graphene nanoribbons. Physica Scripta, 98(9):095922, 2023.

[7] Tiago de Sousa Araujo Cassiano, Luiz Antonio Ribeiro Junior, Geraldo Magela e Silva, and Pedro Henrique de Oliveira Neto. Strain-tuneable bipolaron stability on ultranarrow bilayer graphene nanoribbon. The Journal of Physical Chemistry C, 128(3):1433–1442, 2024.

[8] Tiago SA Cassiano, ML Pereira, GM e Silva, Pedro Henrique de Oliveira Neto, and LA Ribeiro. Large polarons in two-dimensional fullerene networks: the crucial role of anisotropy in charge transport. Nanoscale, 16(5):2337–2346, 2024.

[9] Hideki Shirakawa, Edwin J Louis, Alan G MacDiarmid, Chwan K Chiang, and Alan J Heeger. Synthesis of electrically conducting organic polymers: halogen derivatives of polyacetylene,(ch) x. Journal of the Chemical Society, Chemical Communications, (16):578–580, 1977.

[10] Hideki Shirakawa. The discovery of polyacetylene film: the dawning of an era of conducting polymers (nobel lecture). Angewandte Chemie International Edition, 40(14):2574–2580, 2001.

[11] Jun Gao Fumitomo Hide and Hailiang Wang. Efficient photodetectors and photovoltaic cells from composites of fullerenes and conjugated polymers: Photoinduced electron transfer. Synthetic metals, 84(1-3):979–980, 1997.

[12] Mohamad Saleh AlSalhi, Javed Alam, Lawrence Arockiasamy Dass, and Mohan Raja.

Recent advances in conjugated polymers for light emitting devices. International Journal of Molecular Sciences, 12(3):2036–2054, 2011.

[13] Markus Gross, David C Müller, Heinz-Georg Nothofer, Ulrich Scherf, Dieter Neher, Christoph Bräuchle, and Klaus Meerholz. Improving the performance of doped π-conjugated polymers for use in organic light-emitting diodes. Nature, 405(6787):661–665, 2000.

[14] Samik Jhulki, Jeehong Kim, In-Chul Hwang, Golam Haider, Jiyong Park, Ji Young Park, Yeonsang Lee, Wooseup Hwang, Ajaz Ahmed Dar, Barun Dhara, et al. Solution-processable, crystalline π-conjugated two-dimensional polymers with high charge carrier mobility. Chem, 6(8):2035–2045, 2020.

[15] Zijie Qiu, Brenton AG Hammer, and Klaus Müllen. Conjugated polymers–problems and promises. Progress in Polymer Science, 100:101179, 2020.

[16] Richard E Smalley. Discovering the fullerenes (nobel lecture). Angewandte Chemie International Edition in English, 36(15):1594–1601, 1997.

[17] Thomas W Ebbesen. Carbon nanotubes. Annual review of materials science, 24(1):235–264, 1994.

[18] Kostya S Novoselov, Andre K Geim, Sergei V Morozov, Dingde Jiang, Yanshui Zhang, Sergey V Dubonos, Irina V Grigorieva, and Alexandr A Firsov. Electric field effect in atomically thin carbon films. science, 306(5696):666–669, 2004.

[19] Cheng Zhang, Jinguo Chen, Jindong Gao, Guanglong Tan, Shaobo Bai, Kangwei Weng, Hua Min Chen, Xiaohong Ding, Huanyu Cheng, Yanhui Yang, et al. Laser processing of crumpled porous graphene/mxene nanocomposites for a standalone gas sensing system. Nano letters, 23(8):3435–3443, 2023.

[20] Byungjin Cho, Jongwon Yoon, Myung Gwan Hahm, Dong-Ho Kim, Ah Ra Kim, Yung Ho Kahng, Sang-Won Park, Young-Joo Lee, Sung-Gyu Park, Jung-Dae Kwon, et al. Graphene-based gas sensor: metal decoration effect and application to a flexible device. Journal of Materials Chemistry C, 2(27):5280–5285, 2014.

[21] F Giannazzo, R Dagher, E Schilirò, SE Panasci, G Greco, G Nicotra, F Roccaforte, S Agnello, J Brault, Y Cordier, et al. Nanoscale structural and electrical properties of graphene grown on algan by catalyst-free chemical vapor deposition. Nanotechnology, 32(1):015705, 2020.

[22] YZN Htwe, MK Abdullah, and M Mariatti. Water-based graphene/agnps hybrid conductive inks for flexible electronic applications. Journal of Materials Research and Technology, 16:59–73, 2022.

[23] Yuxuan Lin, Xinming Li, Dan Xie, Tingting Feng, Yu Chen, Rui Song, He Tian, Tianling Ren, Minlin Zhong, Kunlin Wang, et al. Graphene/semiconductor heterojunction solar cells with modulated antireflection and graphene work function. Energy & Environmental Science, 6(1):108–115, 2013.

[24] Akanksha R Urade, Indranil Lahiri, and KS Suresh. Graphene properties, synthesis and applications: a review. Jom, 75(3):614–630, 2023.

[25] Jinbo Pang, Songang Peng, Chongyang Hou, Hongbin Zhao, Yingju Fan, Chen Ye, Nuo Zhang, Ting Wang, Yu Cao, Weijia Zhou, et al. Applications of graphene in five senses, nervous system, and artificial muscles. ACS sensors, 8(2):482–514, 2023.

[26] Yi He, Chen Yi, Xiliu Zhang, Wei Zhao, and Dongsheng Yu. Magnetic graphene oxide: synthesis approaches, physicochemical characteristics, and biomedical applications. TrAC Trends in Analytical Chemistry, 136:116191, 2021.

[27] Guo Wang. Effect of edge-hydrogen passivation and saturation on the carrier mobility of armchair graphene nanoribbons. Chemical Physics Letters, 533:74–77, 2012.

[28] Kirill I Bolotin, K J Sikes, Zd Jiang, M Klima, G Fudenberg, J ea Hone, Ph Kim, and HL Stormer. Ultrahigh electron mobility in suspended graphene. Solid state communications, 146(9-10):351–355, 2008.

[29] AH Castro Neto, Francisco Guinea, Nuno MR Peres, Kostya S Novoselov, and Andre K Geim. The electronic properties of graphene. Reviews of modern physics, 81(1):109, 2009.

[30] Hoik Lee, Keewook Paeng, and Ick Soo Kim. A review of doping modulation in graphene. Synthetic Metals, 244:36–47, 2018.

[31] Stefano Agnoli and Marco Favaro. Doping graphene with boron: a review of synthe-

sis methods, physicochemical characterization, and emerging applications. Journal of Materials Chemistry A, 4(14):5002–5025, 2016.

[32] Rebti Bhushan, Prashant Kumar, and AK Thakur. Catalyst-free solvothermal synthesis of ultrapure elemental n-and b-doped graphene for energy storage application. Solid State Ionics, 353:115371, 2020.

[33] Li Yang, Cheol-Hwan Park, Young-Woo Son, Marvin L Cohen, and Steven G Louie. Quasiparticle energies and band gaps in graphene nanoribbons. Physical Review Letters, 99(18):186801, 2007.

[34] Asha P Johnson, Chinnu Sabu, N Kumara Swamy, Annstephy Anto, HV Gangadharappa, and K Pramod. Graphene nanoribbon: An emerging and efficient flat molecular platform for advanced biosensing. Biosensors and Bioelectronics, page 113245, 2021.

[35] Yu Zhu, Amanda L Higginbotham, and James M Tour. Covalent functionalization of surfactant-wrapped graphene nanoribbons. Chemistry of Materials, 21(21):5284–5291, 2009.

[36] Hao Bu, Yunfei Chen, Min Zou, Hong Yi, Kedong Bi, and Zhonghua Ni. Atomistic simulations of mechanical properties of graphene nanoribbons. Physics Letters A, 373(37):3359–3362, 2009.

[37] Sanna Lone, Anil Bhardwaj, Amit Kant Pandit, Sumeet Gupta, and Shubham Mahajan. A review of graphene nanoribbon field-effect transistor structures. Journal of Electronic Materials, 50(6):3169–3186, 2021.

[38] Akimitsu Narita, Xinliang Feng, Yenny Hernandez, Søren A Jensen, Mischa Bonn, Huafeng Yang, Ivan A Verzhbitskiy, Cinzia Casiraghi, Michael Ryan Hansen, Amelie HR Koch, et al. Synthesis of structurally well-defined and liquid-phase-processable graphene nanoribbons. Nature chemistry, 6(2):126, 2014.

[39] Ming-Wei Lin, Cheng Ling, Luis A Agapito, Nicholas Kioussis, Yiyang Zhang, Mark Ming-Cheng Cheng, Wei L Wang, Efthimios Kaxiras, and Zhixian Zhou. Approaching the intrinsic band gap in suspended high-mobility graphene nanoribbons. Physical Review B, 84(12):125411, 2011.

[40] Yunbin Hu, Peng Xie, Marzio De Corato, Alice Ruini, Shen Zhao, Felix Meggendorfer, Lasse Arnt Straasø, Loic Rondin, Patrick Simon, Juan Li, et al. Bandgap engineering of graphene nanoribbons by control over structural distortion. Journal of the American Chemical Society, 140(25):7803–7809, 2018.

[41] Luiz Antonio Ribeiro Jr, Wiliam Ferreira da Cunha, Antonio Luciano de Almeida Fonseca, Geraldo Magela e Silva, and Sven Stafstrom. Transport of polarons in graphene nanoribbons. The journal of physical chemistry letters, 6(3):510–514, 2015.

[42] Tiago Sousa Araújo Cassiano, Fábio Ferreira Monteiro, Leonardo Evaristo de Sousa, Geraldo Magela e Silva, and Pedro Henrique de Oliveira Neto. Smooth gap tuning strategy for cove-type graphene nanoribbons. RSC Advances, 10(45):26937–26943, 2020.

[43] Young-Woo Son, Marvin L Cohen, and Steven G Louie. Energy gaps in graphene nanoribbons. Physical review letters, 97(21):216803, 2006.

[44] Marcelo Lopes Pereira Júnior, Pedro Henrique de Oliveira Neto, Demétrio Antônio da Silva Filho, Leonardo Evaristo de Sousa, Geraldo Magela e Silva, and Luiz Antônio Ribeiro Júnior. Charge localization and hopping in a topologically engineered graphene nanoribbon. Scientific Reports, 11(1):1–9, 2021.

[45] Yea-Lee Lee, Fangzhou Zhao, Ting Cao, Jisoon Ihm, and Steven G Louie. Topological phases in cove-edged and chevron graphene nanoribbons: Geometric structures, z 2 invariants, and junction states. Nano letters, 18(11):7247–7253, 2018.

[46] WenXing Zhang. Voltage-driven spintronic logic gates in graphene nanoribbons. Scientific reports, 4(1):1–5, 2014.

[47] Er-jun Kan, Zhenyu Li, Jinlong Yang, and JG Hou. Half-metallicity in edge-modified zigzag graphene nanoribbons. Journal of the American Chemical Society, 130(13):4224–4225, 2008.

[48] Preetika Sharma and Gaurav Sapra. Integrating silicon in armchair graphene nanoribbon for solar cell applications. In IOP Conference Series: Materials Science and Engineering, volume 1225, page 012028. IOP Publishing, 2022.

[49] Fouad N Ajeel, Mohammed H Mohammed, and Alaa M Khudhair. Energy bandgap engineering of graphene nanoribbon by doping phosphorous impurities to create nano-heterostructures: A dft study. Physica E: Low-dimensional Systems and Nanostructures, 105:105–115, 2019.

[50] Lingxiu Chen, Li He, Hui Shan Wang, Haomin Wang, Shujie Tang, Chunxiao Cong,

Hong Xie, Lei Li, Hui Xia, Tianxin Li, et al. Oriented graphene nanoribbons embedded in hexagonal boron nitride trenches. Nature communications, 8(1):1–6, 2017.

[51] Vivek Saraswat, Robert M Jacobberger, and Michael S Arnold. Materials science challenges to graphene nanoribbon electronics. ACS nano, 15(3):3674–3708, 2021.

[52] Chuan Liu, Bing Yao, Taige Dong, Haiguang Ma, Shaobo Zhang, Junzhuan Wang, Jun Xu, Yi Shi, Kunji Chen, Libo Gao, et al. Highly stretchable graphene nanoribbon springs by programmable nanowire lithography. npj 2D Materials and Applications, 3(1):1–9, 2019.

[53] Daniel J Rizzo, Gregory Veber, Ting Cao, Christopher Bronner, Ting Chen, Fangzhou Zhao, Henry Rodriguez, Steven G Louie, Michael F Crommie, and Felix R Fischer. Topological band engineering of graphene nanoribbons. Nature, 560(7717):204, 2018.

[54] Stephan Blankenburg, Jinming Cai, Pascal Ruffieux, Rached Jaafar, Daniele Passerone, Xinliang Feng, Klaus Mullen, Roman Fasel, and Carlo A Pignedoli. Intraribbon heterojunction formation in ultranarrow graphene nanoribbons. Acs Nano, 6(3):2020–2025, 2012.

[55] Yen-Chia Chen, Ting Cao, Chen Chen, Zahra Pedramrazi, Danny Haberer, Dimas G De Oteyza, Felix R Fischer, Steven G Louie, and Michael F Crommie. Molecular bandgap engineering of bottom-up synthesized graphene nanoribbon heterojunctions. Nature nanotechnology, 10(2):156–160, 2015.

[56] Amir Taqieddin and NR Aluru. Electronic structure and transport in graphene nanoribbon

heterojunctions under uniaxial strain: Implications for flexible electronics. ACS Applied Nano Materials, 4(6):5816–5824, 2021.

[57] Christoph Dobner, Gang Li, Mamun Sarker, Alexander Sinitskii, and Axel Enders. Diffusion-controlled on-surface synthesis of graphene nanoribbon heterojunctions. RSC advances, 12(11):6615–6618, 2022.

[58] Michele Pizzochero, Nikita V Tepliakov, Johannes Lischner, Arash A Mostofi, and Efthimios Kaxiras. One-dimensional magnetic conduction channels across zigzag graphene nanoribbon/hexagonal boron nitride heterojunctions. Nano Letters, 2024.

[59] Paulo S Costa, Jacob D Teeter, Axel Enders, and Alexander Sinitskii. Chevron-based graphene nanoribbon heterojunctions: Localized effects of lateral extension and structural defects on electronic properties. Carbon, 134:310–315, 2018.

[60] Jinming Cai, Carlo A Pignedoli, Leopold Talirz, Pascal Ruffieux, Hajo Söde, Liangbo Liang, Vincent Meunier, Reinhard Berger, Rongjin Li, Xinliang Feng, et al. Graphene nanoribbon heterojunctions. Nature nanotechnology, 9(11):896–900, 2014.

[61] Matthew Yankowitz, Shaowen Chen, Hryhoriy Polshyn, Yuxuan Zhang, K Watanabe, T Taniguchi, David Graf, Andrea F Young, and Cory R Dean. Tuning superconductivity in twisted bilayer graphene. Science, 363(6431):1059–1064, 2019.

[62] Qing Zhang, Guangwei Hu, Weiliang Ma, Peining Li, Alex Krasnok, Rainer Hillenbrand, Andrea Alù, and Cheng-Wei Qiu. Interface nano-optics with van der waals polaritons. Nature, 597(7875):187–195, 2021.

[63] Viliam Vaňo, Mohammad Amini, Somesh C Ganguli, Guangze Chen, Jose L Lado, Shawulienu Kezilebieke, and Peter Liljeroth. Artificial heavy fermions in a van der waals heterostructure. Nature, 599(7886):582–586, 2021.

[64] Edward McCann and Mikito Koshino. The electronic properties of bilayer graphene. Reports on Progress in physics, 76(5):056503, 2013.

[65] Eduardo V Castro, KS Novoselov, SV Morozov, NMR Peres, JMB Lopes Dos Santos, Johan Nilsson, F Guinea, AK Geim, and AH Castro Neto. Biased bilayer graphene: semiconductor with a gap tunable by the electric field effect. Physical review letters, 99(21):216802, 2007.

[66] Wenjing Zhang, Qixing Wang, Yu Chen, Zhuo Wang, and Andrew TS Wee. Van der waals stacked 2d layered materials for optoelectronics. 2D Materials, 3(2):022001, 2016.

[67] Hanjian Lai and Feng He. Crystal engineering in organic photovoltaic acceptors: a 3d network approach. Advanced Energy Materials, 10(47):2002678, 2020.

[68] Lingxiang Hou, Xueping Cui, Bo Guan, Shaozhi Wang, Ruian Li, Yunqi Liu, Daoben Zhu, and Jian Zheng. Synthesis of a monolayer fullerene network. Nature, 606(7914):507–510, 2022.

[69] Veaceslav Coropceanu, Jérôme Cornil, Demetrio A da Silva Filho, Yoann Olivier, Robert Silbey, and Jean-Luc Brédas. Charge transport in organic semiconductors. Chemical reviews, 107(4):926–952, 2007.

[70] Samuele Giannini, Orestis George Ziogos, Antoine Carof, Matthew Ellis, and Jochen Blumberger. Flickering polarons extending over ten nanometres mediate charge transport in high-mobility organic crystals. Advanced Theory and Simulations, 3(9):2000093, 2020.

[71] ME Gershenson, V Podzorov, and AF Morpurgo. Colloquium: Electronic transport in single-crystal organic transistors. Reviews of modern physics, 78(3):973, 2006.

[72] Colin Reese and Zhenan Bao. Organic single-crystal field-effect transistors. Materials Today, 10(3):20–27, 2007.

[73] Tao He, Matthias Stolte, Christian Burschka, Nis Hauke Hansen, Thomas Musiol, Daniel Kälblein, Jens Pflaum, Xutang Tao, Jochen Brill, and Frank Würthner. Single-crystal field-effect transistors of new cl2-ndi polymorph processed by sublimation in air. Nature communications, 6(1):5954, 2015.

[74] Pance Naumov, Stanislav Chizhik, Manas K Panda, Naba K Nath, and Elena Boldyreva. Mechanically responsive molecular crystals. Chemical reviews, 115(22):12440–12490, 2015.

[75] Hao Liu, Zhengyi Bian, Qinyu Cheng, Linfeng Lan, Yue Wang, and Hongyu Zhang. Controllably realizing elastic/plastic bending based on a room-temperature phosphorescent waveguiding organic crystal. Chemical science, 10(1):227–232, 2019.

[76] Luca Catalano, Durga Prasad Karothu, Stefan Schramm, Ejaz Ahmed, Rachid Rezgui, Timothy J Barber, Antonino Famulari, and Panče Naumov. Dual-mode light transduction

through a plastically bendable organic crystal as an optical waveguide. Angewandte Chemie International Edition, 57(52):17254–17258, 2018.

[77] Jean Luc Bredas and G Bryan Street. Polarons, bipolarons, and solitons in conducting polymers. Accounts of Chemical Research, 18(10):309–315, 1985.

[78] Aaron Bostwick, Taisuke Ohta, Thomas Seyller, Karsten Horn, and Eli Rotenberg. Quasiparticle dynamics in graphene. Nature physics, 3(1):36–40, 2007.

[79] Li Yang, Marvin L Cohen, and Steven G Louie. Excitonic effects in the optical spectra of graphene nanoribbons. Nano letters, 7(10):3112–3115, 2007.

[80] Wiliam Ferreira da Cunha, Pedro Henrique de Oliveira Neto, Luiz Antonio Ribeiro Junior, and Geraldo Magela e Silva. Quasiparticle description of transition metal dichalcogenide nanoribbons. Physical Review B, 99(3):035405, 2019.

[81] Marcelo Lopes Pereira Júnior, Bernhard Georg Enders Neto, William Ferreira Giozza, Rafael Timóteo Sousa Júnior, Geraldo Magela e Silva, and Luiz Antônio Ribeiro Júnior. Transport of quasiparticles in coronene-based graphene nanoribbons. Journal of Materials Chemistry C, 8(35):12100–12107, 2020.

[82] Wiliam F da Cunha, Paulo H Acioli, Pedro H de Oliveira Neto, Ricardo Gargano, and Geraldo M e Silva. Polaron properties in armchair graphene nanoribbons. The Journal of Physical Chemistry A, 120(27):4893–4900, 2016.

[83] Pedro Henrique de Oliveira Neto and Troy Van Voorhis. Dynamics of charge quasiparticles generation in armchair graphene nanoribbons. Carbon, 132:352–358, 2018.

[84] Marcelo Macedo Fischer, Luiz Antonio Ribeiro Junior, Wiliam Ferreira da Cunha, Leonardo Evaristo de Sousa, Geraldo Magela e Silva, and Pedro Henrique de Oliveira Neto. Ultrafast direct generation of quasiparticles in graphene nanoribbons. Carbon, 158:553–558, 2020.

[85] Junichi Yamaguchi, Hironobu Hayashi, Hideyuki Jippo, Akitoshi Shiotari, Manabu Ohtomo, Mitsuhiro Sakakura, Nao Hieda, Naoki Aratani, Mari Ohfuchi, Yoshiaki Sugimoto, et al. Small bandgap in atomically precise 17-atom-wide armchair-edged graphene nanoribbons. Communications Materials, 1(1):1–9, 2020.

[86] Luiz Antonio Ribeiro Junior and Sven Stafström. Polaron stability in molecular semiconductors: Theoretical insight into the impact of the temperature, electric field and the system dimensionality. Physical Chemistry Chemical Physics, 17(14):8973–8982, 2015.

[87] Marcelo Macedo Fischer, Leonardo Evaristo de Sousa, Leonardo Luiz e Castro, Luiz Antonio Ribeiro, Rafael Timóteo de Sousa, Geraldo Magela e Silva, and Pedro Henrique de Oliveira Neto. Effective mass of quasiparticles in armchair graphene nanoribbons. Scientific reports, 9(1):1–8, 2019.

[88] Zongping Chen, Hai I Wang, Joan Teyssandier, Kunal S Mali, Tim Dumslaff, Ivan Ivanov, Wen Zhang, Pascal Ruffieux, Roman Fasel, Hans Joachim Rader, et al. Chemical vapor deposition synthesis and terahertz photoconductivity of low-band-gap n= 9 armchair graphene nanoribbons. Journal of the American Chemical Society, 139(10):3635–3638, 2017.

[89] Elham Mozafari and Sven Stafström. Polaron dynamics in a two-dimensional holstein-peierls system. The Journal of chemical physics, 138(18):184104, 2013.

[90] Ying-fei Chang, Zhong-yuan Lu, Li-jia An, and Jing-ping Zhang. From molecules to materials: molecular and crystal engineering design of organic optoelectronic functional materials for high carrier mobility. The Journal of Physical Chemistry C, 116(1):1195–1199, 2012.

[91] Ivan Ivanov, Yunbin Hu, Silvio Osella, Uliana Beser, Hai I Wang, David Beljonne, Akimitsu Narita, Klaus Mullen, Dmitry Turchinovich, and Mischa Bonn. Role of edge engineering in photoconductivity of graphene nanoribbons. Journal of the American Chemical Society, 139(23):7982–7988, 2017.

[92] Samantha Bruzzone and Gianluca Fiori. Ab-initio simulations of deformation potentials and electron mobility in chemically modified graphene and two-dimensional hexagonal boron-nitride. Applied Physics Letters, 99(22):222108, 2011.

[93] N. Aziziah Amin, Zaharah Johari, Mohammad Taghi Ahmadi, and Razali Ismail. Low-field mobility model on parabolic band energy of graphene nanoribbon. Modern Physics Letters B, 25(4):281–290, 2011.

[94] Simone Pisana, Michele Lazzeri, Cinzia Casiraghi, Kostya S Novoselov, Andre K Geim, Andrea C Ferrari, and Francesco Mauri. Breakdown of the adiabatic born–oppenheimer approximation in graphene. Nature materials, 6(3):198–201, 2007.

[95] Steven H Simon. The Oxford solid state basics. OUP Oxford, 2013.

[96] John M Ziman. Principles of the Theory of Solids. Cambridge university press, 1972.

[97] Alan J Heeger, S Kivelson, JR Schrieffer, and W-P Su. Solitons in conducting polymers. Reviews of Modern Physics, 60(3):781, 1988.

[98] W_P Su, JR Schrieffer, and Ao J Heeger. Solitons in polyacetylene. Physical review letters, 42(25):1698, 1979.

[99] Wiliam Ferreira da Cunha, Pedro Henrique de Oliveira Neto, Akira Terai, and Geraldo Magela e Silva. Dynamics of charge carriers on hexagonal nanoribbons with vacancy defects. Physical Review B, 94(1):014301, 2016.

[100] Gesiel Gomes Silva, Wiliam Ferreira da Cunha, Rafael Timóteo de Sousa Junior, Antonio Luciano Almeida Fonseca, Luiz Antônio Ribeiro Júnior, and Geraldo Magela e Silva. Influence of quasi-particle density over polaron mobility in armchair graphene nanoribbons. Physical Chemistry Chemical Physics, 20(24):16712–16718, 2018.

[101] Wiliam Ferreira da Cunha, Luiz Antonio Ribeiro Junior, Antonio Luciano de Almeida Fonseca, Ricardo Gargano, and Geraldo Magela e Silva. Impurity effects on polaron dynamics in graphene nanoribbons. Carbon, 91:171–177, 2015.

[102] Tiago de Sousa Araújo Cassiano. Structural and electronic properties of the cove-type graphene nanoribbons. 2021.

[103] Yoshiyuki Ono and Akira Terai. Motion of charged soliton in polyacetylene due to electric field. Journal of the Physical Society of Japan, 59(8):2893–2904, 1990.

[104] Wiliam Ferreira da Cunha, Pedro Henrique de Oliveira Neto, Akira Terai, and Geraldo Magela e Silva. Dynamics of charge carriers on hexagonal nanoribbons with vacancy defects. Physical Review B, 94(1):014301, 2016.

[105] Maurício Bellissimo Falleiros. Espalhamento de pólarons em compostos de poliparafenileno. PhD thesis, Universidade de Brasília, 2019.

[106] John Robert Taylor. Classical mechanics. Number 531 TAY. bookman, 2005.

[107] P. H. De Oliveira Neto, J. F. Teixeira, W. F. Da Cunha, R. Gargano, and G. M. E Silva. Electron-lattice coupling in armchair graphene nanoribbons. Journal of Physical Chemistry Letters, 3(20):3039–3042, 2012.

[108] PH de Oliveira Neto, JF Teixeira, WF Da Cunha, R Gargano, and GM e Silva. Electron–lattice coupling in armchair graphene nanoribbons. The journal of physical chemistry letters, 3(20):3039–3042, 2012.

[109] Elham Mozafari. A Theoretical Study of Charge Transport in Molecular Crystals. Linkopings Universitet (Sweden), 2012.

[110] Elham Mozafari and Sven Stafström. Polaron stability in molecular crystals. Physics Letters A, 376(22):1807–1811, 2012.

[111] Luiz Antonio Ribeiro Junior and Sven Stafström. Polaron dynamics in anisotropic holstein–peierls systems. Physical Chemistry Chemical Physics, 19(5):4078–4084, 2017.

[112] Martin Riedmiller and Heinrich Braun. A direct adaptive method for faster backpropaga-

tion learning: The rprop algorithm. In IEEE international conference on neural networks, pages 586–591. IEEE, 1993.

[113] Shuai Zhao, Xibei Zhang, Yong Ni, Qing Peng, and Yujie Wei. Anisotropic mechanical response of a 2d covalently bound fullerene lattice. Carbon, 202:118–124, 2023.

[114] Linfeng Yu, Jinyuan Xu, Bo Peng, Guangzhao Qin, and Gang Su. Anisotropic optical, mechanical, and thermoelectric properties of two-dimensional fullerene networks. The Journal of Physical Chemistry Letters, 13:11622–11629, 2022.

APPENDIX A

PUBLISHED PAPER (CONJUGATED POLYMERS)

A.1 PAPER A1

Quasiparticle dynamics by effective π-field distortion

Tiago de Sousa Araújo Cassiano

Pedro Henrique de Oliveira Neto

Geraldo Magela e Silva

Sci Rep 12, 7967 (2022)

10.1038/s41598-022-11832-2

www.nature.com/scientificreports

scientific reports

Check for updates

OPEN

Quasiparticle dynamics by effective π-field distortion

Tiago de Sousa Araújo Cassiano, Pedro Henrique de Oliveira Neto & Geraldo Magela e Silva✉

Modeling dynamical processes of quasiparticles in low dimensional π-conjugated systems is challenging due to electron-phonon coupling. We show that this interaction leads to linear potential energy terms in the lattice Lagrangian similar to a local "gravitational" field. The presence of quasiparticles deforms this field in a way analogous to a low-dimension solution of general relativity. Our calculations with analytical expressions for effective π-fields yield the correct band structure and deliver proper time evolution of the quasiparticle's properties. Furthermore, we report a sharp reduction in the dynamics computational time up to two orders of magnitude, a result that has major simulation implications.

π-conjugated systems have been used as primary materials in optoelectronics, being prominent candidates to substitute inorganic devices. Showing several promising properties such as low cost, flexibility, and versatility of synthesis, these materials are already present in photodetectors[35], organic solar cells[15], light-emitting diodes[1,12], and field-effect transistors[16], among others[34]. Understanding the fundamental properties of organic π-conjugated compounds constitutes a complex and central problem that can lead to significant technological applications.

Most of the optical and electronic properties of those systems originate from the conjugated bonding based on sp^2-hybridized carbons. The combination of strong electron-phonon coupling, intrinsic to π-electrons, and low dimension confinement effects leads to transport mechanisms mediated by quasiparticles. The dynamics of these carriers determine the spectroscopic, optical, energy, and charge transport properties in π-conjugated compounds[2]. While excitons are responsible for energy transport, polarons are the main charge carriers. Polarons are lattice distortions that polarize the nearby environment. They are collective excitations with spin 1/2, charge $\pm e$, and effective mass that depends on the material[4,5]. The lattice distortion pattern and the intragap states of the electronic band characterize them. Besides the polaron, other charge carriers may be present in π-conjugated systems such as bipolarons and solitons, although been less prevalent.

The theoretical description of charge dynamics of π-conjugated systems is convoluted. Since electron-phonon coupling is present, the electronic and nuclei equations can not be separated solved. They must be solved simultaneously, in a scenario where the Born Oppenheimer approximation does not hold.

Su, Schrieffer, and Heeger were pioneers in modeling the quasiparticle transport by a semi-classical approach for conjugated systems[14,28,30,31]. Their model, known as the SSH model, was initially proposed to describe the conduction in polyacetylene. In the context of a tight-binding method, the core of this model is a first-order approximation of the hopping integral considering lattice distortion. This model was used to describe the morphological and electronic aspects of conjugated polymers carrying quasiparticles. Eventually, further refinements enabled the study of dynamic states[11,13,24,29,33]. The electronic states evolve according to the time-dependent Schrödinger equation, while the lattice does it through Lagrangian mechanics. However, the electron-phonon interaction couples the equations, requiring them to be solved simultaneously. Most of the simulation's computational cost comes from this constraint.

Recently, the SSH model was extended to 2D systems, increasing even further its applicability and impact. Nowadays, this development is the basis of theoretical research in graphene nanoribbons[3,8,26,27]. In addition, the extension for aggregates, known as the Holstein-Peierls model, became a central tool to investigate intermolecular charge dynamics[9,18,21,23].

By examining the expected value of the Lagrangian we show that, to the space-time distortion done by mass in general relativity, the polaron is associated with a low-dimensional distortion of the effective π-force-field. The field of the π-electrons works as an effective "gravitational" field with the potential energy proportional to the displacement of the carbon atoms. We propose an alternative model to simulate the dynamics of conjugated systems by including this effective potential analytically to describe the π-electrons influence on the lattice. This change removes the need for higher-order explicit time integration methods. The model's physical accuracy is examined. We simulated polaron dynamics on cis-polyacetylene with both the conventional model as a reference and our own. Detailed analysis of the polaron drifting process, electronic band structure, energy dynamics, and

Institute of Pysics, University of Braília, Brasília, Brazil. ✉email: magela@unb.br

other phenomena reveals the equivalence between the methodologies. Moreover, the method is also notably cost-efficient, producing time reductions of two orders of magnitude, indicating its use for larger systems in which the conventional procedure becomes impracticable.

Methods

We present the SSH model in detail to point out precisely what can be done in a different way. Cis-polyacetylene is considered to keep the notation as concise as possible. Besides, its structure is a common backbone of conducting polymers, and the results are extended easily to 2-D π-systems as graphene nanoribbons. In this formalism, the model Hamiltonian is the sum of electronic (H_{tb}) and lattice (H_{latt}) terms. The first contribution is a tight-binding-like operator given by[30]

$$H_{tb} = -\sum_{n,s}[t_{n+1,n}C^{\dagger}_{n+1,s}C_{n,s} + h.c.]. \tag{1}$$

$C^{\dagger}_{n+1,s}$ is the creation operator of a π-electron at site $n+1$ with spin s. $t_{n+1,n}$ is the hopping integral associated with sites $n+1$ and n. The SSH model restricts the physical description to only low-energy excitations[14]. As a result, the σ-bond fluctuates close to its undisturbed length. The hopping integral is assumed to be dependent on the inter-site distance. Expanding $t_{n+1,n}$ over this length gives

$$t_{n+1,n} = t_n + \alpha(u_{n+1} - u_n), \tag{2}$$

where $t_n \equiv (1 + (-1)^n\delta_0)t_0$, with t_0 the hopping integral in the absence of distortions, δ_0 a Brazovskii-Kirova symmetry breaking term, and u_n the displacement of site n with respect to its equilibrium position. The dependence of the hopping integral with the position is mediated by α, the electron-phonon coupling constant.

In addition, the small fluctuation of the σ-bonds allows to adopt the harmonic approximation and treat the lattice as a sum of coupled harmonic oscillators,

$$H_{latt} = \frac{K}{2}\sum_n (u_{n+1} - u_n)^2 + \frac{1}{2M}\sum_n p_n^2. \tag{3}$$

Here, K stands for the elastic constant, M is the site's mass, and P_i is the i-th conjugated momentum.

It is not possible to diagonalize the electronic Hamiltonian directly since it depends on the lattice configuration. Instead, one must simultaneously solve for both the electronic and lattice in a self-consistent manner[10].

One begins by finding stationary solutions for the lattice and π-electrons in an iterative self-consistent way until the convergence criterion is matched. Once the solution converges, it is possible to evolve it in time by including an external electric field. It can be done through a Peierls substitution on the Hamiltonian[25]. Ultimately, this operation only incorporates a time-dependent phase to the hopping integral in Eq. 2, which now reads

$$t_{n+1,n} = e^{-i\gamma A(t)}(t_n + \alpha(u_{n+1} - u_n)). \tag{4}$$

$\gamma \equiv ea/(\hbar c)$, where e stands for the elementary charge, a the lattice parameter, c the speed of light, and $A(t)$ is the vector potential. The electric field depends only on time, $E(t) = -(1/c)\dot{A}(t)$.

Let $|\psi_{k,s}(t)\rangle$ be the electronic solution at a given time t, and $\mathbf{U}(dt) \equiv e^{-iH(t)dt/\hbar}$ the time-evolution operator. Then, the state, after a time interval dt, becomes

$$|\psi_{k,s}(t+dt)\rangle = e^{-iH(t)dt/\hbar}|\psi_{k,s}(t)\rangle. \tag{5}$$

Expanding it over the basis of eigenstates, $\{|\phi_{ls}(t)\rangle\}$, of the electronic Hamiltonian at a given time t leads to,

$$|\psi_{k,s}(t+dt)\rangle = \sum_l e^{-iE_{l,s}dt/\hbar}|\phi_{l,s}(t)\rangle\langle\phi_{l,s}(t)|\psi_{k,s}(t)\rangle, \tag{6}$$

or,

$$\begin{aligned}\psi_{k,s}(n, t+dt) &= \langle n|\psi_{k,s}(t+dt)\rangle \\ &= \sum_{l,m}\phi^*_{l,s}(m,t)\psi_{k,s}(m,t)e^{-iE_{l,s}dt/\hbar}\phi_{l,s}(n,t).\end{aligned} \tag{7}$$

As for the lattice, the expected value of the Lagrangian, $\langle L\rangle$, obeys the Euler-Lagrange equations,

$$\frac{d}{dt}\left(\frac{\partial\langle L\rangle}{\partial\dot{u}_n}\right) = \frac{\partial\langle L\rangle}{\partial u_n}. \tag{8}$$

$\langle L\rangle$ is calculated with a Slater-determinant state composed with all occupied electronic states, $\psi_{k,s}(n,t)$. This equation leads to

$$\begin{aligned}M\ddot{y}_n = &K(y_{n+1} - 2y_n + y_{n-1}) \\ &+\alpha(B_{n+1} - 2B_n + B_{n-1} + \text{c.c.}),\end{aligned} \tag{9}$$

with,

$$B_n \equiv e^{-i\gamma A(t)} \sum_{k,s}{}' \psi^*_{k,s}(n+1,t)\psi_{k,s}(n,t), \tag{10}$$

and, $y_n = u_{n+1} - u_n$. The prime sign means a summation over only occupied states.

The time evolution for the model is determined by equations 7 and 9. When time advances one step, the electronic and lattice configurations change. Because of that, the set $\{\phi_{ls}(t')\}$ is not the same as before. After each time step, the modeling requires the re-diagonalization of the electronic Hamiltonian. Alternatively, one could use high-order explicit time integration methods to evolve the Schrödinger equation. However, these approaches have a significant impact on the algorithm's computational cost, meaning limitations on system size and simulation time.

Equation 9 is the crucible of π-systems description. The B_n terms depend on one-electron wavefunctions that are time demanding to find. But, B_n can be calculated analytically for the stationary dimerized configuration[31]. In this case, the results render Eq. 9 as equivalent to a series of connected spring-masses subjected to an alternating gravitational field, since $B_{n+1} = -B_n$. Which can also be deduced by symmetry arguments. Obviously, this picture changes as time and quasiparticles get into consideration. Nevertheless, the change is well-behaved and predictable. It might be more convenient to think in terms of a π-electrons force field defined by,

$$\Pi_n = -\alpha(B_n + B_n^*). \tag{11}$$

Solving numerically in tandem Eqs. 7 and 9 for several systems[5,6,10], it can be verified that far from quasiparticles and defects, Π_n still behaves as an alternating effective "gravitational" field. It is also found that this effective field distorts in association with polarons according to the pattern $sech^2(x - vt)$. It should be pointed out that the square hyperbolic secant dependence could be foreseen from the analytical solutions of the TLM continuum model[32].

In what follows, we present the simulations of polaron dynamics with the usual approach and the proposed effective field to highlight the equivalence and difference between the two methods.

We set the parameters according to the usual values assigned to conjugated polymers. α = 4.1 eV/Å, t_0 = 2.5 eV, δ_0 = 0.05, K = 21 eV/Å^2 and a = 1.41 Å[19,20]. We simulate a polaron state in the presence of an electric field with a strength of 2.4$\times 10^5$ V/cm. Here, $E(t)$ will continuously grow from zero until t = 50 fs, when it reaches its maximum. Right after, the field drops to 0, remaining off until the end of the simulation. Throughout this work, we simulate the polymer with a system of 120 sites with periodic boundary conditions. The sites' masses equals 13 *a.u.*. Moreover, the initial states of the dynamical simulations are stationary solutions, provided by the self-consistent procedure previously outlined.

Results

Figure 1a represents diagrammatically the π-electron force field, Π_n^d, in the absence of any disturbance by colored arrows. One may see that sites with the same parity possess arrows of equal size, meaning they experience the same potential. Fig. 1(b) shows this field for a polaron. As can be seen, sites far away from the quasiparticle continue to feel a uniform parity-based alternating force field. However, those near it have a local distortion on the force field.

Figure 1c shows actual calculations of Π_n of a system bearing a polaron. The conventional approach yields the red line. The effective method gives the blue one. The quasiparticle's presence breaks the uniformity of the potential leading to a local distortion on the force field. The inset presents Π_n at several time snapshots. The undulation on the left of the red line is due to a breather. It is dependent on how the polaron is accelerated. The breather mode is discernible around the initial position of the polaron.

The effective field is obtained by fitting $\Pi_n = \Pi_n^d + \Pi_n^p$ to a numerically calculated system with a polaron. We found that the polaron force field distortion, Π_n^p, is given by,

$$\Pi_n^p = (-1)^n a_1 \text{sech}^2(a_2 n - vt) \tag{12}$$

in which, $a_1 = -0.52$ and $a_2 = 0.27$. Here we set $v = a_3 A(t)$ with $a_3 = 2.7 * 10^{-3}$. These parameters are robust and characterize polarons in different configurations. In practice, our methodology to estimate Π_n begins by explicitly simulating polaron dynamics via the usual approach. Then, with this reference result, we use Eq. 10 to find B_n, which translates into Π_n through Eq. 11. Having this reference, the π force field is determined through the fitting of the parameters in Eq. 12. The fitted expression represents the general electronic contribution to the lattice dynamics of a conjugated polymer hosting a drifting polaron driven by an external field.

We present in Fig. 2 the results for the system's lattice and electronic pictures for comparison. Fig. 2a and c depict the lattice order parameter and charge density obtained through the conventional formalism. On the other hand, Fig. 2b and d refer to the same variables calculated using the effective potential.

The quasiparticle's trajectory consists of two phases: an initial acceleration and a regime of constant velocity. The first time interval ranges from 0 to 50 fs. The profile of this period is a direct outcome of the active presence of the electric field. The polaron begins to emit phonons in both directions. After 50 fs, the electric field goes off. Right after the phonon scattering event, the quasiparticles drift with a constant velocity until about 280 fs. At this time, the distortions reach the polaron initial position due to the periodic boundary condition. As soon as the quasiparticles return to this region, the polarons of both methodologies suffer from phonon collisions since they encounter breathers excited earlier. As the two structures collide, the signature distortion of the quasiparticle is momentarily muddled[7,17].

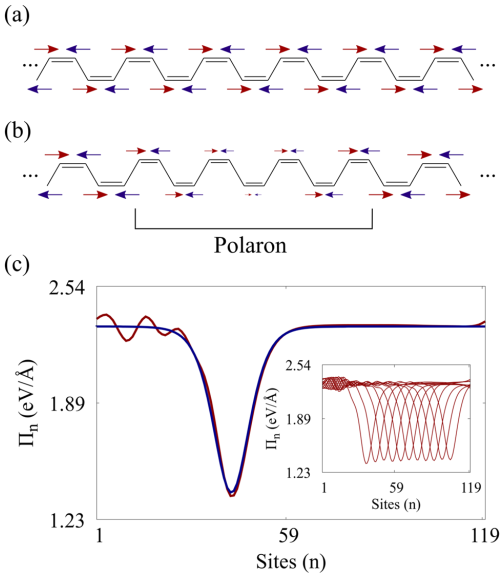

Figure 1. Diagrams (a) and (b) illustrate the behavior of the effective force field in two situations: (a) in the absence of quasiparticles and (b) when the chain hosts a polaron. At each site, there is a colored arrow that symbolizes the orientation of the force field caused by the π-electrons effective potential. The red color indicates odd parity, while the blue even. In (b), there is a distorted set of arrows representing the field distortion associated with the quasiparticle. In (c), the force fields, Π_n, for the conventional and alternative approaches are shown. The lines in red refer to the conventional method, while the blue one is for the effective approach. The inset presents the effective field's time evolution as the polaron drifts.

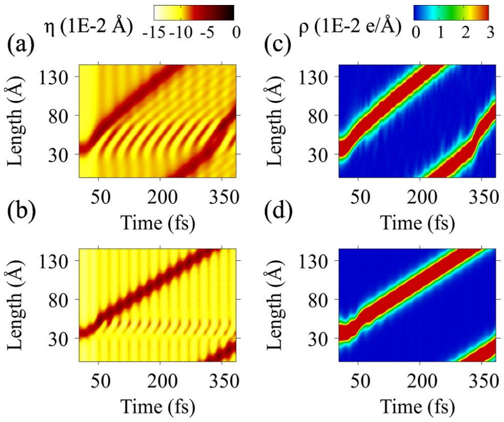

Figure 2. The electronic and lattice dynamics of a polaron state through the traditional and proposed model. Figures (a) and (b) refer to the lattice order parameter, $\eta_n \equiv (y_{n+1} - 2y_n + y_{n-1})/4$, calculated via the conventional and the effective potential approaches, respectively. Light and dark tones indicate the distortion intensity. The localized dark-colored region refers to the polaron. On the other hand, (c) and (d) show the chain's charge density time evolution, $\rho(t) \equiv \sum_{k,s} |\psi_{k,s}(n,t)|^2$, using the traditional procedure and the effective potential, respectively. Here, hot colors represent charge accumulation, while cold ones indicate the absence of charge.

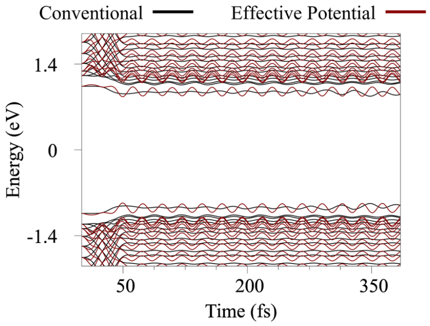

Figure 3. Time dependence of the electronic structure around the band gap. The red and black lines represent electronic states for π-electrons through the effective field and standard approaches, respectively. The states associated with the polaron are visible above the valence band and below the conduction band.

The trajectories delivered by both methodologies represent physically equivalent phenomena. In both cases, the polaron drifts by two distinct regimes, covering similar distances at the same time range. Additionally, the quasiparticles react identically when the acceleration ceases its influence.

Figure 2c and d show the charge density time evolution. As expected, the motion of the charged region is the same as the local deformation that appears in the lattice order parameter. As in Fig. 2a–c, at the same time, the scattered phonons collide with the polaron. These events cause a disturbance in the localized lattice distortion. Because the quasiparticle is a coupled structure of lattice distortion and charge accumulation, a similar effect occurs in (c) and (d). However, since the scattered phonons are less energetic in (d), the disturbance in the charge density profile is smaller.

There is significant accordance regarding the energy dynamics. At the start of the simulations, until about 50 fs, the electronic energy rapidly increases with the applied electric field. Next, the curve ceases to grow and begins to follow an oscillatory trajectory until the end of the simulation. In addition, one may note that polaron moves slightly faster in the traditional simulation. This occurs because, in comparison with the usual approach, the π-field formalism generates a quasiparticle with more definite lattice deformation, increasing the carrier's transport inertia. For this reason, under same electric field conditions, the quasiparticle simulated via the usual approach will cover a slightly greater distance.

The equivalence between the two approaches also becomes apparent when the electronic band structure is analyzed. Figure 3 displays the time dependence of the system's electronic band around the gap with a polaron state. Here, we present the energy states from the two independent methods. The black-colored lines refer to the energy levels obtained with the standard simulation. Alternatively, the red-colored states result from the effective potential dynamics. In both cases, the lines represent electronic states. As can be seen, the methodologies deliver equivalent electronic descriptions of the system.

The overall behavior of the bands can be summarized in two distinct regimes. The first one starts at the beginning of the simulation and goes to about 50 fs. During this period, the energy levels suffer a short but continuous shrinkage towards the center of the gap. That is a direct consequence of the Peierls instability, which is triggered by the external field. The other regime initiates right after that and goes until the end of the simulation. The energy states display small fluctuations around an average value. This profile is a result of lattice disturbances caused by the polaron's continuous drift and the motion of scattered phonons[22].

Besides the similarities, the band from the effective potential approach has more intense fluctuations. It is a consequence of the successive collisions with the normal oscillation mode visible in Fig. 2b. The energy bandgap of the conventional approach is found to be 1.81 ∓ 0.06 eV, while the effective field method gives 1.83 ∓ 0.1 eV.

The computation cost of the proposed model is a central point. As discussed in the methods, the approach eliminates the need to diagonalize the electronic Hamiltonian at each time step. Clearly, such optimization reduces the computational cost. All simulations were performed using the same machine. The results present a great drop in the execution time, averaging two orders of magnitude. Although such an estimate depends on the machine used, we expect no changes in the conclusion: the effective potential is two orders of magnitude faster than conventional simulations.

Conclusion

In conclusion, we introduced an alternative model to simulate π-conjugated systems. The approach describes the electronic contribution to lattice dynamics in terms of effective π-fields. We showed that in the absence of lattice disturbances the effective force field is uniform, behaving similarly to an alternating constant gravitational field. By extending the study to excited states, we showed that the presence of quasiparticles distorts the field locally. We ran extensive tests comparing it with the usual formalism to estimate the model's reliability. The comparison between the modelings took place with dynamical simulations of the drifting of polaron under the influence of external electric fields. The two methodologies agree on the polaron's trajectory, the electronic band structure, and the phonon scattering. In that sense, the adoption of this new strategy causes no loss in the description's physical accuracy. In addition, we also tested the model's limits by enforcing different electric field regimes. Even under such conditions, the model coincides tightly with reference simulations. We also report a sharp time drop of two orders of magnitude compared with the standard approach. That is due to freeing the calculations from the constraint of diagonalization at each time in the evolution process. Our approach is an alternative to simulate much larger π-systems, where π-electron interactions are considered, and dynamics of multiple polarons become possible.

Data availability

The datasets used and/or analysed during the current study available from the corresponding author on reasonable request.

Received: 25 February 2022; Accepted: 18 April 2022

References

1. AlSalhi, M. S., Alam, J., Dass, L. A. & Raja, M. Recent advances in conjugated polymers for light emitting devices. *Int. J. Mol. Sci.* **12**(3), 2036–2054 (2011).
2. Bredas, J. L. & Street, G. B. Polarons, bipolarons, and solitons in conducting polymers. *Acc. Chem. Res.* **18**(10), 309–315 (1985).
3. Cassiano, T. *et al.* Smooth gap tuning strategy for cove-type graphene nanoribbons. *RSC Adv.* **10**(45), 26937–26943 (2020).
4. da Cunha, W. F., Acioli, P. H., de Oliveira Neto, P. H., Gargano, R. & e Silva, G. .M. . Polaron properties in armchair graphene nanoribbons. *J. Phys. Chem. A* **120**(27), 4893–4900 (2016).
5. da Cunha, W. F., de Oliveira Neto, P. H., Junior, L. A. R. & e Silva, G. . M. . Quasiparticle description of transition metal dichalcogenide nanoribbons. *Phys. Rev. B* **99**(3), 035405 (2019).
6. da Cunha, W. F., de Oliveira Neto, P. H., Terai, A. & e Silva, G. . M. . Dynamics of charge carriers on hexagonal nanoribbons with vacancy defects. *Phys. Rev. B* **94**(1), 014301 (2016).
7. da Silva Pinheiro, C. & e Silva, G. . M. . Use of polarons and bipolarons in logical switches based on conjugated polymers. *Phys. Rev. B* **65**, 094304 (2002).
8. de Oliveira Neto, P., Teixeira, J., Da Cunha, W., Gargano, R. & e Silva, G. Electron-lattice coupling in armchair graphene nanoribbons. *J. Phys. Chem. Lett.* **3**(20), 3039–3042 (2012).
9. Duan, H.-G., Nalbach, P., Miller, R. D. & Thorwart, M. Ultrafast energy transfer in excitonically coupled molecules induced by a nonlocal peierls phonon. *J. Phys. Chem. Lett.* **10**(6), 1206–1211 (2019).
10. e Silva, G. M. Electric-field effects on the competition between polarons and bipolarons in conjugated polymers. *Phys. Rev. B* **61**(16), 10777 (2000).
11. e Silva, G. M. & Terai, A. Dynamics of solitons in polyacetylene with interchain coupling. *Phys. Rev. B* **47**(19), 12568 (1993).
12. Gross, M. *et al.* Improving the performance of doped π-conjugated polymers for use in organic light-emitting diodes. *Nature* **405**(6787), 661–665 (2000).
13. Guinea, F. Dynamics of polyacetylene chains. *Phys. Rev. B* **30**(4), 1884 (1984).
14. Heeger, A. J., Kivelson, S., Schrieffer, J. & Su, W.-P. Solitons in conducting polymers. *Rev. Mod. Phys.* **60**(3), 781 (1988).
15. Hide, J. G. F. & Wang, H. Efficient photodetectors and photovoltaic cells from composites of fullerenes and conjugated polymers: Photoinduced electron transfer. *Synth. Met.* **84**(1–3), 979–980 (1997).
16. Jhulki, S. *et al.* Solution-processable, crystalline π-conjugated two-dimensional polymers with high charge carrier mobility. *Chem* **6**(8), 2035–2045 (2020).
17. Johansson, A. A. & Stafström, S. Nonadiabatic simulations of polaron dynamics. *Phys. Rev. B* **69**(23), 235205 (2004).
18. Junior, L. A. R. & Stafström, S. Polaron dynamics in anisotropic Holstein-Peierls systems. *Phys. Chem. Chem. Phys.* **19**(5), 4078–4084 (2017).
19. Kotov, V. N., Uchoa, B., Pereira, V. M., Guinea, F. & Neto, A. C. Electron-electron interactions in graphene: Current status and perspectives. *Rev. Mod. Phys.* **84**(3), 1067 (2012).
20. Lee, C., Wei, X., Kysar, J. W. & Hone, J. Measurement of the elastic properties and intrinsic strength of monolayer graphene. *Science* **5887**, 385–388 (2008).
21. Lee, M. H., Aragó, J. & Troisi, A. Charge dynamics in organic photovoltaic materials: Interplay between quantum diffusion and quantum relaxation. *J. Phys. Chem. C* **119**(27), 14989–14998 (2015).
22. Lima, M. P. & e Silva, G. M. Dynamical evolution of polaron to bipolaron in conjugated polymers. *Phys. Rev. B* **74**(22), 224304 (2006).
23. Mozafari, E. & Stafström, S. Polaron dynamics in a two-dimensional Holstein-Peierls system. *J. Chem. Phys.* **138**(18), 184104 (2013).
24. Ono, Y. & Terai, A. Motion of charged soliton in polyacetylene due to electric field. *J. Phys. Soc. Jpn.* **59**(8), 2893–2904 (1990).
25. Peierls, R. Zur theorie des diamagnetismus von leitungselektronen. *Z. Phys.* **80**(11–12), 763–791 (1933).
26. Pereira Junior, M. L. *et al.* Charge transport mechanism in chevron-graphene nanoribbons. *J. Phys. Chem. C* **124**(41), 22392–22398 (2020).
27. Ribeiro, L. A. Jr. *et al.* Transport of polarons in graphene nanoribbons. *J. Phys. Chem. Lett.* **6**(3), 510–514 (2015).
28. Su, W. Soliton excitations in a commensurability 2 mixed peierls system. *Solid State Commun.* **48**(5), 479–481 (1983).
29. Su, W. & Schrieffer, J. Soliton dynamics in polyacetylene. *Proc. Natl. Acad. Sci.* **77**(10), 5626–5629 (1980).
30. Su, W., Schrieffer, J. & Heeger, A. J. Solitons in polyacetylene. *Phys. Rev. Lett.* **42**(25), 1698 (1979).
31. Su, W.-P., Schrieffer, J. & Heeger, A. Soliton excitations in polyacetylene. *Phys. Rev. B* **22**(4), 2099 (1980).
32. Takayama, H., Lin-Liu, Y. R. & Maki, K. Continuum model for solitons in polyacetylene. *Phys. Rev. B* **21**(6), 2388 (1980).
33. Terai, A. & Ono, Y. Electric field induced depinning of a charged soliton from an impurity center in polyacetylene. *J. Phys. Soc. Jpn.* **60**(1), 196–203 (1991).
34. Xu, Y., Zhang, F. & Feng, X. Patterning of conjugated polymers for organic optoelectronic devices. *Small* **7**(10), 1338–1360 (2011).
35. Zhang, L. *et al.* Toward highly sensitive polymer photodetectors by molecular engineering. *Adv. Mater.* **27**(41), 6496–6503 (2015).

Acknowledgements

The authors gratefully acknowledge the financial support from Brazilian Research Councils CNPq, CAPES, and FAPDF. P.H.O.N., and G.M.e S. gratefully acknowledge, respectively, the financial support from FAP-DF grants 0193.001662/2017, and 0193.001766/2017. G.M.e S. gratefully acknowledge the financial support from CNPq grants 304637/2018-1.

Author contributions

T.S.A.C., P.H.O.N and G.M.e S. wrote the main manuscript and analyzed the results. G.M.e S. developed the simulation code. P.H.O.N and G.M.e S. reviewed the manuscript. All authors wrote the main manuscript text, prepared figures 1-3, and reviewed the manuscript.

Competing interests

The authors declare no competing interests.

Additional information

Correspondence and requests for materials should be addressed to G.M.S.

Reprints and permissions information is available at www.nature.com/reprints.

APPENDIX B

PUBLISHED PAPERS (GRAPHENE NANORIBBONS)

B.1 PAPER B1

Charge transport in cove-type graphene nanoribbons: The role of quasiparticles

Tiago de Sousa Araújo Cassiano

Leonardo Evaristo de Sousa

Luiz Antônio Ribeiro Junior

Geraldo Magela e Silva

Pedro Henrique de Oliveira Neto

Synthetic Metals 287 (2022) 117056

10.1016/j.synthmet.2022.117056

B.2 PAPER B2

Regulating Polaron Transport Regime via Heterojunction Engineering in Cove-Type Graphene Nanoribbons

---

Tiago de Sousa Araújo Cassiano

Luiz Antônio Ribeiro Junior

Pedro Henrique de Oliveira Neto

Geraldo Magela e Silva

Adv. Theory Simul. 2023, 2200877

10.1002/adts.202200877

B.3 PAPER B3

Quasiparticles in Graphene Nanoribbon Heterojunctions: Insights from a Simplified One-Dimensional Model

---

Tiago de Sousa Araújo Cassiano

Pedro Henrique de Oliveira Neto

Geraldo Magela e Silva

J. Phys. Chem. C 2023, 127, 29, 14293–14302

10.1021/acs.jpcc.3c02553

B.4 PAPER B4

Thermally-induced charge carrier population control on graphene nanoribbons

---

Tiago de Sousa Araújo Cassiano

Geraldo Magela e Silva

Pedro Henrique de Oliveira Neto

Mater. Adv., 2024, 5, 4668-4678

10.1039/d3ma01181j

Volume 5
Number 11
7 June 2024
Pages 4527–4946

Materials Advances

rsc.li/materials-advances

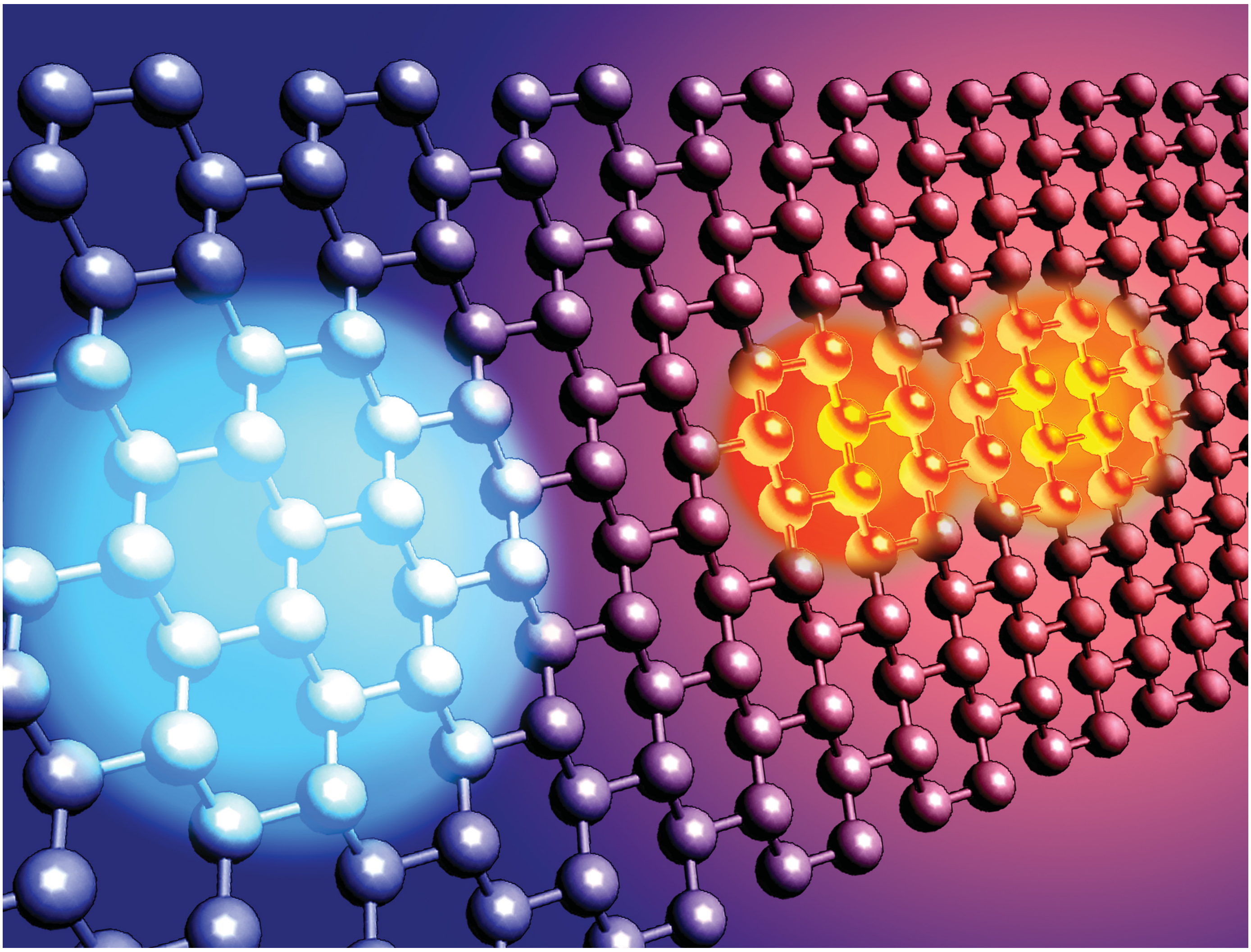

ISSN 2633-5409

ROYAL SOCIETY OF CHEMISTRY

PAPER
Geraldo Magela e Silva *et al.*
Thermally-induced charge carrier population control on graphene nanoribbons

Materials
Advances

ROYAL SOCIETY
OF CHEMISTRY

PAPER

View Article Online
View Journal | View Issue

Check for updates

Cite this: *Mater. Adv.*, 2024, 5, 4668

Received 28th December 2023,
Accepted 25th February 2024

DOI: 10.1039/d3ma01181j

rsc.li/materials-advances

Thermally-induced charge carrier population control on graphene nanoribbons†

Tiago de Sousa Araújo Cassiano, [a] Geraldo Magela e Silva *[a] and
Pedro Henrique de Oliveira Neto [ab]

Organic thermoelectric devices allow the conversion of heat into electricity in a sustainable way, making them strong candidates to solve the present energy crisis. In this context, integrating graphene nanoribbons (GNRs) into thermoelectrics holds great potential for addressing this challenge. The development of a physical description of charge carriers under thermal influence is a paramount step toward this objective. However, to this day, the effects of temperature on charged quasiparticles hosted on GNRs remain elusive. In this work, we propose an adaptation to the long-established Su–Schrieffer–Heeger (SSH) model Hamiltonian to accommodate thermal effects on GNRs. The results show that random lattice deformations can significantly alter polarons' and bipolarons' localization profiles. Moreover, we report a thermally-induced re-balance of carrier stability. As temperature increases, the probability of observing bipolarons decays in favor of the formation of two independent polarons. The results are especially relevant to Seeback-based thermoelectrics because they rely on temperature gradients. With the thermal stability of charge carriers, local thermal differences could regulate GNR-based currents with quasiparticle population control.

1 Introduction

The interest in thermoelectric devices has been revigorated in recent years. The potential of direct energy conversion from heat to electricity offers a promising avenue for addressing the current energy crisis.[1] In this sense, organic-based apparatuses are particularly attractive due to their inherent flexibility, low weight, low cost, and sustainable production.[2] With the recent rise of 2D materials, the idea of envisioning future organic thermoelectric applications with them is gaining momentum.

Since the isolation of graphene about 20 years ago, 2D materials have been driving a revolution in materials science. Graphene derivatives play a special role in this development. Most of their appeal resorts to the emergence of unique quantum phenomena after simple structural/environmental changes.[3–10] Nowadays, this attribute is the core of novel optoelectronic devices. Concerning semiconducting apparatuses, graphene nanoribbons (GNRs) stand out as the flagship choice in ultra-narrow applications. Among the many edge shapes,[3,11] the armchair type (AGNR) has an encouraging prospect, already integrating novel devices.[5,11,12] Given this scenario, using GNRs in next-generation thermoelectric devices is a natural path to proceed.[13]

Charge transport is fundamental for the description of the thermoelectric effect. In organic materials, the mechanism is driven by charged quasiparticles. They are polarized defects coupled with phonon clouds resulting from the collective response of the system.[14,15] The polaron, a half-spin structure of charge e, is usually the main carrier during transport. Besides its importance, other high-order quasiparticles can emerge during the transport mechanism. In a highly doped configuration,[16,17] two independent polarons can merge together, recombining into a new carrier known as a bipolaron.[18] This bosonic quasiparticle has twice the polaron's charge. Naturally, it is an active carrier with its own transport and magnetic properties. Importantly, bipolarons also participate in photonic mechanisms[19] because the scattering process may induce the formation of excitonic quasiparticles.[16,18,20] Therefore, the stability of polarons and bipolarons reverberates in electronic and optical performance.

Importantly, due to the coupled nature of a charged quasiparticle, its shape and stability directly impact the mobility and effective mass. Therefore, characterizing charge carriers allows to predict performance capabilities and provides new insights into transport mechanisms. Such a strategy had previously led to important results for conjugated polymers,[21–24] GNRs,[6,25–27] and molecular crystals.[28,29]

However, describing the charge carriers is not enough to understand thermoelectric effects. A realistic physical description

---

[a] Institute of Physics, University of Brasília, 70919-970, Brasília, Brazil.
E-mail: magela@unb.br
[b] International Center of Physics, University of Brasília, 70919-970, Brasília, Brazil

† Electronic supplementary information (ESI) available. See DOI: https://doi.org/10.1039/d3ma01181j

requires an explicit consideration of thermal response. Substantial effort was directed to developing adequate strategies.[30] The lattice can be highly sensitive to thermal influence, making the use of hybrid Hamiltonians, with explicit electronic and lattice interactions, a desirable approach.[30] The matter is especially relevant when considering systems with a strong electron–phonon coupling. In a hybrid Hamiltonian approach, one can model thermal effects as random distortions of the lattice bonds.[31–33] In this context, the Su–Schrieffer–Heeger hybrid Hamiltonian[15,34] is a robust framework to investigate thermal mechanisms in quantum systems, being the backbone of important studies.[31,32,35–37]

Progress was made through this route, which helped uncover the functioning of intricate phenomena in highly confined materials. For instance, with a mixed 1D Hamiltonian, Troisi recovered the long-established mobility power law dependence with temperature in rubrene crystals.[28,29] Other studies reported a thermal-assisted reduction of electron–hole pair binding energy,[32] the hampering of polaron stability,[33,36] and shortening of quasiparticle recombination[37] in conjugated polymers. These works demonstrate that the theoretical investigation of thermal properties holds a latent potential to elucidate and provide insights in nanoelectronics and photonics. However, besides the importance of GNRs, the impact of thermal influence over its charge carriers remains an open topic.

In this work, we simulate the formation of polarons and bipolarons on armchair graphene nanoribbons under several temperature regimes. The model consists of an adaptation of the SSH hybrid Hamiltonian. The proposed modification aims to consider thermal effects as bond distortions. We selected four armchair nanoribbons with different widths to implement the study. Bipolaron stability is determined. The results show that raising the temperature can progressively hamper bipolaron cohesion, favoring the formation of independent polaron pairs instead. Additionally, we report an increase of 25% of polarons for a temperature variation of 150 K. The results could benefit future thermoelectric applications based on the Seeback effect while providing a phyisically accurate description of charge carriers under thermal influence.

2 Methodology

Four armchair nanoribbons were simulated. Three of them are illustrated in Fig. 1. Fig. 1(a), (b), and (c) present, respectively, the 4, 6, and 9AGNR structures. Their labels correspond to the number of carbon atoms along the width axis, as demonstrated in Fig. 1(a) for the 4AGNR. For each GNR, the SSH model Hamiltonian H consists of the sum of the lattice (H_{latt}) and electronic (H_{elec}) contributions:[15,22,23,34]

$$H = H_{\text{latt}} + H_{\text{elec}} \tag{1}$$

The former is modeled under the Harmonic approximation, reading[8,38,39]

$$H_{\text{latt}} = \frac{K}{2}\sum_{\langle i,j\rangle}{\eta_{i,j}}^2 + \sum_i \frac{P_i^2}{2M}. \tag{2}$$

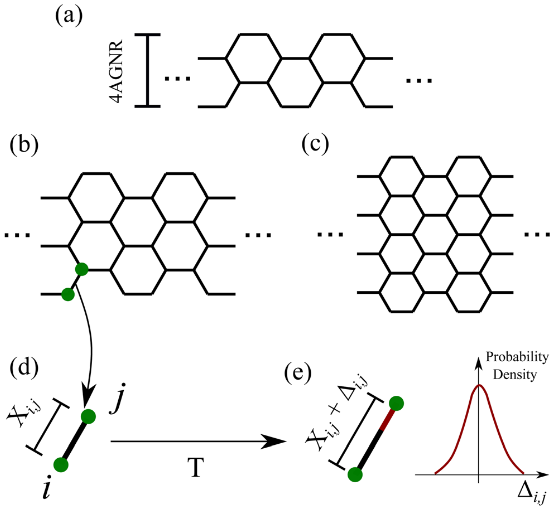

Fig. 1 Schematic representation of some of the armchair nanoribbons simulated and the modeling applied. The structure of the 4AGNR is displayed in (a). The label corresponds to the number of carbon atoms along the width axis. The 6AGNR and 9AGNR are displayed, respectively, in (b) and (c). The inclusion of thermal effects is illustrated in (d) and (e). (d) shows the bond distortion derived from the stationary algorithm. In the presence of heat, this bond is further deformed by a random noise sampled by a distribution, as shown in (e).

Here, K is the harmonic constant, M is the site mass, P_i is the conjugated momentum of the i-th site, and $\eta_{i,j}$ is the deformation of the bond connecting sites i and j. The bracket at the lower sum index indicates a summation over neighboring bonds.

The electronic part is treated through a tight-binding formalism, which models the π-electron hopping as[38]

$$H_{\text{elec}} = -\sum_{\langle i,j\rangle,s}\left(t_{i,j}C_{i,s}^{\dagger}C_{j,s} + \text{h.c.}\right), \tag{3}$$

where $C_{i,s}^{\dagger}$ and $C_{i,s}$ stand for the creation and annihilation operator of a π-electron with spin s at the i-th site. In addition, $t_{i,j}$ is the hopping integral linking sites i and j. Here, h.c. stands for the hermitian complex. Both the lattice and electronic interactions are subjected to periodic boundary conditions.

The electronic and lattice interactions are coupled through a first-order expansion of the hopping integral in the pristine configuration (t_0):[15,21,34]

$$t_{i,j} = (t_0 - \alpha\eta_{i,j}). \tag{4}$$

The lattice coupling to the hopping integral is determined by the electron–phonon coupling α.

Following the Ehrenfest Theorem, the lattice solution can be obtained by solving the Euler–Lagrange equations of the expected value of the Lagrangian.[8,21,38] In the case of stationary configurations, when no kinetic interaction is considered ($P_i = 0$), the minimization condition simplifies to:

$$\frac{\partial\langle H\rangle}{\partial\eta_{i,j}} = 0. \tag{5}$$

Here, $\langle H\rangle \equiv \langle\Psi|H|\Psi\rangle$ is the expected value of the potential energy. The state $|\Psi\rangle$ is a Slater determinant formed by the occupied π-electron orbitals. After explicit manipulation, this expression turns into[38]

$$\eta_{i,j} = -\frac{\alpha}{K}(\rho_{i,j} + \text{c.c.}), \tag{6}$$

where $\rho_{i,j}$ is the (i,j) element of the charge density matrix,

$$\rho_{i,j} = \sum_{k,s}{}' \psi^*_{ks}(i)\psi_{ks}(j), \tag{7}$$

and $\psi_{ks}(i)$ is the k-th eigenstate projected at the i-th site with spin s. The prime sign stands for a sum over the occupied states. Here, c.c. stands for the conjugated complex.

Since the Hamiltonian explicitly depends on the lattice configuration, a self-consistent algorithm is applied to solve the hybrid model.[8] The procedure begins by choosing an appropriate guess for the bond distortion set $\{\eta_{i,j}\}$ (which is usually taken as 0). Then, H_{elec} can be numerically built and diagonalized, yielding the corresponding eigenvectors and eigenvalues. The new electronic solution is then applied to recalculate $\{\eta_{i,j}\}$ according to eqn (6). Then, the newly calculated lattice configuration is compared with the previous set. This involves calculating the root mean squared error between the two solutions. If the difference is below a preset threshold, the algorithm stops. Otherwise, the procedure repeats by using the updated $\{\eta_{i,j}\}$ in the initial step.

Charge states are obtained by removing the electrons from the material. This means extracting spin–orbitals from the neutral state Slater determinant. For instance, a positive polaron is created after removing an electron occupying the highest occupied molecular orbital (HOMO). In turn, a positive bipolaron emerges after removing two electrons from the HOMO. The corresponding carriers with a negative charge are obtainable by adding electrons to the unoccupied molecular orbital (LUMO). Importantly, the positive and negative quasiparticles are bound to exhibit the same properties due to the electron–hole symmetry.

The parameters of the model Hamiltonian are based on previous studies on AGNRs and similar conjugated systems. That is $t_0 = 2.7$ eV,[4,40] $K = 21$ eV Å^{-2},[34,41] and $\alpha = 5.2$ eV Å^{-1}.[26,39,42,43]

A. Thermal effects

Temperature effects can be modeled as noise distortions around the stationary lattice configuration.[30–32] Suppose that the stationary algorithm yields a lattice configuration in which the sites i and j are linked by a bond with a length of $X_{i,j}$. The thermal-corrected bond length for a temperature T is the sum of a random disturbance ($\Delta^k_{i,j}(T)$) to $X_{i,j}$:

$$X^k_{i,j}(T) = X_{i,j} + \Delta^k_{i,j}(T), \tag{8}$$

where k labels the ensemble member to which this distortion corresponds.

However, it is always possible to recognize $\eta_{i,j}$ into $X_{i,j}$ because they differ only by a constant. In other words,

$$X_{i,j} = L_0 + \eta_{i,j}, \tag{9}$$

where $L_0 = 1.41$ Å is the lattice parameter.

Because of that, the lattice changes due to thermal effects can be thought as corrections to the bond length distortion, turning each $\eta_{i,j}$ into

$$\eta^k_{i,j}(T) = \eta_{i,j} + \Delta^k_{i,j}(T). \tag{10}$$

The $\Delta^k_{i,j}(T)$ is sampled according to the Boltzmann probability distribution:[30,32,33]

$$I(x,T) \propto \exp\left(-\frac{Kx^2}{2k_{\text{b}}T}\right). \tag{11}$$

Here, k_{b} is the Boltzmann constant and x is the distortion random variable. For each ensemble member, the sampling is done on all existing bonds. The process consists of two steps: (1) for each bond, an x value is sampled from the distribution in eqn (11) through the Box–Muller algorithm; (2) the distortions are implemented in the lattice, rendering a new set $\{\eta\}$. Then, H_{elec} is diagonalized using the updated lattice, yielding the corrected eigenvalues and eigenvectors of this particular configuration. Finally, ensemble statistics will provide the physical description of the GNRs. As a side remark, we recall that the normalization of the distribution is irrelevant for the sampling because it is a common factor for all x at a fixed T.

Fig. 1(d) and (e) illustrate the sampling procedure. In Fig. 1(d), the converged bond length $X_{i,j}$ connects the sites i and j. For a finite temperature T, $X_{i,j}$ is corrected by a random distortion $\Delta_{i,j}$ that is sampled from the distribution in eqn (11). The result is a bond distorted from its equilibrium length, as shown in Fig. 1(e). This process is repeated for all unique bonds, giving one ensemble member as the end result. By repeating the procedure, an ensemble of GNR configurations is generated. Their collective response will translate into the physical description of the material under thermal effects.

All cases were simulated by constructing ensembles with 5000 members. This number was found to be adequate after verifying the statistical robustness of averaging processes. Fig. S1 (ESI†) illustrates this test. The variation of the total energy in the neutral, polaron and bipolaron states is presented in Fig. S1(a), (c) and (d) (ESI†). The solid lines represent the energy of a given ensemble element, while the dashed lines are the corresponding cumulative averages. As can be seen, the solid curves display an oscillating behavior. On the other hand, the dashed lines are stable, exhibiting no significant changes when the ensemble has more than 1000 elements. Therefore, any succeeding quantity that relies solely on the total energies should be equally stable.

We emphasize that a small ensemble can lead to an under-represented thermal response. To see this, we present the zoomed versions of Fig. S1(a), (c) and (d) (ESI†), respectively, in Fig. S1(b), (d) and (e) (ESI†). As can be seen, the dashed curves are not straight lines anymore. For a small ensemble, the cumulative mean is not stable.

In the following discussion, the k index will be suppressed when its presence is not relevant. We emphasize that ordering the ensemble geometries has no physical meaning and is only important for the sake of clarity and practical reasons. Finally, all the simulated results obtained using the traditional model (with no explicit consideration of thermal effects) will be referred to as the "0 K" case.

In addition, we recall that in general, thermal effects influence the electrons through changes in the electronic occupation. Since electrons are fermionic particles, the Fermi–Dirac distribution determines the temperature dependence of the occupation. This effect was not included because all the simulated GNRs are intrinsic semiconductors, with a gap of ≈ 1–3 eV. In such cases, a significant modification in the electronic occupation is only visible for thermal baths at high temperatures ≈ 5000 K. Since we are concerned with near-ambient temperatures, the occupation change is negligible. Naturally, the situation can drastically change when dealing with semimetals, metals, and highly doped semiconductors. For those materials, even a low-temperature reservoir can thermally excite electrons to the conduction band. The impact of thermal effects on the electronic occupation depends on the actual density of charge carriers. In a high-density charge carrier regime, the system has many particles at the conductance (or valence) band. In such cases, occupation changes become relevant because there is a large number of particles to fill the vacant states. On the other hand, the intra-band excitation, although present, has a minimal impact. This is because it alters the occupation of only a few electrons (or holes).

Note that this does not mean that electrons are insensitive to thermal effects in the model. We recall that the electronic Hamiltonian has a contribution from the lattice through the electron–phonon coupling. Therefore, the thermal distortions in the sites' positions reverberate due to the electronic eigenstates and eigenvalues.

B. Bipolaron stability

The bipolaron binding energy (BE) can be estimated as the energy difference between the bipolaron formation energy ($\mathrm{FE_{bip}}$) and two times the polaron formation energy ($\mathrm{FE_{pol}}$):[44]

$$\mathrm{BE} = \mathrm{FE_{bip}} - 2\mathrm{FE_{pol}}, \tag{12}$$

where

$$\mathrm{FE_{bip}} = \mathrm{SCF_{bip}} - \mathrm{SCF_{neutr}} \text{ and}$$
$$\mathrm{FE_{pol}} = \mathrm{SCF_{pol}} - \mathrm{SCF_{neutr}}. \tag{13}$$

Here, $\mathrm{SCF_{bip/pol}}$ is the self-consistent energy obtained from the stationary algorithm for the bipolaron/polaron state. In a similar manner, $\mathrm{SCF_{neutr}}$ is the corresponding energy for the neutral configuration. If $\mathrm{BE} > 0$, the formation of two independent polarons is energetically more favorable than a single bipolaron. In other words, bipolaron formation would occur only with the aid of an external agent. When $\mathrm{BE} < 0$, the opposite becomes true: bipolarons are expected to form spontaneously.

It is important to note that $\mathrm{SCF_{bip}}$, $\mathrm{SCF_{pol}}$, and $\mathrm{SCF_{neutr}}$ are distributions when considering thermal effects. Each state is represented by an ensemble of 5000 separate calculations. For this reason, eqn (12) needs to be adapted. First, it is important to realize that each ensemble member shares the same probability of being observable. In addition, BE should be a distribution that obeys eqn (12). Therefore, BE calculation is done by the sampling values obtained from $\mathrm{FE_{bip}}$ and $\mathrm{FE_{pol}}$ and applying them to eqn (12). However, although independent in principle, the polaron and bipolaron formation energies cannot be sampled separately for BE calculation. During each selection process, the same $\mathrm{SCF_{neutr}}$ sampled energy was used to calculate both $\mathrm{FE_{bip}}$ and $\mathrm{FE_{pol}}$. That way, we avoid the consideration of artificial recombinations involving ground-state lattice reorganization.

C. Dimerization ratio

An important feature of conjugated materials is the dimerization of neighboring bonds. Its presence is a sign of lattice cohesion and can be associated with optical/electronic properties.[15,45] For this reason, tracking changes on this attribute can be a potential source for new insights. Here, we propose a simple calculation to estimate dimerization. For an ensemble of size N_{ens} and a GNR with L bonds, the dimerization ratio (DR) is:

$$\mathrm{DR}(T) = \sum_{k}^{N} \sum_{\langle i,j \rangle}^{L} \frac{\mathrm{sign}(h_{i,j})\mathrm{sign}(h^{k}_{i,j}(T))}{N_{\mathrm{ens}} L}, \tag{14}$$

where the product $\mathrm{sign}(\eta_{i,j})\mathrm{sign}(\eta^{k}_{i,j}(T))$ is 1 when dimerization is preserved or is -1 when it is not preserved. The sum, which is normalized by the denominator $N_{\mathrm{ens}}L$, yields the ratio of bonds whose sign (if it contracts or expands around the pristine length) is preserved after the thermally-induced deformation. The ratio can be readily converted to a percentage by multiplying it by 100.

3 Results

Our study begins by considering the effects of temperature in neutral AGNRs. The results will serve as a reference for the succeeding analysis on charged states. Fig. 2 displays the thermal influence on the 4AGNR's lattice. Fig. 2(a)–(c) exhibit the distortion distribution for the three types of bonds present in the hexagonal lattice: the *trans* (/), *cis* (\) and vertical (|), respectively. Near each distribution plot, a GNR slice is placed with the corresponding bond type highlighted in yellow. The colors of the curves indicate the temperature: 95 K (blue), 197 K (red), and 350 K (green). As can be seen, all three blue curves contain two distinguished peaks, one centralized in the $\eta > 0$ region and the other in the negative zone. The bond distortion length associated with each peak corresponds to the unique bonds at 0 K. As the temperature rises, the probability density drops around the peaks and the distribution begins to spread over. This is a direct result of sampling the bonds using eqn (11) because the standard deviation is proportional to the temperature.

It is also suggested to look at the order parameter heatmap of ensemble members. Fig. 2(d)–(f) correspond to 0 K, 95 K and 350 K, respectively. For all cases, dark tones indicate a bond

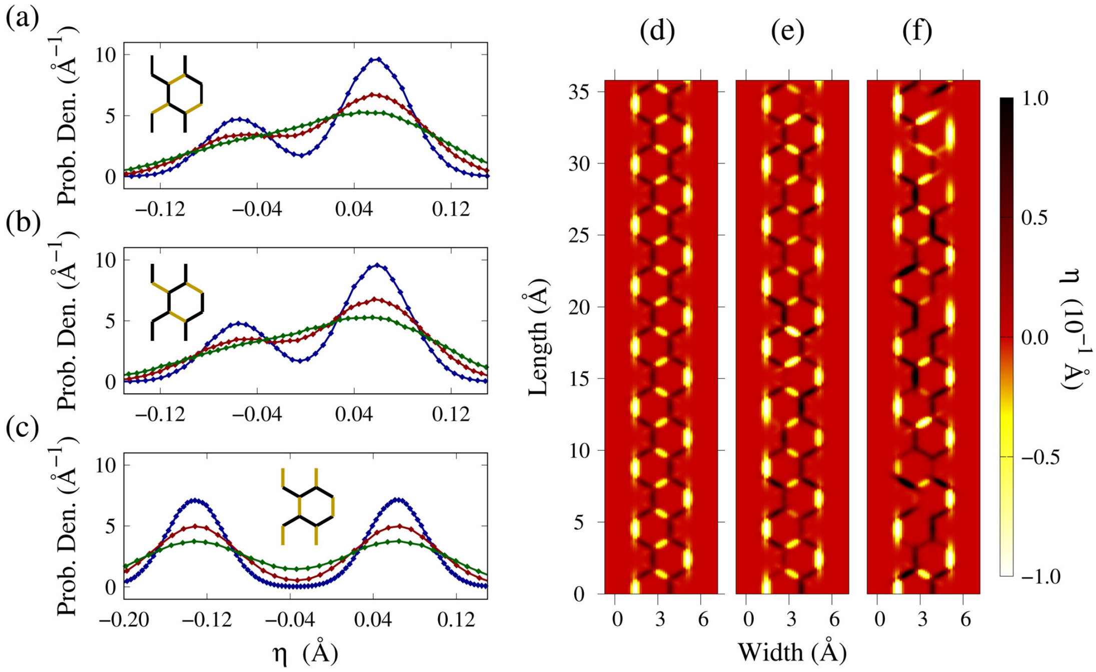

Fig. 2 Bond deformations in the presence of thermal effects in the neutral 4AGNR. (a), (b) and (c) are, respectively, the deformation distributions for the *trans* (/), *cis* (\) and vertical (|) bonds. In each plot, a GNR slice illustration is placed to exhibit, in yellow, the corresponding bond type. The blue, red, and green curves correspond to T = 95, 197, and 350 K. In addition, (d), (e), and (f) depict the bond deformation heatmaps for T = 0, 95, and 350 K. The dark colors refer to expanded bonds, while light tones indicate contraction.

expansion, while light colors represent a contraction. Bonds in red display no distortion. When temperature is not considered, the 4AGNR bonds form an alternating pattern, intercalating between contraction and expansion along the width lines. This is the dimerization effect, which is widely reported for GNRs[8,38] and other conjugated materials such as polymers.[15,34] As the temperature increases, this pattern is progressively destroyed. Some bonds that were once contracting at 0 K start expanding now and *vice versa*. Another possibility is for the bond to display no distortion at all, indicated by the color red. The results show that thermal effects can significantly change the lattice. Therefore, any mechanism that rely, to some extent, on lattice properties is expected to be also influenced. This is especially relevant for quasiparticle formation that usually depends on the lattice symmetry for the generation of stable carriers. Therefore, it is expected that carriers created at high-temperature regimes are less stable than the 0 K case.

One may notice that the profile for 197 K is considerably closer to the 350 K configuration than it is from the 95 K configuration. In other words, the thermal response in a high T regime is expected to be less sensitive to temperature variations. This trend will be visible in all the following results.

Fig. S3–S5 (ESI†) present the same panel of Fig. 3 for the 6, 7, and 9AGNR. As in the 4AGNR case, these nanoribbon bonds display an increasing degree of expansion or shrinking as the temperature rises. Moreover, wider nanoribbons present bond length distributions with peaks closer to 0 Å. Because of that, thermal distortions in wider nanoribbons are more prone to change the bonding state (if it is expanding or shrinking). Therefore, the result foreshadows an enhanced sensitivity of wider nanoribbons to dimerization changes.

To further explore this indication, we proceed to analyze the bond distributions more systematically. Here, we present Fig. 3(a)–(d). They are the corresponding heatmaps of distortion distribution of all bond types combined for the 4, 6, 7, and 9AGNR. The yellow tones indicate a high probability of occurrence, while purple represents a low probability. A white line is drawn at η = 0 Å to serve as a guide. Each different nanoribbon has at least two high-probability regions. The first one corresponds to the expanded bonds ($\eta > 0$) and the other represents contraction ($\eta < 0$). The position of these zones along the η axis depends on the nanoribbon width. For instance, when $T \approx 95$ K, the 4AGNR heatmap has an orange region near η = 0.06 Å, while the 6AGNR's corresponding peak is at η = 0.09 Å. In all cases, increasing the temperature seems to spread the high-probability regions over the η-axis, a response already observed in Fig. 2(a)–(c).

When T is high enough, the peaks that once were related to contracted bonds begin to overlap with the expansion peaks for all GNRs. As a result, the bond distortion sign begins to flip in some configurations. To better visualize the effect, we present DR as a function of the temperature for the 4 (blue), 6 (red),

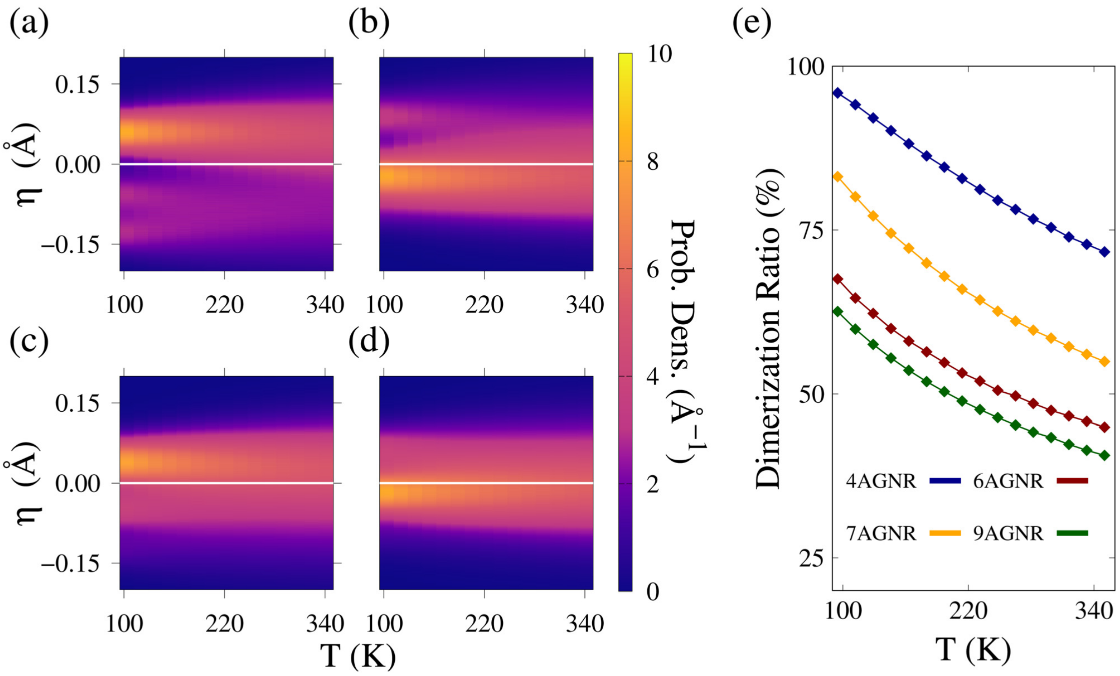

Fig. 3 Thermal effects over bond distortions in the AGNRs. (a)–(d) show, respectively, the bond distortion probability density heatmaps of the neutral 4, 6, 7, and 9AGNR. The regions in yellow have a high probability density, while those in purple display a low density. A white line at η = 0 Å is drawn in all heatmaps to serve as a reference. (e) presents the dimerization ratio (DZ) as a function of the temperature for the 4 (blue), 6 (red), 7 (yellow), and 9AGNR (green).

7 (yellow), and 9AGNR (green) as shown in Fig. 3(e). Qualitatively, all curves share the same behavior: as T increases, DR decays monotonically. This is an expected outcome. It results from the growing overlap between the distributions' peaks associated with contracted and expanded bonds.

Some nanoribbons are more prone to dimerization degradation than others. At 95 K, the 4AGNR has DR $\approx$ 96%, bearing almost no change compared with the 0 K solution. On the other hand, the 9AGNR has a DR of $\approx$62% for the same temperature. This is a result of the initial position of the η peaks shown in Fig. 2(a)–(d). The peaks closer to 0 Å will cross this value at lower temperatures, providing a non-zero probability to the flipping of the distortion sign of some bonds. The wider nanoribbons present bonds closer to this region. Therefore, the results suggest that width extension enhances the temperature changes in the nanoribbon structural stability. Since quasiparticle formation depends on lattice cohesion, charge carriers hosted on wider nanoribbons are expected to be less stable.

Although wider GNRs suffer more from temperature effects, the relation is not monotonic. For instance, the 6AGNR suffers a stronger dimerization degradation than the 7AGNR. That is due to the grouping of armchair families.[10,46] Members belonging to the same family are expected to group together, making width effects to be non-monotonous. Because of that, the 4AGNR and 7AGNR have to display a similar response. The same applies to the 6AGNR and the 9AGNR. A clear example of such behavior is the dependence of the AGNR energy bandgap on the nanoribbon's width, as widely reported the in literature.[10,46]

Although temperature significantly impacts the dimerization of individual members of the ensemble, we observe no effects when considering the mean values of η. Fig. S1 (ESI†) displays this calculation for the 4AGNR at 300 K. Four ensemble individuals are displayed in Fig. S1(a) (ESI†). The average of them, along with the remaining 4996 units of the set, yields the heatmap shown in Fig. S1(b) (ESI†). This profile is equivalent to the one shown in Fig. 2(d). The explanation for this lies in the Gaussian form of the probability distribution used to sample the distortions. The average of $\Delta^k_{i,j}(T)$ is zero for any T because eqn (11) is symmetric. Therefore, summing out the contribution from each ensemble member will just set each bond distortion to its original value from the stationary algorithm, $\eta_{i,j}$.

Provided the neutral state's general response, we proceed to analyze the effects on the charged states. Fig. 4(a) presents the charge density (ρ) for the 7AGNR. Four heatmaps are displayed, corresponding to individuals from ensembles of different temperatures. Hot colors signal high charge accumulation, while cold tones indicate a low local density. As can be seen, the carrier morphology suffers substantial changes due to temperature. The symmetry patterns present in the 0 K polaron are often eroded due to the random distortions. For instance, when T = 0 K, the amount of charge on the left side equals the right side. However,

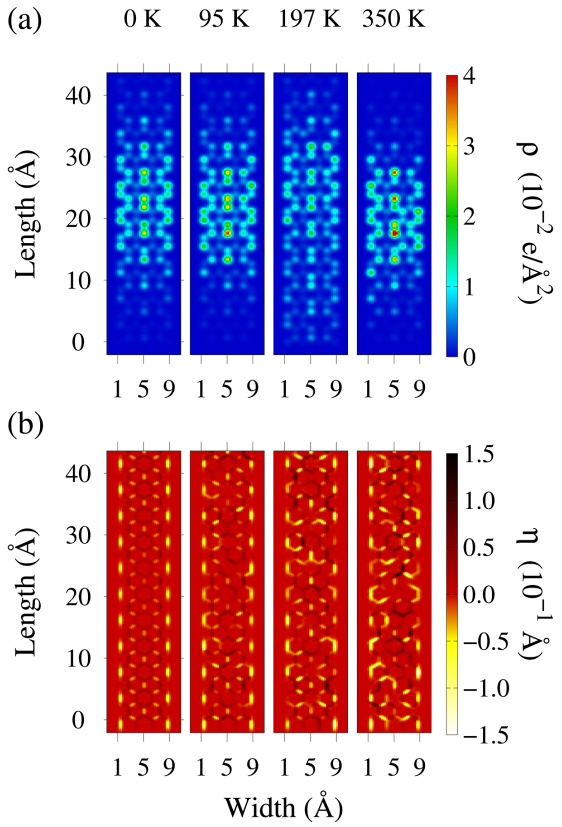

Fig. 4 Polaron localization profile in the 7AGNR. (a) displays the charge density heatmap of ensemble members at T = 0, 95, 197, and 350 K. The cold colors represent a low density, while hot tones indicate charge accumulation. In (b), the corresponding bond deformation heatmap is presented. Here, bonds in yellow contracted, and those in black expanded with respect to the lattice parameter L_0.

this symmetry is lost when considering the 197 K case. Here, the right side has slightly more charge. Changes in the quasiparticle size are observed too. The polarized region at 350 K extends over ≈30 Å, while the 0 K structure has a size of ≈25 Å. Similar asymmetries can be spotted for the other nanoribbons (not shown). These findings are consistent with previous studies on conjugated polymers, in which the polaronic picture of the carrier is challenged with increasing temperature.[33]

A complete overview of a charged quasiparticle requires examination of the nanoribbon lattice deformation profile. The order parameter heatmap is displayed in Fig. 4(b). At 0 K, a distinguishable local distortion is present at the center of the heatmap, representing the polaron local lattice deformation. Due to the coupling of carriers, the deformation size, shape, and magnitude directly impact the resulting charge accumulation.[6,26,43,47] Importantly, the lattice disarray can induce asymmetries in the charge profile. Previous works regarding charge profiles on conjugated polymers indicate that cohesion loss can potentially hinder the transport capability.[48] Here, we extend this reasoning by concluding that the thermally-induced random distortions may reduce the carrier's mobility. This is an expected outcome, corroborated by widely reported mobility degradation with increasing temperature in molecular crystals.[28,31,49] Confirmation of this response is achievable through dynamical simulations.

We remark that the profiles displayed in Fig. 4 cannot be interpreted as the average behavior of the nanoribbon in that temperature regime. These profiles are snapshots of individual ensemble members. Therefore, a comparison between these structures holds no physical significance. Only the collective response of the ensemble set has this meaning. The heatmaps are presented to illustrate how distorted the 0 K polaron picture becomes when temperature effects emerge.

Now, we move to quantitative analysis. Fig. 5(a)–(d) display the formation energy distributions of the 4AGNR at 100, 150, 200, and 350 K. The curves in red refer to the polaron state, while the ones in blue represent the bipolaron response. Regardless of the temperature magnitude, each state distribution exhibits a Gaussian-like shape with a well-defined peak. Moreover, the peak position of the polaron case is always at a lower energy than that of the bipolaron. This is an expected outcome, reflecting that the system requires more energy to create a bipolaron than a polaron. That should be the case because the additional charge requires a more profound lattice reorganization to form a localized polarized structure. However, as the temperature rises, an interesting effect begins to unfold: the distributions overlap. In other words, certain polaron states, assisted by thermal effects, are energetically more costly to form than bipolaronic configurations. This nonintuitive setting suggests that quasiparticle stability can be widely affected by thermally-induced distortions. The overlapping feature is present in all simulated GNRs.

The variants shown in Fig. 5 for the 6, 7, and 9AGNR are presented in Fig. S6–S8 (ESI†). Qualitatively, all nanoribbons display the same behavior: the polaron and bipolaron distributions are monomodal curves that begin to overlap when increasing the temperature. However, close analysis shows that the overlap degree depends on the width. This can be verified by comparing Fig. 5(d) with Fig. S8(d) (ESI†). We recall that the dispersion of the distribution is associated with the material thermal response. The broader the curve, the more intense the change induced by the distortions. Therefore, the result evidences that wider nanoribbons are more sensitive to thermal influence.

For some configurations, $\mathrm{EF_{bip}} < \mathrm{EF_{pol}}$. Then, one should expect that the bipolaron stability distribution (see eqn (12)) may have a non-zero probability of being positive. In other words, a non-zero temperature favors the destabilization of bipolarons, effectively facilitating polaron formation. To verify this reasoning, we present the bipolaron stability heatmaps in Fig. 6(a)–(d) for the 4, 6, 7, and 9AGNR, respectively. The colors indicate the probability density magnitude: the zones in blue have a high probability density. In turn, the BE regions in yellow have a low probability density. For each heatmap, a red line is drawn at BE = 0 eV to serve as a reference. Near this line, all distributions display a single strong blue signal. Then, the

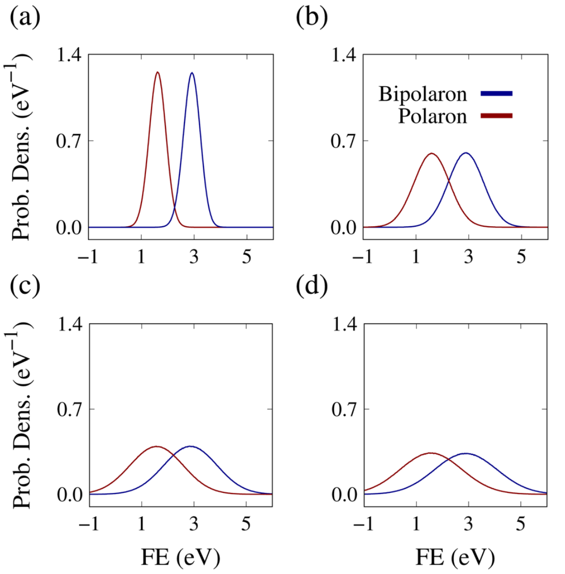

Fig. 5 4AGNR probability density distribution of the polaron (red) and bipolaron (blue) formation energies. (a)–(d) Refer to, respectively, T = 95, 197, 299, and 350 cases.

density progressively drops for BE values away from the central region. This behavior is characteristic of a monomodal distribution. The FE curves shown in Fig. 5 display a similar response.

Note that the center of the distributions is not at BE = 0 eV. In the absence of thermal effects, BE equals −0.36, −0.19, −0.23, and −0.10 eV for the 4, 6, 7, and 9AGNR, respectively. Therefore, bipolarons are more stable than two independent polarons when T = 0 K. As the temperature rises, the distribution expands along the y-axis, making high BE energy states accessible. A consequence of this feature is that the distributions begin to cross the red line, exhibiting a non-zero probability of occurring positive BE configurations.

That thermally-induced behavior has the potential to represent significant implications for GNR-based nanoelectronics. We recall that bipolarons are active agents in photonics. They are involved in excitonic formations, influencing the emission mechanism. Since temperature destabilizes bipolaron formation, thermal effects will reverberate due to the optical properties of GNRs. If bipolarons are prone to split into polarons, biexciton formation might be hampered. As a result, characteristic biexciton peaks at emission spectra are expected to drop with temperature increase. These findings could be explored in thermoelectric applications. Seeback-based gadgets make use of spatial temperature gradients to function. Then, the results suggest that the ratio of polaron/bipolaron

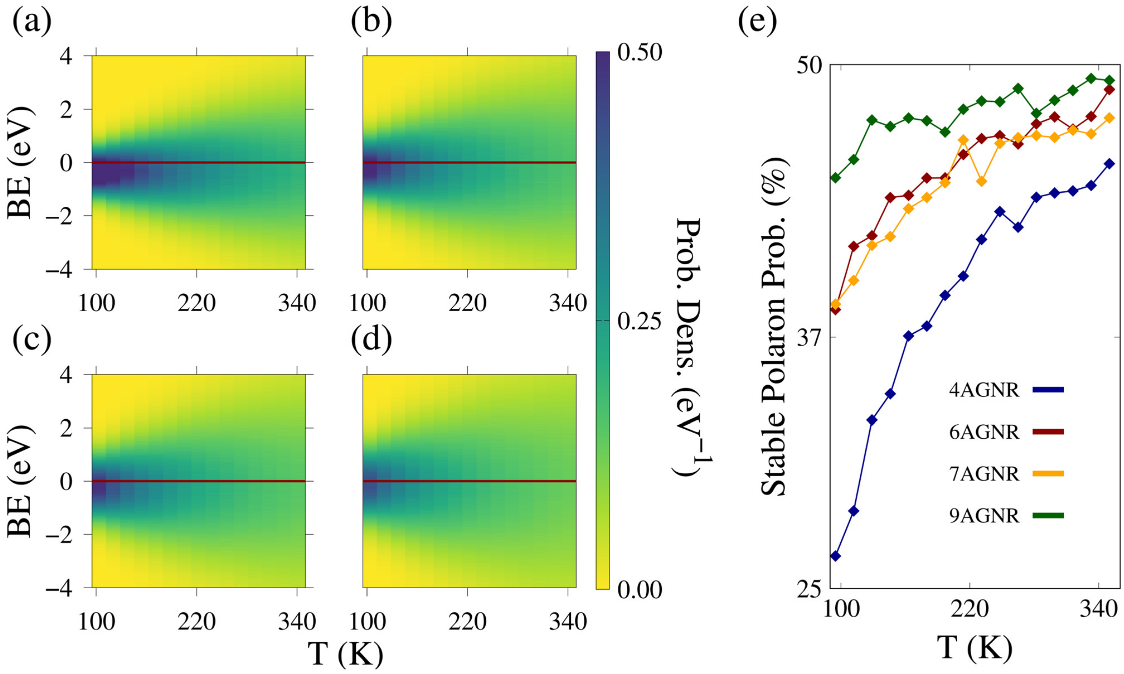

Fig. 6 (a)–(d) depict the bipolaron binding energy distributions heatmaps for the 4, 6, 7, and 9AGNR, respectively. The regions in blue present high probability density, while those in yellow have a low probability. (e) displays the percentage of probability of stable polarons as a function of the temperature. This quantity is obtained by integrating each BE distribution in the region BE > 0 eV. The colors of the curves indicate the nanoribbon width, following the same convention shown in Fig. 3.

populations will be different at the device's edges. Such configuration could be rationalized as a spin filter tool because polarons are fermionic carriers and bipolarons are bosons.

It is important to note that the current model does not include electron–electron repulsion terms. While these terms are pertinent in the context of collision-induced recombination[50,51] and magnetic processes,[52–54] their incorporation beyond these scenarios does not yield substantial enhancements for the model. The effect is to cause minor adjustments to the gap magnitude and quasiparticle profile. In the present case, the quasiparticles are isolated. Therefore, this addition can be avoided.

Moreover, the rising probability density for positive BE is bound to change charge transport efficiency. Bipolarons often present different transport properties compared with polarons.[6,44,47] Our results show that temperature favors the formation of polarons. Therefore, the polaron population is expected to grow with T. As a result, the nanoribbon charge transport mechanism could be characterized by polarons and their properties even in regimes of strong doping. This feature can affect future thermoelectric applications in which transport efficiency (*i.e.* the current magnitude) is temperature-dependent.

The degree of bipolaron destabilization depends on the nanoribbon width. To investigate this in detail, Fig. 6(e) presents the probability of obtaining two stable polarons as a function of the temperature. The curves were obtained by integrating the probability density curve inside the positive BE region. The color of the curves indicates the nanoribbon width, following the same convention shown in Fig. 3(e). As expected, increasing the temperature raises the probability of positive BE for all AGNRs. However, the nanoribbon width has a profound impact on the probability value. For instance, the 4AGNR has a 26% chance of having a configuration with two stable polarons at 95 K. When T = 350 K, this probability goes to 45%. At the same temperature, in the case of the 9AGNR, the probability escalates from 45% to 49%. Another point worth mentioning is that due to the monomodal character of BE distribution, the probability of positive BE cannot be greater than 50%. The reason is that the probability density also spreads towards the negative BE region. Consequently, at least half of the distribution will still have BE $<$ 0. This interesting result shows that one cannot indefinitely favor the bipolaron split through temperature increments.

4 Conclusion

In conclusion, we investigated the influence of thermal effects on the properties of armchair graphene nanoribbons. Four different width configurations are analyzed. The results show that temperature is an agent that erodes dimerization patterns. The degradation depends on the nanoribbon width. In general, it is shown that wider GNRs are more prone to lose this lattice cohesion.

When it comes to charged states, thermal effects induce significant changes in the formation energies of polarons and bipolarons. As an outcome of ensemble statistics, these quantities become distributions. Their dispersion increases with rising temperature. As a result, an interesting result emerges for high T: bipolaron and polaron FE probability density distributions overlap. This means that certain configurations display a lower bipolaron formation energy compared with a single polaron. Further investigation of these cases led to the calculation of bipolaron binding energy distribution. The results show that temperature promotes the occurrence of states with BE $>$ 0 eV, effectively favoring the formation of polarons instead of bipolarons. In contrast to 0 K simulations in which bipolarons are stable, here we report that almost 50% of the ensemble states contain stable polarons for high T. These unexpected results paint an encouraging prospect to envision thermoelectric devices that control the population of charge carriers. Moreover, the results illustrate the importance of including thermal effects to represent realistic scenarios.

Data availability

The data that support the findings of this study are available from the corresponding author upon reasonable request.

Author contributions

T. S. A. C. – conceptualization, data curation, formal analysis, methodology, validation, and writing – original draft preparation. G. M. S. – and P. H. O. N. – conceptualization, funding acquisition, formal analysis, visualization, validation, supervision, and writing – reviewing. All authors reviewed the manuscript.

Conflicts of interest

The authors declare no competing financial or non-financial interests.

Acknowledgements

The authors gratefully acknowledge the financial support from Brazilian Research Councils DC, (grant number 304637/2018-1) CAPES, and FAPDF. P. H. O. N. and G. M. S. gratefully acknowledge the financial support provided by FAPDF grants 00193-00001853/2023-15 and 00193-00001831/2023-47. G. M. S. and P. H. O. N. gratefully acknowledge the financial support provided by CNPq grants 304637/2018-1 and 306080/2022-2, respectively.

References

1 X.-L. Shi, J. Zou and Z.-G. Chen, Advanced thermoelectric design: from materials and structures to devices, *Chem. Rev.*, 2020, **120**(15), 7399–7515, DOI: 10.1021/acs.chemrev.0c00026.

2 S. Lee, S. Kim, A. Pathak, A. Tripathi, T. Qiao, Y. Lee, H. Lee and H. Y. Woo, Recent progress in organic thermoelectric

materials and devices, *Macromol. Res.*, 2020, **28**(6), 531–552, DOI: **10.1007/s13233-020-8116-y**.

3 Y. Yano, N. Mitoma, H. Ito and K. Itami, A quest for structurally uniform graphene nanoribbons: synthesis, properties, and applications, *J. Org. Chem.*, 2019, **85**(1), 4–33, DOI: **10.1021/acs.joc.9b02814**.

4 A. C. Neto, F. Guinea, N. M. Peres, K. S. Novoselov and A. K. Geim, The electronic properties of graphene, *Rev. Mod. Phys.*, 2009, **81**(1), 109, DOI: **10.1103/RevModPhys.81.109**.

5 D. J. Rizzo, G. Veber, T. Cao, C. Bronner, T. Chen, F. Zhao, H. Rodriguez, S. G. Louie, M. F. Crommie and F. R. Fischer, Topological band engineering of graphene nanoribbons, *Nature*, 2018, **560**(7717), 204–208, DOI: **10.1038/s41586-018-0376-8**.

6 W. F. da Cunha, P. H. Acioli, P. H. D. oliveira Neto, R. Gargano and G. M. e Silva, Polaron properties in armchair graphene nanoribbons, *J. Phys. Chem. A*, 2016, **120**(27), 4893–4900, DOI: **10.1021/acs.jpca.5b12491**.

7 E. McCann and M. Koshino, The electronic properties of bilayer graphene, *Rep. Prog. Phys.*, 2013, **76**(5), 056503, DOI: **10.1088/0034-4885/76/5/056503**.

8 T. D. S. A. Cassiano, F. F. Monteiro, L. E. De Sousa, G. M. E. Silva and P. H. D. Oliveira Neto, Smooth gap tuning strategy for cove-type graphene nanoribbons, *RSC Adv.*, 2020, **10**(45), 26937–26943, DOI: **10.1039/D0RA02997A**.

9 M. Yankowitz, S. Chen, H. Polshyn, Y. Zhang, K. Watanabe, T. Taniguchi, D. Graf, A. F. Young and C. R. Dean, Tuning superconductivity in twisted bilayer graphene, *Science*, 2019, **363**(6431), 1059–1064, DOI: **10.1126/science.aav1910**.

10 Y.-W. Son, M. L. Cohen and S. G. Louie, Energy gaps in graphene nanoribbons, *Phys. Rev. Lett.*, 2006, **97**(21), 216803, DOI: **10.1103/PhysRevLett.97.216803**.

11 A. Narita, X.-Y. Wang, X. Feng and K. Mullen, New advances in nanographene chemistry, *Chem. Soc. Rev.*, 2015, **44**, 6616–6643, DOI: **10.1039/C5CS00183H**.

12 J. Cai, C. A. Pignedoli, L. Talirz, P. Ruffieux, H. Söde, L. Liang, V. Meunier, R. Berger, R. Li and X. Feng, *et al.*, Graphene nanoribbon heterojunctions, *Nat. Nanotechnol.*, 2014, **9**(11), 896–900, DOI: **10.1038/nnano.2014.184**.

13 J. Oh, Y. Kim, S. Chung, H. Kim and J. G. Son, Fabrication of a MoS2/Graphene nanoribbon heterojunction network for improved thermoelectric properties, *Adv. Mater. Interfaces*, 2019, **6**(23), 1901333, DOI: **10.1002/admi.201901333**.

14 J. Bredas, J. Scott, K. Yakushi and G. Street, Polarons and bipolarons in polypyrrole: Evolution of the band structure and optical spectrum upon doing, *Phys. Rev. B: Condens. Matter Mater. Phys.*, 1984, **30**(2), 1023, DOI: **10.1103/PhysRevB.30.1023**.

15 A. J. Heeger, S. Kivelson, J. Schrieffer and W.-P. Su, Solitons in conducting polymers, *Rev. Mod. Phys.*, 1988, **60**(3), 781, DOI: **10.1103/RevModPhys.60.781**.

16 Z. Sun, Y. Li, S. Xie, Z. An and D. Liu, Scattering processes between bipolaron and exciton in conjugated polymers, *Phys. Rev. B: Condens. Matter Mater. Phys.*, 2009, **79**(20), 201310, DOI: **10.1103/PhysRevB.79.201310**.

17 Y. Liu, S. Gao, X. Zhang, J. H. Xin and C. Zhang, Probing the nature of charge carriers in one-dimensional conjugated polymers: a review of the theoretical models, experimental trends, and thermoelectric applications, *J. Mater. Chem. C*, 2023, **11**, 12–47, DOI: **10.1039/D2TC03574J**.

18 B. Di, Y. Meng, Y. Wang, X. Liu and Z. An, Formation and evolution dynamics of bipolarons in conjugated polymers, *J. Phys. Chem. B*, 2011, **115**(5), 964–971, DOI: **10.1021/jp110875b**.

19 D. Braun and A. J. Heeger, Visible light emission from semiconducting polymer diodes, *Appl. Phys. Lett.*, 1991, **58**(18), 1982–1984, DOI: **10.1103/PhysRevB.44.8652**.

20 Z. Sun and S. Stafström, Bipolaron recombination in conjugated polymers, *J. Chem. Phys.*, 2011, **135**(7), 074902, DOI: **10.1063/1.3624730**.

21 G. M. e Silva, Electric-field effects on the competition between polarons and bipolarons in conjugated polymers, *Phys. Rev. B: Condens. Matter Mater. Phys.*, 2000, **61**(16), 10777, DOI: **10.1103/PhysRevB.61.10777**.

22 T. Astakhova and G. Vinogradov, New aspects of polaron dynamics in electric field, *Eur. Phys. J. B*, 2019, **92**(11), 1–9, DOI: **10.1140/epjb/e2019-100339-y**.

23 A. A. Johansson and S. Stafström, Nonadiabatic simulations of polaron dynamics, *Phys. Rev. B: Condens. Matter Mater. Phys.*, 2004, **69**(23), 235205, DOI: **10.1103/PhysRevB.69.235205**.

24 M. B. Falleiros and G. M. e Silva, Same charge polaron and bipolaron scattering on conducting polymers, *J. Phys. Chem. A*, 2019, **123**(7), 1319–1327, DOI: **10.1021/acs.jpca.8b11725**.

25 T. D. S. A. Cassiano, L. A. R. Júnior, G. M. e Silva and P. H. d O. Neto, Regulating Polaron Transport Regime via Heterojunction Engineering in Cove-Type Graphene Nanoribbons, *Adv. Theory Simul.*, 2023, 2200877, DOI: **10.1002/adts.202200877**.

26 P. H. D. oliveira Neto and T. Van Voorhis, Dynamics of charge quasiparticles generation in armchair graphene nanoribbons, *Carbon*, 2018, **132**, 352–358, DOI: **10.1016/j.carbon.2018.02.062**.

27 Y. Sakai and A. Terai, Dynamics of Quasiparticles Generation, Transport and Relaxation in Armchair-edge Graphene Nanoribbons, *J. Phys. Soc. Jpn.*, 2019, **88**(5), 054718, DOI: **10.7566/JPSJ.88.054718**.

28 A. Troisi and G. Orlandi, Charge-transport regime of crystalline organic semiconductors: Diffusion limited by thermal off-diagonal electronic disorder, *Phys. Rev. Lett.*, 2006, **96**(8), 086601, DOI: **10.1103/PhysRevLett.96.086601**.

29 A. Troisi, Prediction of the absolute charge mobility of molecular semiconductors: the case of rubrene, *Adv. Mater.*, 2007, **19**(15), 2000–2004, DOI: **10.1002/adma.200700550**.

30 L. Wang, O. V. Prezhdo and D. Beljonne, Mixed quantum-classical dynamics for charge transport in organics, *Phys. Chem. Chem. Phys.*, 2015, **17**(19), 12395–12406, DOI: **10.1039/C5CP00485C**.

31 L. Wang, A. V. Akimov, L. Chen and O. V. Prezhdo, Quantized Hamiltonian dynamics captures the low-temperature regime of charge transport in molecular crystals, *J. Chem. Phys.*, 2013, **139**(17), 174109, DOI: **10.1063/1.4828863**.

32 T. Gao, Q. Lu, C. Li, K. Gao and S. Xie, Thermally Induced Exciton Diffusion and Dissociation in Organic Semiconductors,

J. Phys. Chem. C, 2019, **123**(47), 28527–28532, DOI: **10.1021/acs.jpcc.9b06789**.

33 L. Yang, D. Yi, S. Han and S. Xie, Theoretical investigation on thermal effect in organic semiconductors, *Org. Electron.*, 2015, **23**, 39–43, DOI: **10.1016/j.orgel.2015.04.008**.

34 W. P. Su, J. R. Schrieffer and A. J. Heeger, Solitons in polyacetylene, *Phys. Rev. Lett.*, 1979, **42**(25), 1698, DOI: **10.1103/PhysRevLett.42.1698**.

35 M. G. D. Amaral and C. A. D. Carvalho, A Hybrid Monte Carlo Study of the Su-Schrieffer-Heeger Model, *Int. J. Mod. Phys. C*, 1994, **5**(03), 459–481, DOI: **10.1142/S0129183194000659**.

36 W. F. da Cunha, P. H. D. oliveira Neto, R. Gargano and G. Magela e Silva, Temperature effects on polaron stability in polyacetylene, *Int. J. Quantum Chem.*, 2008, **108**(13), 2448–2453, DOI: **10.1002/qua.21798**.

37 Y. Meng, G.-j Guo, Y.-d Wang, Y.-f Li and Z. An, The effects of temperature on the formation and stability of bipolarons in conjugated polymers, *Eur. Phys. J. B*, 2017, **90**, 1–7, DOI: **10.1140/epjb/e2017-80018-7**.

38 P. D. oliveira Neto, J. Teixeira, W. Da Cunha, R. Gargano and G. e Silva, Electron-lattice coupling in armchair graphene nanoribbons, *J. Phys. Chem. Lett.*, 2012, **3**(20), 3039–3042, DOI: **10.1021/jz301247u**.

39 L. A. Ribeiro Jr, W. F. da Cunha, A. L. D. A. Fonseca, G. M. e Silva and S. Stafstrom, Transport of polarons in graphene nanoribbons, *J. Phys. Chem. Lett.*, 2015, **6**(3), 510–514, DOI: **10.1021/jz502460g**.

40 V. N. Kotov, B. Uchoa, V. M. Pereira, F. Guinea and A. C. Neto, Electron-electron interactions in graphene: Current status and perspectives, *Rev. Mod. Phys.*, 2012, **84**(3), 1067, DOI: **10.1103/RevModPhys.84.1067**.

41 J. Williams, T. Low, M. Lundstrom and C. Marcus, Gate-controlled guiding of electrons in graphene, *Nat. Nanotechnol.*, 2011, **6**(4), 222–225, DOI: **10.1038/nnano.2011.3**.

42 M. M. Fischer, L. A. R. Junior, W. F. da Cunha, L. E. de Sousa, G. M. e Silva and P. H. D. oliveira Neto, Ultrafast direct generation of quasiparticles in graphene nanoribbons, *Carbon*, 2020, **158**, 553–558, DOI: **10.1016/j.carbon.2019.11.025**.

43 T. d S. A. Cassiano, G. M. e Silva and P. H. d oliveira Neto, Phase transition of polarons in bilayer graphene nanoribbons, *Phys. Scr.*, 2023, **98**(9), 095922, DOI: **10.1088/1402-4896/acecc2**.

44 G. G. Silva, L. A. Ribeiro Junior, M. L. Pereira Junior, A. L. D. A. Fonseca and R. T. de Sousa Júnior, *et al.*, Bipolaron dynamics in graphene nanoribbons, *Sci. Rep.*, 2019, **9**(1), 1–8, DOI: **10.1038/s41598-019-39774-2**.

45 F. J. Martn-Martnez, S. Fias, G. Van Lier, F. De Proft and P. Geerlings, Electronic structure and aromaticity of graphene nanoribbons, *Chem. – Eur. J.*, 2012, **18**(20), 6183–6194, DOI: **10.1002/chem.201103977**.

46 L. Yang, C.-H. Park, Y.-W. Son, M. L. Cohen and S. G. Louie, Quasiparticle energies and band gaps in graphene nanoribbons, *Phys. Rev. Lett.*, 2007, **99**(18), 186801, DOI: **10.1103/PhysRevLett.99.186801**.

47 T. d S. A. Cassiano, L. E. de Sousa, L. A. R. Junior, G. M. e Silva and P. H. d oliveira Neto, Charge transport in cove-type graphene nanoribbons: The role of quasiparticles, *Synth. Met.*, 2022, **287**, 117056, DOI: **10.1016/j.synthmet.2022.117056**.

48 L. A. Ribeiro, W. F. da Cunha, P. H. de Oliveria Neto, R. Gargano and G. M. e Silva, Effects of temperature and electric field induced phase transitions on the dynamics of polarons and bipolarons, *New J. Chem.*, 2013, **37**(9), 2829–2836, DOI: **10.1039/C3NJ00602F**.

49 V. Cataudella, G. De Filippis and C. A. Perroni, Transport properties and optical conductivity of the adiabatic Su-Schrieffer-Heeger model: A showcase study for rubrene-based field effect transistors, *Phys. Rev. B: Condens. Matter Mater. Phys.*, 2011, **83**(16), 165203, DOI: **10.1103/PhysRevB.83.165203**.

50 L. A. Ribeiro, W. F. da Cunha, P. H. d oliveira Neto, R. Gargano and G. M. e Silva, Dynamical study of impurity effects on bipolaron-bipolaron and bipolaron-polaron scattering in conjugated polymers, *J. Phys. Chem. B*, 2013, **117**(39), 11801–11811, DOI: **10.1021/jp402963k**.

51 A. Terai and Y. Ono, Dynamics of photogenerated soliton pairs in polyacetylene, *Synth. Met.*, 1992, **50**(1–3), 603–609, DOI: **10.1016/0379-6779(92)90217-7**.

52 O. V. Yazyev, Magnetism in disordered graphene and irradiated graphite, *Phys. Rev. Lett.*, 2008, **101**(3), 037203, DOI: **10.1103/PhysRevLett.101.037203**.

53 H. Lee, K. Wakabayashi, Y.-W. Son and Y. Miyamoto, A single particle Hamiltonian for electro-magnetic properties of graphene nanoribbons, *Carbon*, 2012, **50**(10), 3454–3458, DOI: **10.1016/j.carbon.2012.03.009**.

54 D. G. de Oteyza and T. Frederiksen, Carbon-based nanostructures as a versatile platform for tunable π-magnetism, *J. Phys.: Condens. Matter*, 2022, **34**(44), 443001, DOI: **10.1088/1361-648X/ac8a7f**.

APPENDIX C

PUBLISHED PAPERS (BILAYER GNR)

C.1 PAPER C1

Phase transition of polarons in bilayer graphene nanoribbons

Tiago de Sousa Araújo Cassiano

Geraldo Magela e Silva

Pedro Henrique de Oliveira Neto

Phys. Scr. 98 (2023) 095922

10.1088/1402-4896/acecc2

C.2 PAPER C2

Strain-Tuneable Bipolaron Stability on Ultranarrow Bilayer Graphene Nanoribbon

---

Tiago de Sousa Araújo Cassiano

Luiz Antônio Ribeiro Júnior

Geraldo Magela e Silva

Pedro Henrique de Oliveira Neto

J. Phys. Chem. C 2024, 128, 3, 1433–1442

10.1021/acs.jpcc.3c07052

APPENDIX D

PUBLISHED PAPER (MOLECULAR CRYSTAL)

D.1 PAPER D1

Large polarons in two-dimensional fullerene networks: the crucial role of anisotropy in charge transport

T. S. A. Cassiano

M. L. Pereira, Junior

G. M. e Silva

P. H. de Oliveira Neto

L. A. Ribeiro, Junior

Nanoscale, 2024, 16, 2337-2346
10.1039/D3NR04920E